Technical Report
TR-18-07
December 2019

Reactive transport modelling considering transport in interlayer water

New model, sensitivity analyses and results from the Integrated Sulfide Project inter-model comparison exercise

Andrés Idiart
Emilie Coene
Ferran Bagaria
Gabriela Román-Ross
Martin Birgersson

SVENSK KÄRNBRÄNSLEHANTERING AB

SWEDISH NUCLEAR FUEL
AND WASTE MANAGEMENT CO

Box 3091, SE-169 03 Solna
Phone +46 8 459 84 00
skb.se

SVENSK KÄRNBRÄNSLEHANTERING

ISSN 1404-0344
SKB TR-18-07
ID 1690653
December 2019

Reactive transport modelling considering transport in interlayer water

New model, sensitivity analyses and results from the Integrated Sulfide Project inter-model comparison exercise

Andrés Idiart, Emilie Coene, Ferran Bagaria, Gabriela Román-Ross
Amphos 21 Consulting S.L.

Martin Birgersson
Clay Technology AB

Abstract

The main goal of the Integrated Sulfide Project (ISP), a collaboration between Posiva and SKB, is the assessment of copper corrosion in the canister of a KBS-3V repository due to the presence of sulfide. To this end, conceptual and numerical models of the fate of sulfide in the near-field need to be developed to quantify the different processes concerning sulfide production, transport and consumption.

Within Work Package 3 of the ISP (Integration with Safety Case), SKB and Posiva have defined a Base Case scenario with the main physical and chemical processes affecting the fate of sulfide in the near-field, in collaboration with the different modelling teams involved in the project. This Base Case defines the physical properties of the bentonite barriers, the host rock, and the interfaces between these barriers and the host rock. It further defines geochemical processes expected to play a role and the initial composition of each material.

This report summarizes the work undertaken by Amphos 21 in collaboration with ClayTech within the framework of Work Package 3 of the ISP. The main objectives of the present work are:

1. To develop, implement, and verify a new conceptual model for reactive transport modelling in compacted bentonite;
2. To apply the new model for assessing the fate of sulfide in the near-field of a KBS-3V repository system.

The motivation to develop such a model is that recent experimental findings have demonstrated that interlayer pores often dominate the diffusional transport capacity in bentonite. In contrast, many traditional approaches to modelling bentonite chemistry treat the interlayer pores as cation exchange sorption sites, which have no transport capacity. There is consequently a need for developing models which take the transport capacity of the interlayer pores into account.

The newly developed model – named the hybrid model – is restricted to diffusion and reaction processes in water-saturated compacted bentonite. In this model, diffusion occurs exclusively within the interlayer water, while geochemical reactions – including interaction with accessory minerals – are restricted to a disconnected bulk water phase embedded in the bentonite system. Ion equilibrium (i.e. Donnan equilibrium) is maintained at all times between the interlayer and bulk pore solutions.

In this work, the Base Case is implemented using two different reactive transport approaches. The first approach consists of a traditional reactive transport model. In this approach, bentonite is modelled as a single bulk porosity system; interlayer pores are represented by cation exchange sorption sites, with zero volume (bulk porosity equals total or physical porosity). In the second approach, the hybrid model is used, which accounts for diffusion of species exclusively in the interlayer.

Sammanfattning

Huvudsyftet med det integrerade sulfidprojektet (ISP), ett samarbetsprojekt mellan Posiva och SKB, är att bedöma till vilken grad närvaro av sulfid påverkar korrosionen av kopparkapseln i ett KBS-3V-förvar. För detta ändamål måste konceptuella och numeriska modeller av vad som händer med sulfid i närområdet utvecklas för att kvantifiera de olika processerna som rör sulfidproduktion, transport och konsumtion.

SKB och Posiva har i arbetspaket 3 av ISP definierat ett basfallsscenario med de huvudsakliga fysiska och kemiska processerna som påverkar sulfid i närområdet, i samarbete med olika modelleringsgrupper som är involverade i projektet. Detta basfall definierar de fysikaliska egenskaperna hos bentonitbarriärerna, berget och gränsytorna mellan barriärerna och berget. I basfallet definieras de geokemiska processer som förväntas ha betydelse och den initiala sammansättningen för respektive material.

Denna rapport sammanfattar det arbete som Amphos 21 utfört i samarbete med Clay Technology AB inom ramen för ISPs Arbetspaket 3. Huvudsyften med detta arbete är:

1. Att utveckla, implementera och verifiera en ny konceptmodell för reaktiv transportmodellering i kompakterad bentonit;
2. Att tillämpa den nya modellen för att bedöma vad som händer med sulfiden i närområdet (near-field) i ett KBS-3V-förvarssystem.

Motivet till att utveckla en sådan modell är att de senaste experimentella resultaten har visat att porerna mellan flaken i bentoniten ofta är det som dominerar kapaciteten för diffusionstransport. Många traditionella metoder för modellering av bentonitkemi behandlar porerna mellan flaken som katjonbytes- och sorptionsställen, som inte har någon transportkapacitet. Det finns följaktligen ett behov av att utveckla modeller som tar hänsyn till transportkapaciteten hos porerna i bentonitleran.

Den nyutvecklade modellen, som här kallas hybridmodellen, är begränsad till diffusions- och reaktionsprocesser i vattenmättad kompakterat bentonit. I denna modell sker diffusion endast i vattnet mellan bentonitsflaken, medan geokemiska reaktioner – inklusive interaktion med accessoar mineraler – är begränsade till en icke kontinuerlig bulkvattenfas inbäddad i bentonitsystemet. Jonjämvikt (dvs Donnan-jämvikt) upprätthålls hela tiden mellan bulkvattenfasen och vattnet mellan flaken.

I detta arbete implementeras basfallet med två olika reaktiva transportmetoder. Det första tillvägagångssättet består av en traditionell reaktiv transportmodell. I detta tillvägagångssätt modelleras bentonit som system med endast en porositet; porerna mellan betonitflaken representeras av katjonbytes- och sorptionsställen, med nollvolym (bulkporositet är lika med den totala eller fysiska porositeten). I det andra tillvägagångssättet används hybridmodellen, som står för diffusion av ämnen uteslutande i vattnet mellan flaken i bentoniten.

Content

1 Introduction and objectives

This report summarizes the work undertaken by Amphos 21 in collaboration with ClayTech within the framework of Work Package 3 (Integration with Safety Case) of the SKB-Posiva Integrated Sulfide Project (ISP). The main objectives of the present work are:

1. To develop a new conceptual model for reactive transport modelling in compacted bentonite. This model must be capable of reconciling an ion equilibrium-based approach for the diffusion of charged species through the interlayer porosity (Birgersson and Karnland 2009) with a classical geochemical description of compacted bentonite (e.g. Bradbury and Baeyens 2003, Wersin 2003, Arcos et al. 2003).
2. To implement the newly developed conceptual model into the reactive transport modelling framework iCP (Nardi et al. 2014), an interface coupling Comsol Multiphysics (COMSOL 2015) and Phreeqc (Parkhurst and Appelo 2013).
3. To verify the implementation and compare the results with more traditional reactive transport approaches of compacted bentonite.
4. To apply the new model for assessing the fate of sulfide in the near-field of a KBS-3V repository system.

Recent experimental findings have demonstrated that montmorillonite interlayer pores often dominate the diffusional transport capacity in bentonite (Glaus et al. 2007, 2013, 2015). In contrast, many proposed models of bentonite chemistry using single porosity or multi-porosity approaches treat the interlayer pores as cation exchange sorption sites with no transport capacity (see e.g. Alt-Epping et al. 2015, Wersin and Birgersson 2014, Salas et al. 2014, Samper et al. 2016). There is consequently a need for developing models which take the transport capacity of the interlayer pores into account. For instance, Appelo et al. (2010) considered the diffusion of the exchangeable cations to model the transport of strongly sorbed cations such as Cs^+. The multi-porosity model described by Appelo (2013) also assumes an important contribution of the interlayer water on diffusive fluxes. A more detailed discussion about the different available approaches can be found elsewhere (Idiart and Pękala 2016). All these models consider that interlayer water is completely devoid of anions. In contrast, Birgersson and Karnland (2009) consider that interlayer water completely dominates diffusion of cations and anions in compacted bentonite.

The newly developed model – named the hybrid model – is restricted to diffusion and reaction processes in water-saturated compacted bentonite. The key features are the following:

1. Diffusive transport of cations, anions and neutral species occurs exclusively within interlayer water.
2. Geochemical reactions – including interaction with accessory minerals – are restricted to a disconnected bulk water phase embedded in the bentonite system.
3. Ion equilibrium (i.e. Donnan equilibrium) is maintained at all times between the interlayer and bulk pore solutions of bentonite.

Advective transport of ions, which can be important during unsaturated conditions, is at present out of the scope of the model.

The report is broadly divided into two parts: the first part (sections 2 – 5) treats the definition, implementation, and verification of the hybrid model. The second part (sections 6 and 7), focuses on the application of both a 'traditional' reactive transport model and of the hybrid model to the near-field of a KBS-3V repository, with special focus on sulfide transport and reactions (including corrosion of the copper canister).

2 Hybrid model definition

In this section, the proposed model for reactive transport in compacted bentonite, named the hybrid model, is presented. First, a brief description of the components that need to be accounted for in a model for compacted bentonite is given. In the remainder of the section, the mathematical description is presented for treating chemical equilibrium between the model components (in particular equilibrium between bulk and interlayer water), and for treating diffusion within interlayer pores.

2.1 Bentonite components

The components of the system comprised by the compacted bentonite and the surrounding aqueous solution (e.g. groundwater) that are considered in the hybrid model are briefly described here. Bentonite is a clay material dominated by the mineral montmorillonite, which typically represents at least 75 wt.% in high grade material (e.g. Svensson et al. 2011). One of the most distinguishing features of this material – and the reason for considering it as an engineered barrier – is that it swells when contacted with water, i.e. the material expands by actively taking up water.

In addition to montmorillonite, bentonite typically contains several types of accessory minerals, depending on the origin of the material. Typical accessory minerals are quartz, calcite, gypsum, iron (hydr)oxides, and various types of feldspars (e.g. Karnland et al. 2006, Karnland 2010). In addition, bentonite may also contain sulfide components, e.g. pyrite. Furthermore, being a natural soil material, bentonite usually contains some amount of organic matter. In the following, the term accessory mineral is used for any mineral in the bentonite different from montmorillonite.

2.1.1 Montmorillonite

Montmorillonite is a clay mineral of the smectite group. Separate montmorillonite layers are approximately 1 nanometre thick and are built up of one sheet of octahedrally coordinated aluminium (hydr)oxide sandwiched between two tetrahedrally coordinated silicate sheets (Karnland 2010). The extension in the lateral dimensions is typically 100 – 1 000 nanometres. Montmorillonite layers are negatively charged due to substitutions in the atomic structure (aluminium for silicon in the tetrahedral sheets, and magnesium for aluminium in the octahedral sheet). This structural charge is compensated by positively charged ions located at the layer surfaces. In this work, these ions are referred to as the exchangeable ions, for reasons explained below.

The way in which charge is distributed in montmorillonite leads to a strong affinity for water. With access to water, exchangeable ions and surfaces become hydrated due to electrostatic interactions between charges and dipolar water molecules. As a consequence, montmorillonite particles are typically arranged in a face-to-face configuration with thin water films (nanometre wide) between adjacent particles. The space between individual layers of montmorillonite is referred to as the interlayer space.

The extent of hydration of montmorillonite depends on the availability of water (e.g. due to an imposed vapour pressure) and the width of the interlayer space varies correspondingly. X-ray diffraction measurements reveal interlayer distances corresponding to one, two, three, and occasionally four monolayers of water, depending on water availability and the type of exchangeable cations. In systems dominated by small alkali metal ions (Li^+, Na^+, K^+), a continuously varying interlayer space is observed at higher water contents. In such systems, interlayer distances up to the order of 10 nanometres have been observed. The ability to take up water in interlayer spaces is the mechanism governing bentonite swelling.

In hydrated montmorillonite, the exchangeable ions are quite mobile, even at low water contents. These ions can therefore be replaced by other ions if the montmorillonite is contacted with an external ionic solution that is not in equilibrium with the interlayer solution. Thus, montmorillonite (and by extension, bentonite) functions as an ion exchanger, which justifies using the nomenclature “exchangeable” for the ions compensating the structural charge. The mobility of the exchangeable

ions in hydrated montmorillonite strongly indicates that these should be associated with the water in the interlayer space rather than directly with the particle surfaces. Thus, although the exchangeable ions quite often are referred to as “sorbed”, it must be kept in mind that these ions are not immobilized due to bonding to specific surface sites. Instead, as the electrostatic potential generally is lowered in the interlayer space as compared to the external solution, cations accumulate there, in accordance with the Boltzmann distribution (see Section 2.3.1).

Apart from structural charge, montmorillonite particles may also carry charge at specific sites on their edges due to protonation/deprotonation. This amount of charge corresponds to a few percent of the total charge of the particle, and depends on the chemical conditions, especially on pH. Also, other specific ions/molecules may sorb onto the edge sites.

2.1.2 Interlayer water

The total amount of water in highly compacted bentonite corresponds to a few monolayers of interlayer water if distributed evenly (three monolayers gives approximately a porosity of 50 %, corresponding to a montmorillonite dry density of 1.4 g/cm^3). From the above description of the physicochemical properties of the interlayer, it is thus expected that water in compacted bentonite is mainly distributed in interlayer spaces. This has also been inferred experimentally in a number of studies (e.g. Holmboe et al. 2012, Keller et al. 2014). It may be noted that interlayer spaces dominate the pore volume in compacted bentonite also in solute diffusion conceptual models that acknowledge heterogeneity in the porosity types within the bentonite scientific community (see e.g. Appelo 2013).

As the ever-present exchangeable ions are associated with the water in the interlayer spaces, the latter resembles an ionic solution in several respects. However, as the interlayer solution is under all circumstances positively charged, it cannot be described as a conventional bulk water solution. Also, as the electrostatic potential may vary across the interlayer thickness, heterogeneous ion configurations are generally expected.

Since interlayer space is defined as the volume between two basal surfaces of adjacent montmorillonite layers, it follows that interlayer water is the water occupying this volume. However, in this work the definition of interlayer water is extended to include any water that is affected by the electric charge of montmorillonite and thus containing exchangeable ions. Thus, the term will be used, for instance, to refer to the pore solution between a montmorillonite particle and a grain of an accessory mineral (Hsiao and Hedström 2017).

Interlayer water can be considered a non-conventional aqueous solution and is expected to contain other dissolved species (including ions) in addition to the exchangeable cations. It is noted that the total positive charge of the interlayer cations should be equal to the sum of the CEC of montmorillonite and the negative charge of the anions present in the interlayer to maintain electroneutrality. Although it is not the focus of this work, an exploratory study of aqueous interlayer chemistry is presented in Section 2.5.1.

2.1.3 Accessory minerals

Mineral dissolution and precipitation reactions involve both montmorillonite and accessory minerals, and fall into two general categories (Arcos et al. 2000, Curti and Wersin 2002):

- Fast and reversible reactions reaching equilibrium relatively rapidly (within minutes, hours or days), and
- Slow, kinetically-controlled reactions that require very long equilibration periods (years).

The first group includes carbonates (calcite, siderite), sulfates (gypsum), certain oxides (chalcedony, amorphous silica, some Fe-oxides), and other soluble salts (e.g. halite). The latter group mainly involves reactions of silicate minerals, e.g. montmorillonite, mica, or feldspars.

In this work, the focus is on the minerals that react with the aqueous solution in a relatively rapid way. Furthermore, in the hybrid model presented below it is considered that explicit water-mineral

interaction occurs exclusively within a (saturated) bulk porosity. As stated above, the pore volume is dominated by interlayer water and only a small volume fraction of bulk porosity is expected in compacted bentonite.

2.1.4 Bulk water

It is clear that interlayer water must be considered when modelling reactive transport processes along engineered barriers that include compacted bentonite components. Bulk water solutions are, at the same time, also essential for describing this type of systems. In the case of a KBS-3 repository, bulk water is present in the fractures of the crystalline host rock, or in the interface between the barriers and the host rock. It can also be conceived of as constituting a minor part of the bentonite pore water in the form of relatively large and disconnected pores (e.g. Holmboe et al. 2012), either surrounded completely by montmorillonite or also by accessory minerals. Consequently, interlayer water and bulk water must be simultaneously treated when modelling the KBS-3 near field.

Bulk water in the present context is defined as any water different from the interlayer water. In particular, a bulk water solution is charge neutral and constitutes a phase of its own. The latter requirement implies that a separate pressure can be defined in a bulk solution, and that it thereby may maintain advective flow. In contrast, the interlayer water pressure is identical to what is usually referred to as "swelling pressure", and its gradient is associated with mechanical deformation rather than with advective water flow (Birgersson and Karnland 2014).

2.2 Definition of the hybrid model for compacted bentonite

The hybrid model proposed in this work is a macroscopic continuum model defined on a certain coordinate system $\boldsymbol{X}$. The variable used to specify positions in the model is here denoted x, with $x \in \boldsymbol{X}$. Mathematically, the model is defined by a set of variables, which are functions of x:

$c_i^{bulk}(x)$ − a set of aqueous species concentrations in a bulk water phase at point x (chemical species are labelled by subscript i).

$c_i^{int}(x)$ – a corresponding set of interlayer concentrations at point x.

$\omega_i(x)$ – a set of volume fractions (or concentrations) of accessory minerals at point x (the accessory minerals are labelled by subscript j).

Note that these functions physically represent microscopically averaged quantities in a representative elementary volume (REV) at position x.

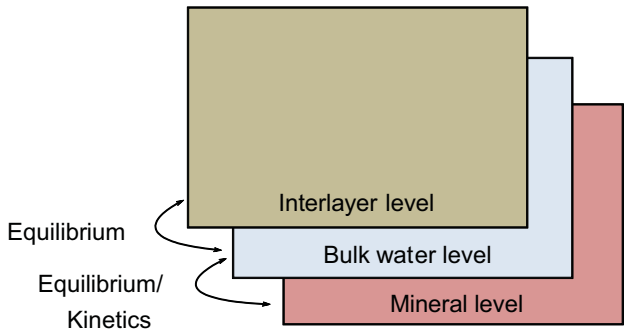

Figure 2-1. *Hybrid model schematics showing the three different "levels": interlayer water, bulk water, and (accessory) minerals. The model domain* $\boldsymbol{X}$ *is here represented by a rectangle.*

2.2.1 Hybrid model “levels”

Conceptually, the three sets of variables presented above may be viewed as constituting three different “levels”, as illustrated in Figure 2-1.

One of the key features of the model is that Fickian diffusive flux is driven by interlayer concentration gradients, i.e. mass transport only occurs in the interlayer “level”: diffusive transport is further discussed in Section 2.4. Chemical processes, on the other hand, are only explicitly treated in the bulk water “level” and between bulk water and mineral “levels”. With this partitioning of the processes, already existing models for bulk water chemistry (i.e. Phreeqc) can be used for all chemical processes in the hybrid model.

The second key feature is the local Donnan equilibrium constraint (ion equilibrium) assumed between the interlayer and bulk solutions (both within the bentonite and at the boundaries with adjacent materials) at all times, i.e. between the interlayer and bulk water “levels”. As a result, ion equilibrium calculations need to be performed not only at boundaries to pure bulk water domains (e.g. rock fractures), but over the entire model domain $\boldsymbol{X}$.

Consequently, ion equilibrium quantities (Ξ_i, f_D) as described in Section 2.3 will appear as derived variables, which are functions of x, e.g. $\Xi_i(x)$, and $f_D(x)$.

At this point, it is worthy to mention that various concepts with the name “Donnan” have been proposed in the literature. Most of these refer exclusively to the equilibrium of anions, e.g. “Donnan exclusion”, or “Donnan volume”. In this report, the term ion equilibrium is preferred to simultaneously refer to equilibrium of both anions and cations. Adopting ion equilibrium for every charged species implies that the physico-chemical bentonite model does not include a separate model for cation exchange nor edge site sorption reactions. On the contrary, cation exchange comes out naturally from the cation equilibrium between interlayer and bulk water.

2.2.2 Water and mineral partitioning

If the hybrid model should represent a real bentonite sample, additional constraints should be imposed. In particular, the volume fraction of each “level” must be considered. The interlayer and bulk water “levels” are assumed to contain all water in the system, and since full water saturation is also assumed, each of these two “levels” can be attributed a porosity variable, the sum of which equals the total porosity (ϕ)

$$\phi^{int} + \phi^{bulk} = \phi \tag{2-1}$$

As the choice of concentration units usually relates to mass of water (e.g. molal), the water-to-solid mass ratios are convenient variables

$$w^{int} = \frac{M_w^{int}}{M_s} \tag{2-2}$$

$$w^{bulk} = \frac{M_w^{bulk}}{M_s} \tag{2-3}$$

where M_w^{int} and M_w^{bulk} respectively denote interlayer and bulk water mass, and M_s is the total mass of solids in the bentonite. The constraint on water masses can now be written

$$w^{int} + w^{bulk} = w \tag{2-4}$$

Where w is the total (measurable) water ratio.

The water-to-solid mass ratios may be converted to porosities as

$$\phi^{int} = \frac{M_w^{int}/\rho_w}{V^{total}} = \frac{w^{int} \cdot M_s}{V^{total} \cdot \rho_w} = w^{int} \cdot \frac{\rho_d}{\rho_w} \tag{2-5}$$

Where V^{total} is the total volume of the system (solids and water), $\rho_d = M_s/V^{total}$ is dry density (kg/m^3), and ρ_w is water density (here assumed to be 1 000 kg/m^3). The bulk porosity is expressed analogously.

The mass fraction of mineral phase *j* is defined as

$$x_j = \frac{M_j}{M_S} \tag{2-6}$$

and the constraint on these variables is

$$\sum x_j = 1 \tag{2-7}$$

It is convenient to separate out the montmorillonite x_{mmt} and the accessory mineral parts x_{acc}

$$x_{mmt} + x_{acc} = 1 \tag{2-8}$$

Mineral mass fractions can be converted to a corresponding variable relating to volume. Thus, the volume fraction of mineral phase *j* is

$$\phi^j = \frac{M_j/\rho_j}{V^{total}} = x_j \cdot \frac{\rho_d}{\rho_j} \tag{2-9}$$

where ρ_j is the density of the mineral phase.

With these definitions, the following constraint on volume can be stated

$$\phi^{int} + \phi^{mmt} + \phi^{bulk} + \phi^{acc} = 1 \tag{2-10}$$

where the two first terms in this sum relate to the interlayer "level", the third term to the bulk water "level", and the last term to the mineral "level".

In practice, the bulk water porosity should be chosen much smaller than the interlayer porosity, as interlayer pores dominate the structure of compacted bentonite. This is also the rationale for assuming that diffusion is exclusively restricted to the interlayer "level". The bulk water and accessory minerals can be interpreted as disconnected "islands" in a matrix of a montmorillonite/interlayer water mixture (Figure 2-2).

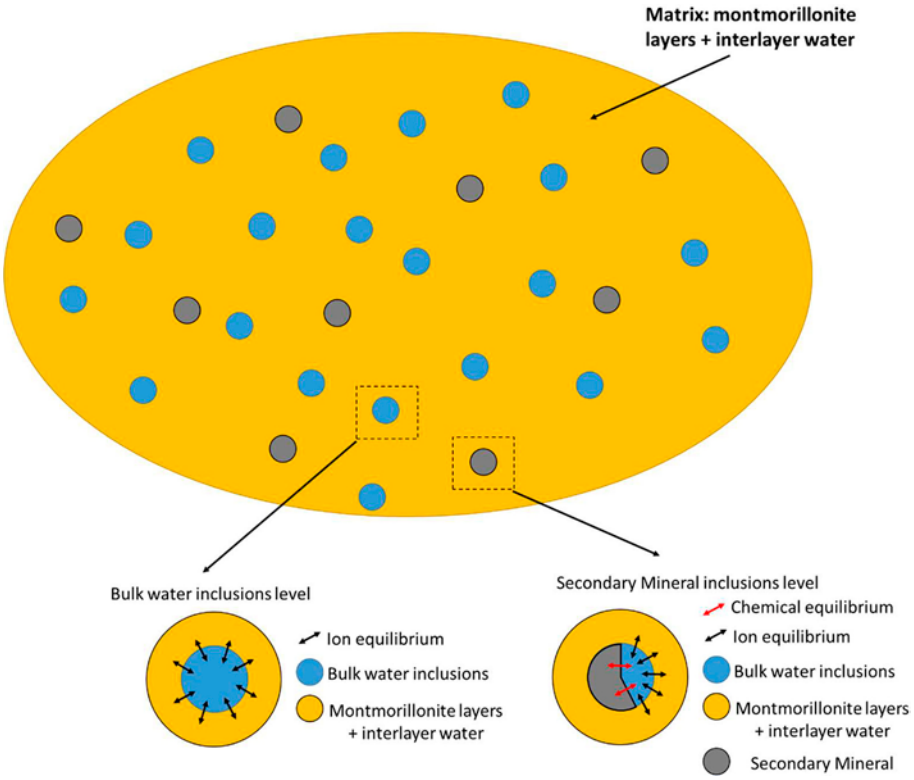

Figure 2-2. *Schematic description of the microstructure envisaged at a given point x in the continuum model domain X: a "matrix" of interlayer water and montmorillonite layers, which occupies the majority of the total volume, surrounds the bulk water porosity and the accessory minerals. In this approach, diffusive transport is exclusively dominated by the interlayer water.*

2.3 Ion Equilibrium

The term chemical equilibrium indicates thermodynamic equilibrium concerning partitioning of mass, in which the corresponding thermodynamic force is governed by the chemical potential. This section considers the chemical equilibrium between an interlayer and a bulk water component, referred to here as ion equilibrium (see also Section 2.2). Ion equilibrium is central in the hybrid model and must furthermore be considered at any boundary between bentonite and external or bulk water.

2.3.1 Model formulation

The system here considered is a fully homogeneous interlayer component in contact with a bulk water solution, as schematically illustrated in Figure 2-3. This system may represent either a boundary between bentonite and external solution (e.g. groundwater), or the interlayer and bulk water levels at a given point within a hybrid model.

The confinement of charged montmorillonite particles implies a difference in electrostatic potential between the interlayer component and the bulk solution (Figure 2-3). This difference is referred to here as the Donnan potential, ψ^*. Note that ψ^* is a negative quantity, since montmorillonite particles carry negative charge.

As the interlayer component is assumed homogeneous, it is completely specified by its water-to-solid mass ratio, w, and its cation exchange capacity, CEC, which quantifies the amount of exchangeable cations in terms of charge equivalents per kilogram dry clay.

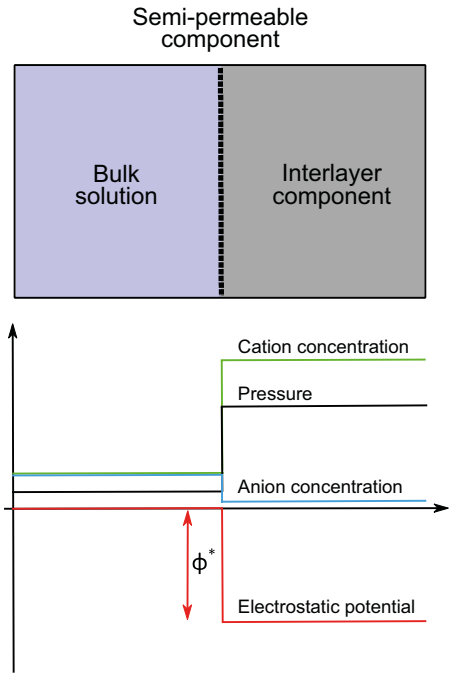

Figure 2-3. *System considered for ion equilibrium, showing the interface between the bulk solution and the interlayer component as a semi-permeable membrane resulting in discontinuous fields of species concentrations, pressure, and electrostatic potential.*

The electro-chemical potential for an aqueous species *i* in an electrostatic potential ψ is

$$\mu_i = \mu_i^0 + RT \cdot \ln a_i + F \cdot z_i \cdot \psi \quad (2\text{-}11)$$

where a_i and z_i are respectively activity and charge of the species *i, R* is the universal gas constant, *T* is the absolute temperature, *F* is the Faraday's constant, and μ_i^0 a reference potential.

At equilibrium, the electro-chemical potential reaches a single value in the interlayer and bulk solutions. Applying Equation 2-11 in the entire system (i.e. bulk plus interlayer) gives

$$\ln a_i^{bulk} = \ln a_i^{int} + \frac{F \cdot z_i}{RT} \cdot \psi^\star \quad (2\text{-}12)$$

Here, superscripts "bulk" and "int" respectively are used for quantities in the bulk and interlayer solutions. Equation 2-11 can be rewritten as

$$a_i^{int} = f_D^{-z_i} \cdot a_i^{bulk} \quad (2\text{-}13)$$

where a "Donnan factor" has been defined as

$$f_D = e^{\frac{F \cdot \psi^\star}{RT}} \quad (2\text{-}14)$$

Note that, since ψ^* is a negative quantity, f_D ranges between 0 and 1 (corresponding, respectively, to infinitely negative and zero Donnan potential).

Equation 2-13 can be restated in terms of concentrations

$$c_i^{int} = \Gamma_i \cdot f_D^{-z_i} \cdot c_i^{bulk} \quad (2\text{-}15)$$

where

$$\Gamma_i = \frac{\gamma_i^{bulk}}{\gamma_i^{int}} \quad (2\text{-}16)$$

is the ratio between the activity coefficients in the bulk and interlayer solutions for the species *i*.

Given the interlayer concentrations for all involved charged species, the requirement of zero net charge in this compartment can be stated as

$$Q_{net} = \sum_i z_i \cdot F \cdot c_i^{int} \cdot M_w^{int} + Q_{surf} = 0 \quad (2\text{-}17)$$

where M_w^{int} denotes total interlayer water mass, and Q_{surf} total surface charge of montmorillonite. Q_{surf} can be calculated from the cation exchange capacity (CEC)

$$Q_{surf} = -CEC \cdot M_s \quad (2\text{-}18)$$

Where M_s is total bentonite solid mass.

The requirement of zero net charge can thereby be rewritten as

$$\sum_i z_i \cdot c_i^{int} - c_{IL} = 0 \quad (2\text{-}19)$$

Where c_{IL} is given by

$$c_{IL} = \frac{CEC}{F \cdot w^{int}} \quad (2\text{-}20)$$

where $w_{int} = M_w^{int}/M_s$ is the interlayer water-to-solid mass ratio.

Combining Equations 2-19 and 2-15 gives an equation for f_D

$$\sum_i z_i \cdot \Gamma_i \cdot f_D^{-z_i} \cdot c_i^{bulk} = c_{IL} \quad (2\text{-}21)$$

which is to be solved given a complete specification of the external concentrations (c_i^{bulk}) and a value of c_{IL}. Note that the parameter c_{IL} quantifies the required interlayer concentration of monovalent cations to precisely compensate the structural charge. Equation 2-21 is a polynomial function with f_D as the unknown and which order is defined by the maximum and minimum charges of the ions involved.

Once the solution to Equation 2-21 is found, the interlayer concentrations are directly given by Equation 2-15. In many cases it is however convenient to express the concentration ratio between the interlayer and the bulk solution. Therefore, so-called ion equilibrium coefficients are defined as

$$\Xi_i = \frac{c_i^{int}}{c_i^{bulk}} \tag{2-22}$$

From Equation 2-15 it directly follows that

$$\Xi_i = \Gamma_i \cdot f_D^{-z_i} \tag{2-23}$$

Equation 2-23 clearly expresses the concentration discontinuities which are maintained across an interface between a bulk solution and an interlayer component in equilibrium (Figure 2-3). The general trend – expressed by the factor f_D^{-zi} – is an enhancement of positively charged ions in the interlayer, while negatively charged ions are reduced. In addition, this general behaviour is modified due to differences in activity coefficients, as expressed by the factor Γ_i.

As a consequence of the generally larger total amount of ions in the interlayer component as compared to the bulk solution (which in turn follows from the presence of charged montmorillonite particles) there is generally an osmotic pressure difference across the interface ('swelling pressure'). Thus, if both the bulk solution and the interlayer component considered here should represent physical quantities, it is required that they are separated by an interface component (Figure 2-3). This interface functions as a semi-permeable membrane, in the sense that it should not allow montmorillonite particles to escape. Moreover, it must be able to withstand the osmotic pressure difference. In the case of an external solution in contact with compacted bentonite, this interface component is typically a steel filter in a laboratory context, or a fractured host rock in a KBS-3 repository.

Equation 2-21 is an equation for calculating f_D given the bulk solution concentration. It is also possible, and sometimes relevant, to instead calculate this quantity given the interlayer concentrations. The equation is in this case slightly simpler, as it expresses the charge neutrality of the bulk solution (i.e. $\sum_i z_i \cdot c_i^{bulk} = 0$) and reads

$$\sum_i \frac{z_i \cdot f_D^{z_i} \cdot c_i^{int}}{\Gamma_i} = 0 \tag{2-24}$$

2.3.2 Partitioning between bulk and interlayer water

Assume a set, $\{n_i\}$, of total amounts of species in a bentonite sample, expressed as moles per kg solid substance. The task is to partition these ions between a bulk water and an interlayer compartment, quantified by water-to-solid mass ratios w^{bulk} and w^{int}, respectively, and with the constraint of having ion equilibrium. Denoting by h_i the fraction of species i in the bulk compartment, ion equilibrium for this species reads

$$\frac{(1-h_i)\cdot n_i}{w^{int}} = \Xi_i \cdot \frac{h_i \cdot n_i}{w^{bulk}} \tag{2-25}$$

Solving this equation for h_i gives

$$h_i = \frac{1}{1+\Xi_i \cdot \frac{w^{int}}{w^{bulk}}} \tag{2-26}$$

It can be observed that the partition of species i between bulk and interlayer waters depends solely on its ion equilibrium coefficient, provided that the bulk and interlayer water contents are constant. Rewriting the equation for the Donnan potential in terms of h_i gives

$$\sum_i z_i \cdot \Xi_i \cdot \frac{1}{1+\Xi_i \cdot \frac{w^{int}}{w^{bulk}}} \frac{n_i}{w^{bulk}} = c_{IL} \tag{2-27}$$

which can be reduced to

$$\sum_i \frac{z_i \cdot n_i}{\frac{w^{bulk}}{\Xi_i} + w^{int}} = c_{IL} \tag{2-28}$$

2.3.3 Activity coefficients

The activity coefficients and activity coefficient ratios (Equation 2-16) play a key role within the proposed framework for ion equilibrium calculations (Equation 2-21). To estimate activity coefficients in bulk solution, well established methods are available, as implemented e.g. in Phreeqc. The estimation of these quantities in an interlayer context is on the other hand subject to much larger uncertainties. For example, Idiart and Pękala (2016) used SIT (specific ion interaction theory) activity correction approach to estimate interlayer activity coefficients at high ionic strength (~3 M).

One approach to defining the ionic strength of the interlayer would be to simply use the conventional formula involving the concentration of all ions present. Such an approach, however, neglects charge contributions from the montmorillonite particles; the interlayer solution is in itself not charge neutral. Therefore, the following definition is proposed here for the interlayer ionic strength

$$I^{int} = \frac{1}{2}\left(\sum_i z_i^2 c_i^{int} + c_{IL}\right) \tag{2-29}$$

This formula contains contributions both from the actual ions in the interlayers as well as from the structural charge, and thereby involves charges which are balanced. Note that c_{IL} quantifies the amount of structural charge in terms of an equivalent interlayer concentration of mono-valent charges. The "mono-valent" character of the structural charges is thus accounted for in the way Equation 2-29 is formulated.

The ionic strength of the interlayer is under all relevant circumstances dominated by the contribution from the structural charge (regardless of whether the c_{IL}–term is included). The relative variation of interlayer ionic strength is therefore expected to be small under many circumstances. A working hypothesis is therefore to treat interlayer activity coefficients as approximately constant. That is, each species will in general have its own interlayer activity coefficient, but this coefficient will remain approximately constant if the ionic strength within the interlayer water does not significantly vary. Part of the development work within the ISP is devoted to assessing these quantities.

2.3.4 Relating selectivity coefficients with interlayer activities

The most general exchange reaction in a system containing two types of cations can be written as

$$\nu M_1 X_{z_1} + \nu \frac{z_1}{z_2} M_2^{+z_2} \leftrightarrow \nu \frac{z_1}{z_2} M_2 X_{z_2} + \nu M_1^{+z_1} \tag{2-30}$$

where the cations are labelled M_1 and M_2, respectively, and z_1 and z_2 are the corresponding valencies. The overall factor ν is furthermore chosen as to reduce all stoichiometric factors to the smallest possible integers. The law of mass action for the above reaction in the Gaines-Thomas convention becomes

$$K = \left[\frac{X_2^{\frac{z_1}{z_2}} \cdot a_1^{bulk}}{X_1 \cdot (a_2^{bulk})^{\frac{z_1}{z_2}}}\right]^{\nu} \tag{2-31}$$

where K is the selectivity coefficient, and X_1 and X_2 are the equivalent charge fraction in the clay of cation 1 and 2, respectively. These can be expressed using interlayer concentrations

$$X_1 = \frac{z_1 \cdot c_1^{int}}{Q_{tot}} \tag{2-32}$$

$$X_2 = \frac{z_2 \cdot c_2^{int}}{Q_{tot}} \tag{2-33}$$

where Q_{tot} is the total cation charge (per unit volume) in the interlayer, given by

$$Q_{tot} = z_1 \cdot c_1^{int} + z_2 \cdot c_2^{int} \tag{2-34}$$

Combining the relations above gives a complex general expression for the selectivity coefficient

$$K = \left[\frac{(z_2 \cdot \Gamma_2 \cdot f_D^{-z_2} \cdot c_2^{bulk})^{\frac{z_1}{z_2}} \gamma_1^{bulk} \cdot c_1^{bulk}}{z_1 \cdot \Gamma_1 \cdot f_D^{-z_1} \cdot c_1^{bulk} \cdot (\gamma_2^{bulk})^{\frac{z_1}{z_2}} \cdot (c_2^{bulk})^{\frac{z_1}{z_2}}}\right]^{\nu} Q_{tot}^{\left(1-\frac{z_1}{z_2}\right)\nu} \quad (2\text{-}35)$$

However, in this expression all properties relating to the bulk solution cancel, as well as the Donnan factors, giving

$$K = \left[\frac{(z_2)^{\frac{z_1}{z_2}} \cdot (\gamma_1^{int})}{(z_1) \cdot (\gamma_2^{int})^{\frac{z_1}{z_2}}}\right]^{\nu} Q_{tot}^{\left(1-\frac{z_1}{z_2}\right)\nu} \quad (2\text{-}36)$$

This expression may still look rather complex, but in the case of exchange between ions of the same valency ($z_1 = z_2$, $\nu = 1$), it reduces to a very simple one

$$K = \frac{\gamma_1^{int}}{\gamma_2^{int}} \quad (2\text{-}37)$$

The other relevant case in practice is exchange between a mono-valent and a di-valent ion (e.g. $z_1 = 1$, $z_2 = 2$, $\nu = 2$), for which the selectivity coefficient reads

$$K = 2\frac{(\gamma_1^{int})^2}{\gamma_2^{int}} Q_{tot} \approx 2\frac{(\gamma_1^{int})^2}{\gamma_2^{int}} c_{IL} \quad (2\text{-}38)$$

The last approximate equality is valid in the limit of low bulk concentration.

These expressions underline the need for a sound understanding and representation of the activity coefficients in the interlayer water. It is only in that case that meaningful selectivity coefficients according to this modelling approach can be obtained.

2.4 Diffusive transport in the interlayer

In the hybrid model proposed here, which considers Donnan equilibrium between the bulk and interlayer solutions, the ions in the interlayer are allowed to diffuse freely. This is in contrast with the traditional reactive transport models with cation exchange reactions, where exchangeable cations are considered to be fixed to the exchanger surface. Diffusion of ions across the interlayer water has been studied by other authors and is acknowledged as an important diffusion path in compacted bentonite (Birgersson and Karnland 2009, Gimmi and Kosakowski 2011, Appelo 2013).

Fickian diffusion is assumed here, i.e. the diffusive flux of a species i is assumed proportional to the gradient of the interlayer concentration of the same species

$$j_i = -\phi^{int} \cdot D_c \cdot \nabla c_i^{int} \quad (2\text{-}39)$$

where ϕ^{int} denotes interlayer porosity and D_c the interlayer pore diffusion coefficient. In this equation, it is assumed that the concentration variable is expressed in terms of water volume rather than water mass. The conversion between the two types of variables is made by multiplying by the solution density, as expressed in terms of water mass, by the factor $\rho_{sol} \cdot x_w$, where ρ_{sol} denotes the density of the interlayer solution, and x_w is the mass fraction of water in this solution. In practice, this factor will be assumed equal to unity.

Since the local interlayer charge must remain constant, it is required that the pore diffusion coefficient D_c is one and the same for all species. A more rigorous treatment, which allows for individual mobilities of the species, would involve e.g. the Nernst-Planck equation, which couples the (relative) ion fluxes to the electric field. This is out of the scope of the present study, although the implementation of the model can be extended from the current Fickian diffusion approach to the more general equations describing diffusion and electro-migration. Nonetheless, it is expected that the effect of electro-migration will be of second order importance when compared to the effect of expressing fluxes in terms of interlayer concentration gradients.

2.4.1 Relation to (external) bulk water concentration

Equation 2-39 relates fluxes to interlayer concentration gradients. It is often also required to relate fluxes to externally imposed boundary conditions, expressed using bulk water concentrations. Thus, the theory of ion equilibrium (Section 2.3) must be incorporated.

An experimental tracer through-diffusion set-up, which is commonly used to evaluate diffusion coefficients in compacted bentonite, is schematically illustrated in Figure 2-4. The steady-state flux for a tracer is related to the concentration difference in the two external aqueous solutions ($\Delta c_i^{ext} = c_{source} - c_{target}$) *via* the so-called effective diffusion coefficient, D_e

$$j_i = D_e \cdot \frac{\Delta c_i^{ext}}{L} \tag{2-40}$$

Where L is the length to the bentonite sample in the diffusion direction. Equation 2-40 implicitly relates the diffusive flux to a gradient in a presumed bulk solution phase in the bentonite (see Figure 2-4). In this sense, the parameter D_e always relates to a bulk water phase (Bourg and Tournassat 2015). Using also Equation 2-39 to express the steady-state flux in the tracer through-diffusion set-up gives a relation between D_e and the interlayer pore diffusion coefficient D_c

$$D_e = \phi^{int} \cdot \Xi_i \cdot D_c \tag{2-41}$$

The effective diffusion coefficient is basically always related to a (bulk) pore diffusion coefficient D_p as $D_e = \phi \cdot D_p$ (see e.g. Bourg and Tournassat 2015). The relation between D_p and D_c is consequently

$$D_p = \frac{\phi^{int}}{\phi} \cdot \Xi_i \cdot D_c \tag{2-42}$$

Note that Ξ_i is here assumed to be independent of position, since the aqueous chemistry is kept constant throughout the system while the diffusing species is assumed to be present only at tracer level.

Equation 2-41 reveals that even though D_c is kept constant for all species, the effective diffusion coefficient is generally different for each species, since it depends on the species-specific quantity Ξ_i. Moreover, due to the dependence on the ion equilibrium coefficient, D_e for a given species depends on the Donnan potential, which in practice implies a dependence on ionic strength for charged species; as the ionic strength decreases, D_e for cations increases indefinitely, while D_e for anions tends toward zero. Thus, the experimental observation that diffusive transport capacity for cations increases with decreasing ionic strength (Glaus et al. 2010, Tachi and Yotsuji 2014) is interpreted as an increased mobility in models which use D_e as the fundamental transport parameter. In contrast, the interpretation in the hybrid model is an increased interlayer concentration gradient as a consequence of an increased (negative) Donnan potential (i.e. an increased mass of ions with maintained mobility, rather than a smaller mass of ions with increased mobility).

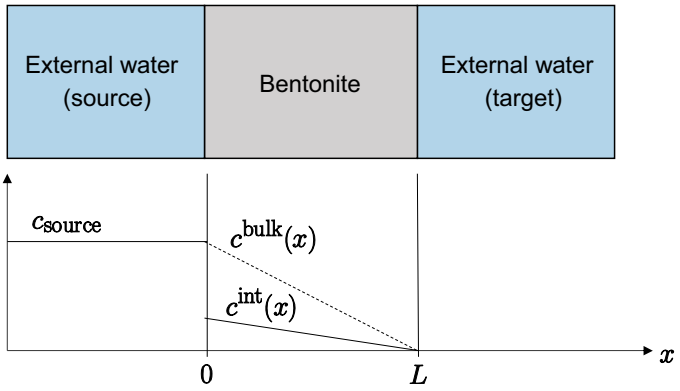

Figure 2-4. *Schematics of the tracer through diffusion set-up. Bottom diagram shows the tracer concentration at steady-state – the bulk solution concentration varies continously across the interfaces between external solution and bentonite, while the interlayer concentration varies discontinously (since the interlayer concentration is reduced this illustration refers to an anion concentration).*

Table 2-1. Speciation of the external water used to evaluate D_e in the hybrid model. External water activity coefficients from Debye-Hückel activity correciton model. Interlayer activity coefficients taken from Birgersson (2019).

Species	External conc. (mM)	γ^{ext}	γ^{int}
Ca^{2+}	14.900	0.357	0.495
Cl^-	111.570	0.745	0.570
Mg^{2+}	6.463	0.357	0.495
Na^+	74.460	0.755	0.704
SO_4^{2-}	2.808	0.330	0.030

As an example, consider an external solution as specified in Table 2-1 in contact with a bentonite specified by c_{IL} = 2873 mM (the value for the bentonite buffer in the Base Case, see Section 6.4). The external water and the clay were equilibrated by solving Equation 2.21 for f_D and the system of Equations 2.22 for the interlayer concentrations. Using the activity coefficients listed in Table 2-1 gives a Donnan factor of f_D = 0.118. In Figure 2-5 the resulting values of D_e for various species are plotted as a function of D_c (assuming that ϕ^{int} = 0.43). It may be noted that, generally, D_e is larger for species with high positive charge, and becomes smaller for species with high negative charge; for e.g. the value $D_c = 5\cdot10^{-11}$ m^2/s, the corresponding D_e values for the ions under consideration is in the range $3\cdot10^{-12}$ –10^{-9} m^2/s. The specific value of D_e is however also dependent on the activity coefficients in the external solution and the interlayer. In Figure 2-5 it may for instance be noted that the effective diffusion coefficient for sulfate is basically equal to that of chloride although it is a di-valent anion. The reason for this is that SO_4^{2-} is attributed a very low interlayer activity coefficient (0.03) (see further Section 4.2.2).

Note that the relation between D_e and D_c expressed by Equation 2-41 can only strictly be established in steady-state. Here, however, Equation 2-41 is used as a general definition of D_e. Starting from Equations 2-39 and 2-22, the diffusive flux can then be expressed in general in terms of the bulk water concentration as (applying the chain rule)

$$j_i = -\phi^{int} \cdot D_c \cdot \nabla\left(\Xi_i \cdot c_i^{bulk}\right) = -D_e \cdot \nabla c_i^{bulk} - \phi^{int} \cdot D_c \cdot c_i^{bulk} \cdot \nabla\Xi_i \qquad (2\text{-}43)$$

This expression shows that the diffusive flux in the hybrid model is proportional to the bulk solution concentration gradient only under conditions where $\nabla\Xi_i = 0$, i.e. when the aqueous chemistry is basically the same everywhere. In general, the "bulk flux" (first term in Equation 2-43) is "corrected" by the second term in equation, which moreover may be dominating in some cases.

2.4.2 Mass conservation in the hybrid model

In the previous section, various properties of the diffusive flux within the hybrid model were examined. The corresponding evolution of species concentrations under the assumption that no chemical processes are active is explored here. In the hybrid model, diffusive flux is postulated to occur exclusively in the interlayer, while bulk pores contain stagnant water. In this context, the continuity equation (which describes the conservation of mass) reads

$$\frac{\partial c_i^{tot}}{\partial t} = -\nabla j = \phi^{int} \cdot D_c \cdot \nabla^2 c_i^{int} \qquad (2\text{-}44)$$

were c_i^{tot} denotes the total concentration in terms of the volume of the full porous medium which may be written $c_i^{tot} = \varphi^{int}\cdot c_i^{int} + \varphi^{bulk}\cdot c_i^{bulk}$. The continuity equation can thereby be rewritten as

$$\frac{\partial c_i^{int}}{\partial t} = D_c \cdot \nabla^2 c_i^{int} - \frac{\phi^{bulk}}{\phi^{int}}\frac{\partial c_i^{bulk}}{\partial t} \qquad (2\text{-}45)$$

Using Equation 2-22, this expression can in turn be rewritten as

$$\frac{\partial c_i^{int}}{\partial t}\left(1 + \frac{\phi^{bulk}}{\phi^{int}}\Xi_i^{-1}\right) = D_c \cdot \nabla^2 c_i^{int} - \frac{\phi^{bulk}}{\phi^{int}} c_i^{int}\frac{\partial \Xi_i^{-1}}{\partial t} \qquad (2\text{-}46)$$

which finally gives

$$\frac{\partial c_i^{int}}{\partial t} = \frac{D_c}{\left(1+\frac{\phi^{bulk}}{\phi^{int}}\Xi_i^{-1}\right)} \cdot \nabla^2 c_i^{int} - \frac{c_i^{int}}{\left(\frac{\phi^{int}}{\phi^{bulk}}+\Xi_i^{-1}\right)} \frac{\partial \Xi_i^{-1}}{\partial t} \tag{2-47}$$

Equation 2-47 is the equivalent of Fick's second law in the hybrid model. It is seen to depend explicitly on Ξ_i, which means that the evolution of species in the hybrid model is coupled (via f_D), although the underlying expression for the flux (Equation 2-39) is not. The first term on the right-hand side may be regarded as containing an "apparent" diffusivity, similar to what appears in models describing the combination of diffusion and sorption (see e.g. Bourg and Tournassat 2015)

$$D_i^* = \frac{D_c}{\left(1+\frac{\phi^{bulk}}{\phi^{int}}\Xi_i^{-1}\right)} \tag{2-48}$$

In the context of the hybrid model, the "sorption" process is the accumulation of ions in the bulk water porosity, which is assumed to be disconnected and stagnant, and hence functions as an "immobilizer". This conceptual view contrasts with traditional models, where diffusion occurs along a bulk connected porosity, while exchange reactions with the interlayer represent the sorption/retardation. Note that different ions are distributed between bulk and interlayer according to their ion equilibrium coefficient (Equation 2-22). Thus, the "apparent" diffusivity in the hybrid model is generally different for each ion. For cations, which typically have values of Ξ_i considerably larger than unity, this "sorption" becomes small ($D^* \approx D_c$). On the contrary, the "sorption" effect can become substantial under circumstances where Ξ_i becomes small, i.e. for anions when the Donnan potential is large.

Note that the issues of coupling of the concentration evolutions as well as the bulk porosity "sorption" mechanism both are specific to the hybrid model. In the limit of vanishing bulk porosity, these effects disappear and Equation 2-47 reduces to the ordinary Fick's second law

$$\frac{\partial c^{int}}{\partial t} = D_c \cdot \nabla^2 c^{int} \tag{2-49}$$

It is also important to note that even in the case of neutral species, for which Ξ may be close to unity, there is some retardation, which is quantified by the ratio between bulk and interlayer porosities. It results from this that the choice of the partition of porosity between bulk and interlayer has implications for conservative diffusion of species.

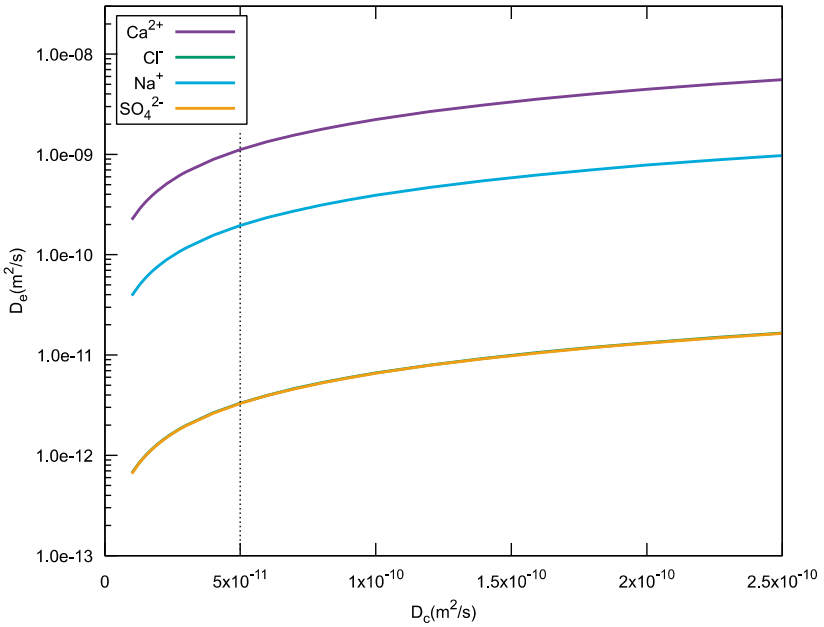

Figure 2-5. *D_e as a function of D_c for species with different charges, as evaluated in a tracer through-diffusion setup. The chloride effective diffusion (green line) is superimposed to that of sulfate (yellow line) and is thus not visible.*

2.5 Aqueous chemistry

2.5.1 Bulk water and interaction with mineral dissolution/precipitation

Bulk water chemistry and its interaction with mineral dissolution/precipitation in the hybrid model follows the classical representation of single bulk porosity geochemical models of bentonite (e.g. Arcos et al. 2003, Curti and Wersin 2002). Therefore, it will not be further discussed in this document.

2.5.2 Interlayer water

The description of the interlayer aqueous solution, presented in sections 2.1.2 and 2.4 makes no special assumptions regarding its chemistry, and it cannot be excluded that interlayers are chemically active. Although the model presented in this report does not consider chemical reactions occurring within the interlayer solution, a brief discussion about potential interlayer chemistry is attempted.

First, it is worth mentioning that there remain large uncertainties concerning the processes governing the fate of ions within the interlayer space. This space has dimensions approaching the molecular scale and is confined by charged silicate surfaces with somewhat heterogeneous charge distribution. Thus, chemistry and in general the behaviour of charged species in the interlayer will probably be significantly affected in comparison to bulk water solution.

Nonetheless, with the assumptions made in Section 2, the description of a chemical reaction in an interlayer is the same as in an ordinary aqueous solution. Writing a general chemical reaction as

$$\sum \nu_i \cdot M_i = 0 \qquad (2\text{-}50)$$

Where ν_i is the stoichiometric coefficient for species M_i (ν_i is negative for reactants and positive for products), the equilibrium condition in an interlayer is (law of mass action):

$$K = \prod \left(a_i^{int}\right)^{\nu_i} \qquad (2\text{-}51)$$

where K denotes the equilibrium constant for the reaction. It is easy to see that K is the same constant as the one used for the reaction in an ordinary aqueous solution by considering the interlayer in equilibrium with such a system.

The relation between external and internal activities in such a case is given by Equation 2-13. Rewriting Equation 2-51 in terms of external activities gives

$$K^{int} = \prod \left(f_D^{-z_i}\right)^{\nu_i} \cdot (a_i^{ext})^{\nu_i} = K^{ext} \cdot f_D^{-\sum z_i \cdot \nu_i} = K^{ext} \cdot (f_D)^0 = K^{ext} \qquad (2\text{-}52)$$

where it is assumed that charge is conserved in the reaction ($\sum z_i \cdot \nu_i = 0$). It is thus shown that the equilibrium constants to be used for interlayer chemistry are the same as those applicable for ordinary aqueous solutions ($K^{int} = K^{ext} = K$). In other words, existing thermodynamic databases of equilibrium constants can be directly used also for interlayer chemistry. However, it is noted that interlayer water is characterized by a high ionic strength (aprox. 3M for a water content of 0.3 kg/kg) and can thus show significantly different activity coefficients compared to the bulk solution. This can affect the suitability of the activity coefficient model used in a given thermodynamic database.

Notice that the result that equilibrium coefficients are unchanged in an interlayer chemical environment was derived by assuming equilibrium with an external solution. When dealing with interlayer chemistry generally, however, no such assumption is required (the equilibrium constants to be used are still the same). As a matter of fact, no reference to external solutions is at all necessary.

2.5.3 Sorption processes

Traditionally, two types of processes have been treated as sorption processes when modelling bentonite: ion exchange and (edge-site) surface complexation. A major feature in the hybrid model is that ion exchange no longer is treated as sorption, but is accounted for by the ion equilibrium framework.

Surface complexation reactions on edge-sites, on the other hand, would need to be considered. This type of reaction may be written as

$$\equiv SOH + H^+ \rightarrow \equiv SOH_2^+ \quad (2\text{-}53)$$

where $\equiv S$ represents the edge-site.

A major and open question is what type of activities should enter the law of mass action for the above reaction:

$$\frac{a_{\equiv SOH_2^+}}{a_{\equiv SOH} \cdot a_{H^+}} = K \quad (2\text{-}54)$$

In this work, surface complexation reactions have not been studied using the hybrid model and will not be discussed further in that context. However, the effect of considering surface complexation reactions on the montmorillonite edge-sites was evaluated using the traditional reactive transport modelling approach in the Base Case model and in a variant case that considers interface metal corrosion (see sections 6.3.4 and 7.2.1, respectively).

3 Hybrid model implementation

The hybrid model for reactive transport in compacted bentonite is implemented with iCP (Nardi et al. 2014), an interface between Comsol Multiphysics (COMSOL 2015) and Phreeqc (Parkhurst and Appelo 2013). iCP is written in Java and uses the IPhreeqc C++ dynamic library and the COMSOL Java-API. The IPhreeqc library (Charlton and Parkhurst 2011) incorporates all the features of Phreeqc. In this implementation, the transport of solutes and other coupled physical processes are calculated in Comsol, while chemical reactions are solved in Phreeqc. iCP follows an operator splitting method to couple physical and chemical processes using a sequential non-iterative approach (SNIA). The chemical step in Phreeqc considers all chemical reactions between the bulk porosity solution and the minerals in the system. The interface then retrieves the bulk concentrations ($c_{i,bulk}$) and activity coefficients ($\gamma_{i,bulk}$) of each aqueous species i included in the model, calculated by Phreeqc in the last time step. These concentrations are used as input for the Comsol model and are equilibrated with the interlayer water. In turn, bulk activity coefficients are used for calculating the Donnan factor (f_D).

Two different physics are solved in Comsol: *solute transport* and *Donnan equilibrium.* In the hybrid model implementation for compacted bentonite, Fickian diffusion in the interlayer porosity is solved for in Comsol, while the bulk pores are considered as stagnant water. This solute transport physics also accounts for diffusion in other porous media that may be in contact with bentonite (e.g. a porous rock). These other domains may have only a single bulk porosity, and therefore their interface with compacted bentonite requires special treatment (see below). All these processes are solved for in the solute transport physics in Comsol.

Comsol also solves the Donnan equilibrium between the interlayer water and the bulk pore water of the compacted bentonite domain, as detailed in Section 2.3.

A schematic summary of the implementation is shown in Figure 3-1.

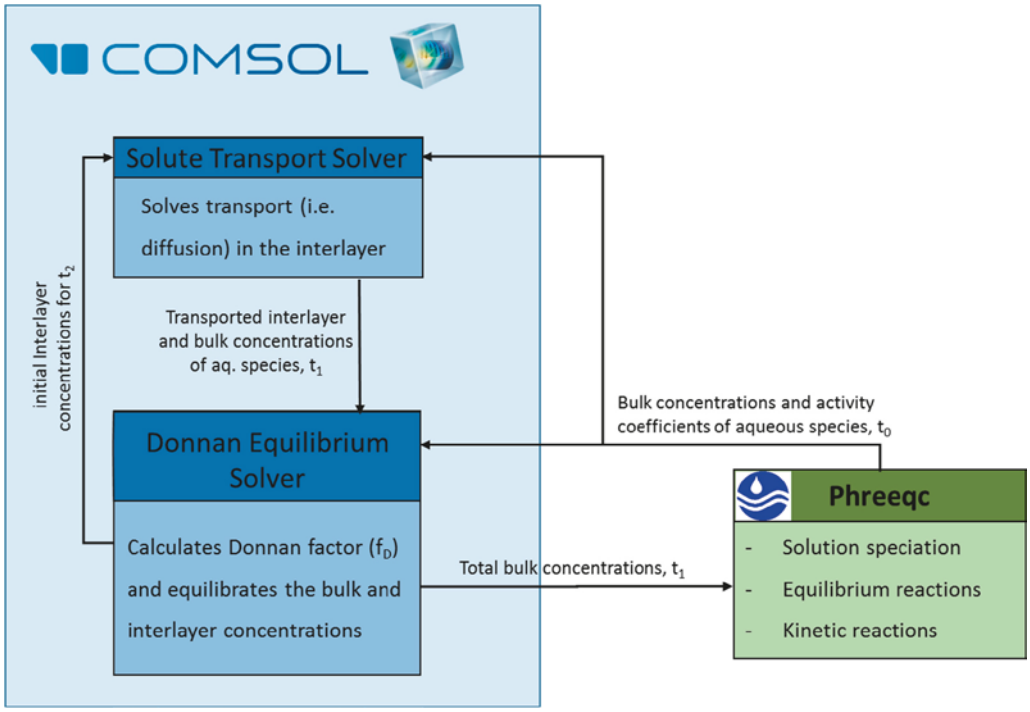

Figure 3-1. *Scheme of the iCP implementation of the hybrid model.*

3.1 Solute transport solver

In this step, Fickian diffusion transport of every aqueous species is calculated. Two types of domains are considered in the hybrid model:

- Compacted bentonite, which has a cation exchange capacity (CEC) and for which transport occurs in the interlayer water. In this domain, the bulk water is stagnant and is in Donnan equilibrium with the interlayer water at each given point. The transported variables are $c_{i,int.}$
- Other single bulk porous media that do not have a structural charge imbalance. In these materials, there is no interlayer water and transport occurs in the bulk water. The transported variables are therefore $c_{i,bulk.}$

Due to the cation exchange capacity of the clay, if it is in contact with another porous medium there will be an electrostatic potential difference between the interlayer water of the clay and the porewater of the other material. The interlayer water in the clay has a high amount of cations due to the negative charge of the clay, while the porewater is charge balanced. This electrostatic potential difference is quantified through the Donnan factor, f_D.

At each interface between compacted bentonite and other porous media, Donnan equilibrium is solved at the boundary. If N is the number of transported species, there are $2 \cdot N + 1$ unknowns to be solved at these boundaries: the Donnan factor ($f_{D,b}$), the interlayer concentrations in the clay ($c_{i,int,b}$) and the bulk concentrations in the domain without CEC ($c_{i,bulk,b}$), with subscript b referring to concentrations at the boundary. These unknowns are solved with a set of $2 \cdot N + 1$ algebraic equations. The first one is the equation for the Donnan factor (similar to Equation 2-21):

$$\sum_i z_i \cdot \frac{\gamma_i^{bulk}}{\gamma_i^{int}} \cdot f_{D,b}^{-z_i} \cdot c_{i,bulk,b} = c_{IL} \tag{3-1}$$

where γ_i^{bulk} is the bulk activity coefficient of a species i as retrieved from Phreeqc (i.e. from the previous time step). γ_i^{int} on the other hand, is the interlayer activity coefficient of species i and is specified in Comsol, as well as the parameter c_{IL}.

There are N equations, one for each species, that define the Donnan equilibrium between the interlayer and bulk concentrations:

$$c_{i,int,b} = \Gamma_i \cdot f_{D,b}^{-z_i} \cdot c_{i,bulk,b} \tag{3-2}$$

Finally, there are N additional equations, one for each species, that ensure mass conservation. For this purpose, two cells are set, one directly to the left of the boundary, between points b_l and b in Figure 3-2, and another one directly to the right, between points b and b_r.

The equation of mass conservation for species i is the following:

$$j_{i,in} - j_{i,out} - \frac{dN_i}{dt} = 0 \tag{3-3}$$

where $j_{i,in}$, $j_{i,out}$ and N_i are the influx of species i through b_l, its outflux through b_r, and the total amount of moles between b_l and b_r, respectively. These quantities are calculated as follows:

$$j_{i,in} = -\phi_{int} D_p \frac{dc_{i,int(b\_l)}}{dx} \tag{3-4}$$

$$j_{i,out} = -\phi_{bulk} D_p \frac{dc_{i,bulk(b\_r)}}{dx} \tag{3-5}$$

$$N_i = \int_{b\_l}^{b} \phi_{int} c_{i,int} + \int_{b}^{b\_r} \phi_{bulk} c_{i,bulk} \tag{3-6}$$

where ϕ_{int} and ϕ_{bulk} are the interlayer porosity of the clay and the bulk (or total) porosity of the other domain, respectively. D_p, on the other hand, is the pore diffusion coefficient. Note that in this case, bentonite is considered at the left of the boundary.

At each time step, the initial clay interlayer concentrations are obtained from the Donnan equilibrium solver of the previous time step. The initial bulk concentrations for the other materials are retrieved directly from Phreeqc. At the end of the transport step, the transported interlayer concentrations are obtained for the bentonite ($c_{i,int}$), and the bulk concentrations for the other domains ($c_{i,bulk}$).

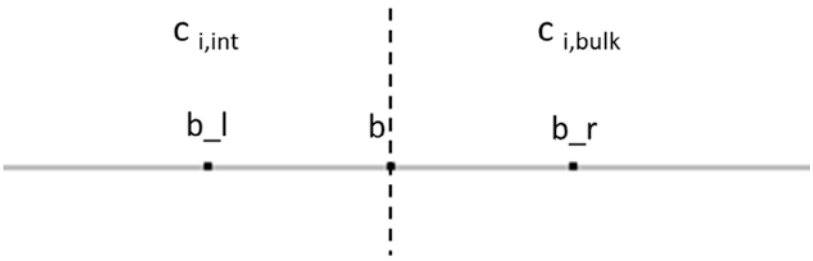

Figure 3-2. *Implementation of the boundary between a compacted bentonite domain (left) and a porous media with only bulk porosity (right).*

3.2 Donnan equilibrium solver

In this step, the compositions of the bulk and interlayer pore solutions of the bentonite are equilibrated. Similar to the case of an interface between the bentonite and another material, within the clay there is an electrostatic potential difference between the bulk pores and the interlayer water.

It is noted that Donnan equilibrium depends on the charge of the species. Therefore, it must be calculated for each individual species. On the other hand, the chemical reaction step performed within Phreeqc after the Donnan equilibrium calculation requires chemical element (e.g. Na, Ca, S, etc.) concentrations as input. Therefore, a total of $2 \cdot N + M + 2$ algebraic equations are solved, where N is the number of transported species and M is the number of chemical elements. The unknowns are the (spatially variable) Donnan factor, the equilibrated interlayer and bulk concentrations of each aqueous species (c_{i,int_e} and $c_{i,bulk\_e}$), the total bulk concentrations of the different chemical elements, and the charge balance of the bulk solution.

The Donnan factor is calculated with the following expression, similar to Equation 3-1:

$$\sum_i z_i \cdot \frac{\gamma_i^{bulk}}{\gamma_i^{int}} \cdot f_D^{-z_i} \cdot c_{i,bulk\_e} = c_{IL} \tag{3-7}$$

Two additional equations are required to calculate the equilibrated bulk and interlayer concentrations of each species. First, both concentrations should comply with the Donnan equilibrium requirement, i.e.:

$$c_{i,int\_e} = \Gamma_i \cdot f_D^{-z_i} \cdot c_{i,bulk\_e} \tag{3-8}$$

In addition, the total mass of each species must be conserved, which reads:

$$\phi_{bulk} \cdot \left(c_{i,bulk} - c_{i,bulk\_e}\right) + \phi_{int} \cdot \left(c_{i,int} - c_{i,int\_e}\right) = 0 \tag{3-9}$$

where $c_{i,bulk}$ is the bulk concentration of species i retrieved from Phreeqc from the previous time step (t_0) and $c_{i,int}$ is the corresponding interlayer concentration after the transport step (t_1).

The resulting set of c_{i,int_e} is used as initial condition for the transport in the interlayer of the next time step. In turn, the equilibrated bulk concentrations ($c_{i,\ bulk\_e}$) are used to calculate the total bulk concentration of the different chemical elements. For domains that do not have CEC, in this step the only calculation performed is to obtain the total concentration of each element with the species bulk concentrations obtained from the transport solver. All these total concentrations in the modelled domains at time t_1 are then used by Phreeqc to perform the chemical reaction step at time t_1.

4 Experimental data

In this section, available experimental data to be used as input in the hybrid model are collected and discussed. In particular, this data collection concerns the choice of interlayer activity coefficients.

4.1 Cations

The definition of the selectivity coefficient using the Gaines-Thomas convention (e.g. Sposito 1981) gives for the calcium/sodium pair

$$\frac{X_{Ca}}{X_{Na}^2} = K_{GT}^{Na/Ca} \cdot \frac{a_{Ca}^{ext}}{\left(a_{Na}^{ext}\right)^2} \tag{4-1}$$

with (see Section 2.3.4)

$$K_{GT}^{Na/Ca} \approx 2c_{IL} \frac{\left(\gamma_{Na}^{int}\right)^2}{\gamma_{Ca}^{int}} \tag{4-2}$$

Thus, according to ion equilibrium theory, plotting X_{Ca}/X_{Na}^2 against $a_{Ca}^{ext}/\left(a_{Na}^{ext}\right)^2$ for a given system (given c_{IL}) should give a straight line whose slope (K_{GT}) can be related to the interlayer activity coefficients for sodium and calcium. Formulas (4-1) and (4-2) can of course be equally applied to the magnesium/sodium pair.

Another relation of practical importance is for the calcium/magnesium pair

$$\frac{X_{Ca}}{X_{Mg}} = K_{GT}^{Mg/Ca} \cdot \frac{a_{Ca}^{ext}}{a_{Mg}^{ext}} \tag{4-3}$$

with K_{GT} in this case being

$$K_{GT}^{Mg/Ca} = \frac{\gamma_{Mg}^{int}}{\gamma_{Ca}^{int}} \tag{4-4}$$

4.1.1 Compacted systems

Reported equilibration studies between a bulk solution and bentonite performed on compacted systems, to which unambiguous values of c_{IL} can be attributed, are scarce. Muurinen and Lehikoinen (1999) report a large set of equilibration tests between initially specified external solutions and compacted clay samples. The variables of the tests were not only the bentonite density, but also the ratio between clay mass and external solution volume was varied.

Data from the study of Muurinen and Lehikoinen (1999) have been used to plot Equation 4-1 and 4-3 for MX-80 bentonite at a density of 1.5 g/cm^3 and is presented in Figure 4-1. This figure confirms that the relations are indeed linear. The slope of these curves quantifies the selectivity coefficient for the corresponding pair of ions, and can thus be used to evaluate the relations between interlayer activity coefficients given by Equations 4-2 and 4-4.

Table 4-1 summarizes the selectivity coefficients and corresponding interlayer activity coefficients ratios evaluated from Muurinen and Lehikoinen (1999) and from Karnland et al. (2011). The study by Karnland et al. (2011) was performed on pure montmorillonite (derived from MX-80 bentonite) and considered only calcium/sodium. Only data judged to represent equilibrium, and which did not show negligible concentrations of the considered ions (> 1mM) was used for the evaluation presented in Table 4-1.

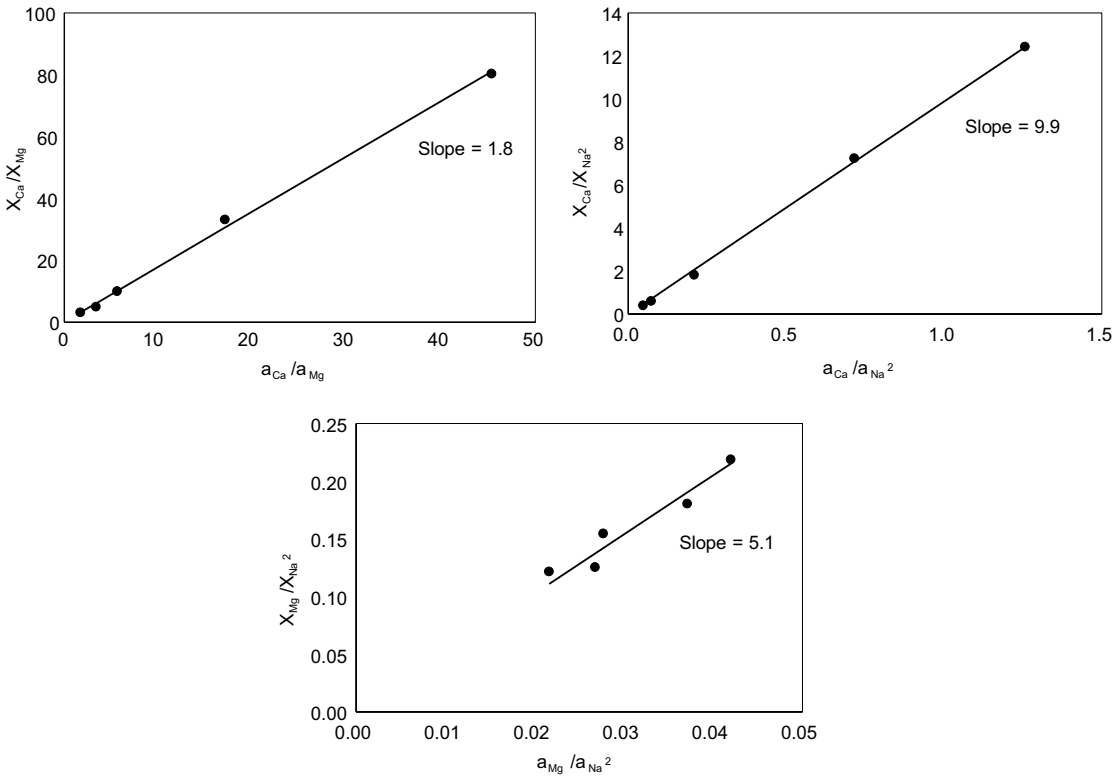

Figure 4-1. Relations between interlayer occupancy and external ion activities in a subset of the tests reported in Muurinen and Lehikoinen (1999). The samples are all MX-80 bentonite at a density of 1.5 g/cm³.

Table 4-1. Selectivity coeffcients and corresponding interlayer activity ratios as evaluated from data in: [1] Muurinen and Lehikoinen (1999) and [2] Karnland et al. (2011).

Reference	ρ_d (g/cm³)	c_{IL}	$K_{GT}^{Na/Ca}$	$(\gamma_{Na}^{int})^2/\gamma_{Ca}^{int}$	$K_{GT}^{Na/Mg}$	$(\gamma_{Na}^{int})^2/\gamma_{Mg}^{int}$	$K_{GT}^{Mg/Ca}$
[1]	1.5	2.5	9.9	2.0	5.1	1.0	1.8
[1]	1.2	1.6	9.0	2.8	5.6	1.8	1.6
[1] WyNa	1.5	2.8	5.7	1.0	-	-	-
[2]	1.5	3.3	8.4	1.3	-	-	-
[2]	1.25	2.2	10.6	2.4	-	-	-
[2]	1.0	1.5	7.9	2.6	-	-	-

4.1.2 Dispersed systems

Most studies on cationic equilibrium (selectivity measurements) have been performed on dispersed systems which are separated into a “clay phase” and a supernatant. In these studies, it is not meaningful to associate a parameter c_{IL} to the clay phase, although Equation 4-1 may still have validity.

Figure 4-2 shows data from two studies – Sposito et al. (1983) and Itälä and Muurinen (2012) – plotted in accordance with Equation 4-1. Although these plots resemble linear relationships, the data is seen to be rather scattered. As the data does not show any systematic deviation from linearity, however, it can be reasonably be concluded that the scatter should be attributed to experimental uncertainty rather than indicating deviation from the relation expressed by Equation 4-1.

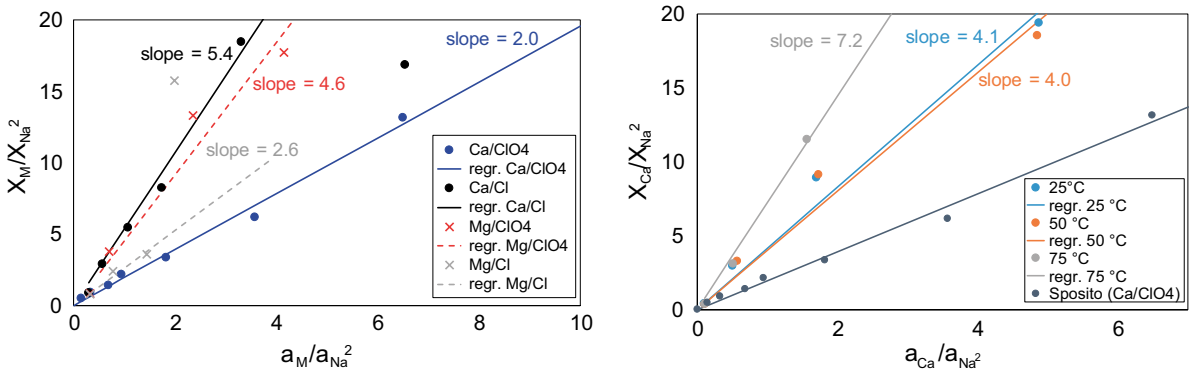

Figure 4-2. *Left: Equation 4-1 plotted using data from Sposito et al. (1983). This study presents equilibrium at 25 °C for both Ca/Na and Mg/Na in pure montmorillonite, performed at constant normality (0.05 N) using either ClO_4 and Cl as background. Right: Similar plots using data from Itälä and Muurinen (2012). The tests were performed at three different temperatures and all used ClO_4 as background (0.1 N).*

In Table 4-2, selectivity coefficients evaluated from the data plotted in Figure 4-2 are presented. In addition, this table lists selectivity coefficients for calcium/sodium and magnesium/sodium evaluated by equilibrating "natural" bentonites in deionized water (Bradbury and Baeyens 2002, Fernández et al. 2004). Naturally, such an evaluation is quite complex, involving several different types of anions and cations, as well as various accessory mineral phases. In addition, this type of evaluation does not probe the full isotherm but rather represent a "snapshot" of a given cation population in the clay.

Comparing the values listed in Table 4-1 and Table 4-2 there appears to be a tendency of higher selectivity coefficients in compacted systems for calcium/sodium and magnesium/sodium. It must be kept in mind, however, that the experimental uncertainty underlying these numbers is rather large.

Table 4-2. Selectivity coefficents evaluated from reported data in dispersed systems. Data from [1] Itälä and Muurinen (2012), [2] Sposito et al. (1983), [3] Bradbury and Baeyens (2002), and [4] Fernández et al. (2004). d.w. = deionized water.

Reference	T (°C)	Clay type	Solution	$K_{GT}^{Na/Ca}$	$K_{GT}^{Na/Mg}$	$K_{GT}^{Mg/Ca}$
[1]	25	Montmorillonite (Wyoming)	ClO_4	4.1	-	-
[1]	50	Montmorillonite (Wyoming)	ClO_4	4.0	-	-
[1]	75	Montmorillonite (Wyoming)	ClO_4	7.2	-	-
[2]	25	Montmorillonite (Wyoming)	ClO_4	2.0	4.6	1.0
[2]	25	Montmorillonite (Wyoming)	Cl	5.4	2.6	-
[3]	25	MX-80 Bentonite	d.w.	2.6	2.2	
[4]	25	FEBEX Bentonite	d.w.	12.8	10.7	

In summary, it can be concluded that existing experimental data on Ca/Na selectivity coefficients has a large range of uncertainty, with values spreading in the range 3 – 13. There is certainly a need to further assess this uncertainty, and to perform additional tests which better comply with expected repository conditions.

4.1.3 Cation content in MX-80

For modelling purposes, it is important to have a well specified initial state of the material, particularly with respect to the initial cation content. Obviously, knowledge of clay cation population is also essential for any type of ion equilibrium evaluation. Table 4-3 gathers reported experimentally determined cation populations of MX-80 bentonite. Again, it may be observed that even though all measurements indicate a sodium dominated system, relatively large discrepancies are found between the different studies.

Table 4-3. Cation population of MX-80 as determined in various studies.

Reference		CEC	Na (%)	Ca (%)	Mg (%)	K (%)
(Müller-Vonmoos and Kahr 1983)		0.76	86	10	4	0
(Bradbury and Baeyens 2002)		0.79	85	8	5	2
(Carlsson 2004)		0.84	65	24	8	3
(Karnland et al. 2006)	(1980)	0.76	83	9	6	2
	(mid 90)	0.75	71	21	6	2
	(2001)	0.75	72	18	8	2
(Kumpulainen and Kiviranta 2010)		0.85	69	23	7	2
(Kumpulainen and Kiviranta 2011)		0.84	62	27	9	2
(Dohrmann et al. 2013)		0.85	69	24	8	2

4.2 Anions

4.2.1 Chloride

Only data from equilibration of compacted systems with an external solution are relevant for evaluating interlayer activity coefficients. Such studies are scarce, but the case of NaCl in compacted purified montmorillonite has been studied by Muurinen and co-workers (Muurinen et al. 2004, 2007, Muurinen 2006). The ion equilibrium can in this simple case be treated analytically and the ion equilibrium coefficient for chloride reads

$$\Xi_{Cl} = -\frac{c_{IL}}{2 \cdot c^{ext}} + \sqrt{\frac{c_{IL}^2}{4 \cdot (c^{ext})^2} + \Gamma_{Na} \cdot \Gamma_{Cl}} \tag{4-5}$$

Thus, the product $\Gamma_{Na} \cdot \Gamma_{Cl}$ can be determined by measuring Ξ_{Cl}. By calculating the activity coefficients in the external concentrations (which is achievable using conventional tools), knowledge of this activity coefficient product gives an estimate of the interlayer activity coefficient product $\gamma_{Na}^{int} \cdot \gamma_{Cl}^{int}$, as

$$\gamma_{Na}^{int} \cdot \gamma_{Cl}^{int} = \frac{\gamma_{Na}^{ext} \cdot \gamma_{Cl}^{ext}}{\Gamma_{Na} \cdot \Gamma_{Cl}} \tag{4-6}$$

Figure 4-3 shows measured chloride concentrations in montmorillonite samples of various densities equilibrated by NaCl solutions in the range 0.1 M – 3.0 M (Muurinen et al. 2004, Muurinen 2006).

Figure 4-3 reveals that the data is rather scattered for low external concentrations (0.1 M and 0.3 M), and an evaluation of $\gamma_{Na}^{int} \cdot \gamma_{Cl}^{int}$ will consequently suffer from the same type of uncertainty. However, the consistency of measured chloride concentrations in the clay in the case of external solution 0.1 M NaCl was evaluated in (Muurinen et al. 2007). In this study, a set of samples were prepared in different ways and the corresponding chloride concentration was measured. In particular, the difference was tested of first water saturating samples using deionized water before contacting them with the saline solution, or by directly saturating the samples with the saline solution. The results of this study are plotted in Figure 4-4. This figure shows that samples pre-equilibrated with deionized water give very similar values of the clay chloride concentration, while samples which were directly saturated with saline solution contain considerably more chloride. This behaviour demonstrates that a substantial amount of time may be needed for samples to reach equilibrium and that one should be careful in interpreting results from these types of "equilibration" studies.

It is assumed here that the samples pre-saturated with deionized water better represent the equilibrium situation. This is motivated both by the fact that such a sample preparation is a priori expected to be closer to equilibrium (saline water is not "dragged" into the sample during water saturation), and by the reasonable "shape" of the corresponding chloride concentration vs. dry density curves. Note that the chloride content in the samples directly contacted with saline solution (series D) starts to increase at (very) high densities – a behaviour that is difficult to motivate from a thermodynamic perspective. This behaviour is also observed in the data for 0.1 M and 0.3 M in Muurinen (2006), see Figure 4-3.

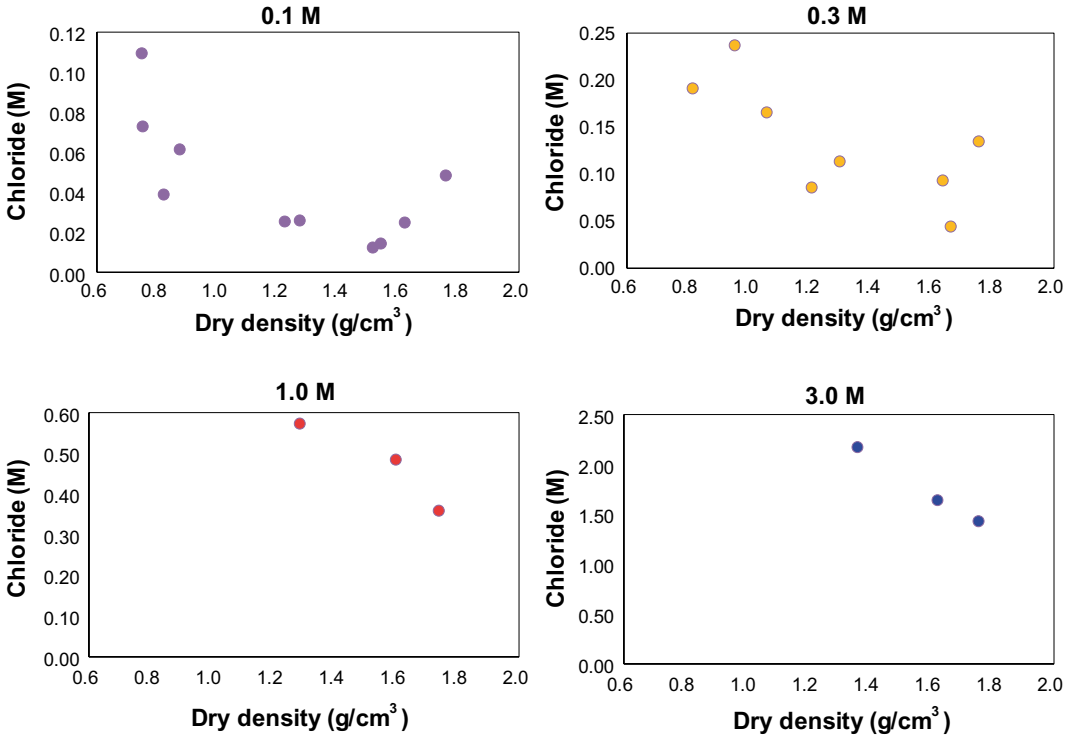

Figure 4-3. *Measured chloride concentrations in montmorillonite samples equilibrated by NaCl solutions of concentrations 0.1 M, 0.3 M, 1.0 M, and 3.0 M. Data from Muurinen (2006).*

Figure 4-5 displays values of $\gamma_{Na}^{int} \cdot \gamma_{Cl}^{int}$ as evaluated from the data presented in Figure 4-3 and Figure 4-4 (using Equations 4-4 and 4-5). These values show substantial amount of scatter – especially for lower values of external concentration. As discussed above, however, much of this scatter is due to samples which are expected to not be fully equilibrated. From that discussion, it is clear that the upper range of the $\gamma_{Na}^{int} \cdot \gamma_{Cl}^{int}$ values at 0.1 M and 0.3 M best represent equilibrium conditions. Therefore, available experimental data on NaCl equilibrium in montmorillonite samples suggests that $\gamma_{Na}^{int} \cdot \gamma_{Cl}^{int}$ remains approximately constant (at least for external concentrations below 1.0 M), with a value in the range 0.2 – 0.3.

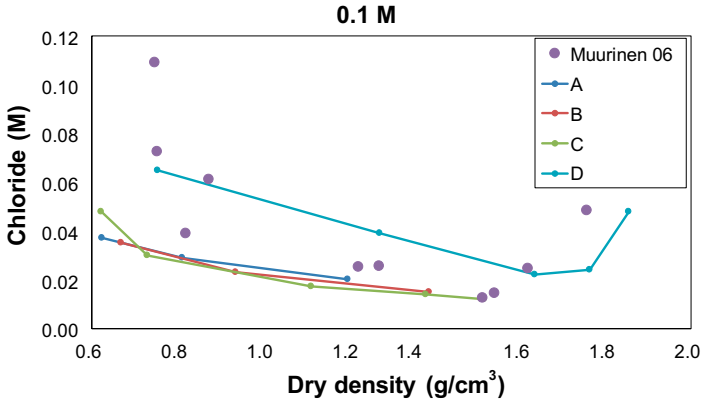

Figure 4-4. *Resulting chloride concentration in montmorillonite samples after "equilibrating" them with 0.1 M NaCl solution. Series A, B, C were all pre-saturated with deionzied water before contacted with the saline solution, while series D was directly contacted with the saline solution in an unsaturated condition. Data from Muurinen et al. (2007). Also plotted are corresponding chloride concentrations reported in Muurinen (2006) for the same external NaCl concentration.*

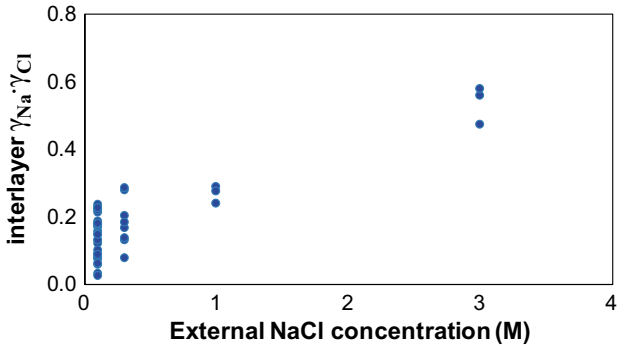

Figure 4-5. *Resulting values of $\gamma_{Na}^{int} \cdot \gamma_{Cl}^{int}$ using Equation 4-5 and 4-6, and data in Muurinen (2006) and Muurinen et al. (2007) (Figure 4-3 and Figure 4-4).*

4.2.2 Sulfate

An evaluation of interlayer activity coefficients for sulfate species has been performed elsewhere (Birgersson 2019). The analysis is based on diffusion data on gypsum dissolving (and diffusing) in a compacted sample of initially pure Na- or Ca-montmorillonite. The derived values of interlayer activity coefficients for sulfate and calcium and sodium sulfate pairs are listed in Table 4-4. Although it is difficult in the analysis to differ between the species SO_4^{2-} and $NaSO_4$, it is clear that very low values of their interlayer activity coefficients are required in order to accommodate the relatively large sulfate fluxes observed in these tests.

Table 4-4. Interlayer activity coefficients of sulfate species as evaluated in Birgersson (2019).

Species	γ^{int}
SO_4^{2-}	0.03
$NaSO_4^-$	0.07
$CaSO_4^0$	1.413

5 Model verification

A series of verification cases are given in this section aimed at improving the understanding about the qualitative effect of using the hybrid model on reactive transport processes. Chemical equilibrium, solute transport and their coupling are tested in separate cases, which are summarized in Table 5-1. Note that, given the lack of experimental data, no quantitative model validation is pursued. Instead, the focus of this section is on the qualitative consistency with the conceptualization described in previous sections.

Table 5-1. Summary of verification cases.

Test case	Description	Purpose	Test variable	Conclusion
Case 1: Na/Ca-montmorillonite with anhydrite (Section 5.1)	Batch simulations: equilibrium between anhydrite and montmorillonite with different Na/Ca ratios in the exchanger (interlayer) and pure bulk water.	Evaluate the qualitative behaviour of the hybrid model (HM) with respect to chemical equilibrium as compared to exchanger and pure interlayer models.	• Anhydrite dissolution; • sulfate concentration	The results of the HM depend on the partitioning between bulk and interlayer waters. In the limit of mostly bulk water, the HM is comparable to a cation exchange model. In the limit of mostly interlayer water, the HM resembles a pure interlayer model.
Case 2: Only transport (Section 5.2.1)	1D model of pure Ca-montmorillonite with in-diffusion of $NaSO_4$.	Verify the implementation of Donnan equilibrium in iCP. Evaluate the effect of using the HM on species transport, as compared to a cation exchange model.	• Donnan factor • Component and species concentrations	The Donnan model is correctly implemented in iCP. The hybrid model results in faster cation transport but slows down anion diffusion.
Case 3: Transport and dissolution (Section 5.2.2)	1D model of pure Ca-montmorillonite + anhydrite with in-diffusion of $NaSO_4$.	Assess the qualitative differences of using different models (HM, exchanger, pure interlayer and interlayer diffusion in Phreeqc) on a reactive transport setup with mineral reactions.	• Anhydrite concentration	The use of a model that includes transport in the interlayer affects mineral reactions (dissolution in this case) due to faster/slower cation/anion diffusion.
Case 4: Solute transport (Section 5.3)	Tracer transport through 1D HM with different bulk/interlayer distributions. Performed with Comsol and iCP	Verify whether the HM displays the behaviour predicted by Equation 2-48. Verify the transport in iCP.	• Tracer concentration	A lower ratio of interlayer/bulk porosity partitioning results in slower tracer transport, as predicted by Equation 2-48. Solute transport has been implemented correctly in iCP.

5.1 Case 1: Na/Ca-montmorillonite with anhydrite

Here, a relatively simple system is defined for testing and analysis of the developed conceptual model. This system is defined to contain only montmorillonite and anhydrite ($CaSO_4$) under isothermal conditions (25 ºC), and the aqueous species accounted for are Na^+, Ca^{2+}, SO_4^{2-}, $NaSO_4^-$ and $CaSO_4^0$. The chemical reactions considered are that for anhydrite dissolution:

$$CaSO_4(s) \rightarrow Ca^{2+} + SO_4^{2-} \qquad \log K_{anhydrite} = -4.28 \qquad (5\text{-}1)$$

and those for ion pair formation:

$$Ca^{2+} + SO_4^{2-} \rightarrow CaSO_4^0 \qquad \log K_{CaSO_4^0} = 2.25 \qquad (5\text{-}2)$$

$$Na^{+} + SO_4^{2-} \rightarrow NaSO_4^- \qquad \log K_{NaSO_4^-} = 0.70 \qquad (5\text{-}3)$$

The initial anhydrite solid mass fraction is x_{anh} = 0.01. This value is chosen large enough so that the source of anhydrite is not exhausted as the system equilibrates, but small enough to have a negligible influence on the total solid mass. The montmorillonite solid mass fraction is consequently set to x_{mmt} = 0.99. The cation exchange capacity of the system is set to 0.9 eq/kg, and the water-to-solid mass ratio is 0.3. A summary of the initial system specifications is shown in Table 5-2. The Na/Ca ratio of the cations compensating montmorillonite structural charge is assumed to be a variable parameter.

Table 5-2. Specification of the test system.

x_{mmt}	x_{anh}	w	ρ_s	ρ_w	CEC	ϕ_{tot}
(-)	(-)	(-)	(g/cm^3)	(g/cm^3)	(eq/kg)	(-)
0.99	0.01	0.3	2.75	1.0	0.9	0.452
Composition of the system (mol/kg solid)			**Na**	**Ca**	**SO_4**	
100 % Na in exchanger initially			0.90	0.073	0.073	
50 % Na in exchanger initially			0.45	0.298	0.073	
0 % Na in exchanger initially			0.00	0.523	0.073	

5.1.1 Phreeqc cation exchange model

A set of Phreeqc batch simulations was performed in which a given exchanger composition is equilibrated with a specified mass of anhydrite and pure bulk water, resulting in partial anhydrite dissolution. The anhydrite solubility, in terms of sulfate concentration, is then evaluated as a function of the initial exchanger composition.

The cation exchange reaction used to represent the montmorillonite interlayers is $2\ NaX + Ca^{2+} \rightleftarrows CaX_2 + 2\ Na^+$, where NaX and CaX_2 indicate sodium and calcium concentrations in the exchanger, respectively. The amount of exchange sites (X) is given by CEC/w = 3 mol/kg. This model also requires a choice of Ca/Na selectivity coefficient, which is set to $K_{Ca/Na}$ = 6.

The amount of dissolved sulfate is not only a function of the amount of sodium in the system, but also of the assumed amount of bulk water. Figure 5-1 shows the concentrations of sulfate species as a function of the amount of sodium initially present on the exchanger when all the water (0.3 kg bulk water/kg of solid, see Table 5-2) in the model is assumed to be bulk water, i.e. $\varphi^{bulk} = \varphi = 0.452$. For an initially pure sodium system, the total sulfate concentration is above 200 mM, while in the pure calcium system (0 % sodium), the anhydrite solubility is 26 mM.

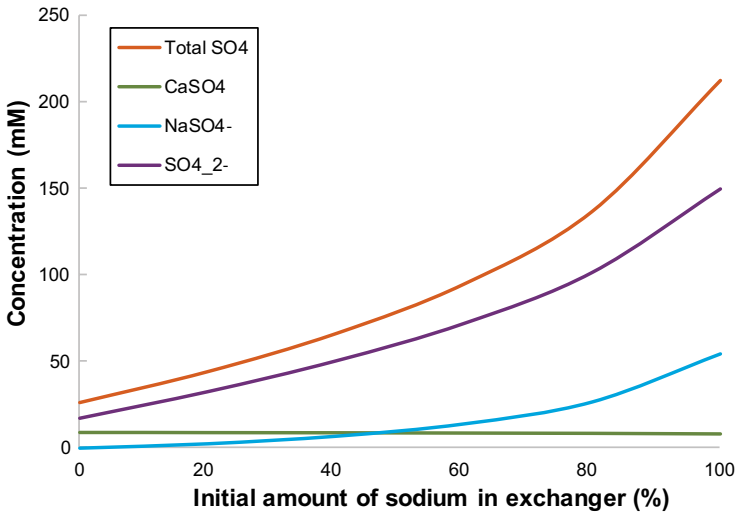

Figure 5-1. *Sulfate inventory at anhydrite equilibrium in the Phreeqc cation exchange model, assuming 100 % bulk water, or $\varphi^{bulk} = 0.452$.*

Figure 5-2 shows the same sulfate species concentrations assuming 32 % bulk water, corresponding to $\varphi^{bulk} = 0.145$ and a ratio of 0.096 kg of bulk water/kg of solid. Note that the total concentration of sulfate species is lower as compared to the previous case – in the limit of having an initially pure sodium system, total sulfate concentration has decreased by approximately a factor of 2. On the other hand, the actual concentrations in the bulk water has increased as compared to the case of having $\varphi^{bulk} = 0.452$.

Figure 5-3 shows the results for the case $\varphi^{bulk} = 0.014$, i.e. only 3 % bulk water (bulk water to solid mass ratio of $9 \cdot 10^{-3}$). Here, the bulk water concentrations become even larger, while total concentrations are very small as compared to the previous cases.

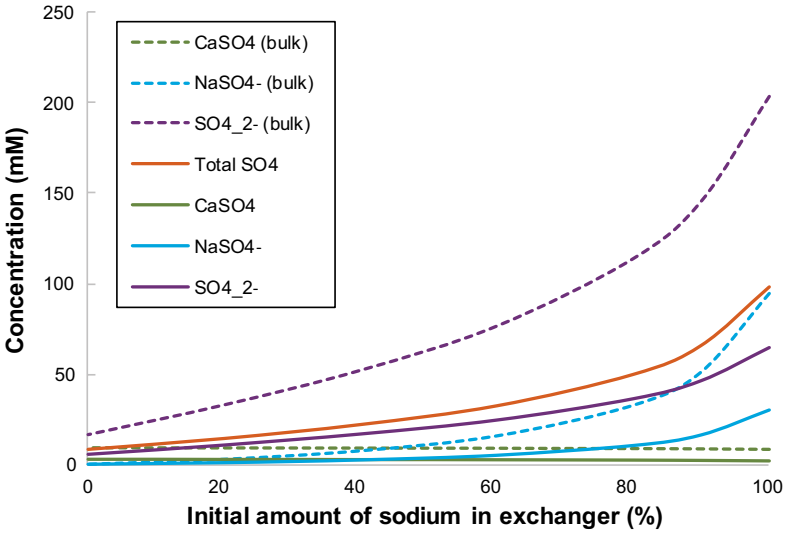

Figure 5-2. *Sulfate inventory at anhydrite equilibrium in the Phreeqc cation exchange model, assuming 32 % bulk water or $\varphi^{bulk} = 0.145$. Full lines show concentrations related to all water in the systems, while dotted lines show corresponding concentration in the bulk water phase.*

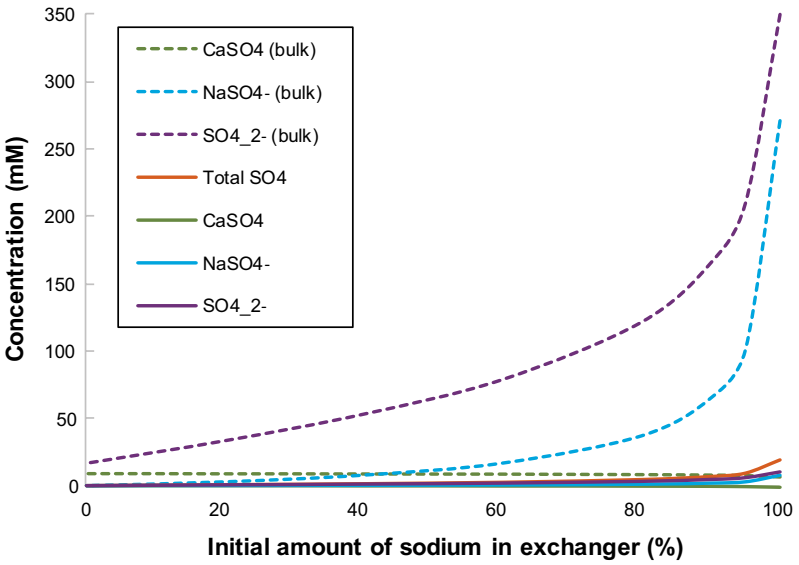

Figure 5-3. *Sulfate inventory at anhydrite equilibrium in the Phreeqc cation exchange model, assuming 3 % bulk water, or $\varphi^{bulk} = 0.014$. Full lines show concentrations related to all water in the systems, while dotted lines show corresponding concentration in the bulk water phase.*

5.1.2 Interlayer-only model

The possibility of considering that the entire porosity of the system is comprised by interlayer water is explored here ($\varphi^{int} = \varphi$). In this test case, mineral reactions are assumed to occur within the interlayer space, following the formulation discussed in Section 2.5.2. The purpose is to use these results for comparison with the hybrid model output in the limit of very small fractions of bulk water.

The process considered in the previous section – equilibration between anhydrite and pure Ca/Na-montmorillonite – is simple enough that it can be carried out analytically in an interlayer-only model, if the activity coefficients are assumed to be constant (chemical processes in interlayers are briefly considered in Section 2.5.2). This derivation is made here. Note that in the hybrid model, mineral dissolution and precipitation is assumed to take place in the bulk water only, whereas in this pure interlayer model it occurs in the interlayer water. The law of mass action for anhydrite dissolution reads

$$c_{Ca^{2+}}^{int} \cdot c_{SO_4^{2-}}^{int} = \frac{K_{anhydrite}}{\gamma_{Ca}^{int} \cdot \gamma_{SO_4}^{int}} \equiv \widetilde{K}_{anhydrite}, \tag{5-4}$$

where $\widetilde{K}_{anhydrite}$ is the equilibrium constant of anhydrite in the interlayer. This equation may be combined with that for $CaSO_4^0$ pair formation to yield

$$c_{CaSO_4^{2-}}^{int} = \frac{K_{anhydrite} \cdot K_{CaSO_4^0}}{\gamma_{CaSO_4}^{int}} \tag{5-5}$$

Under the assumption that the activity coefficient for the ion pair does not depend on the composition of the interlayer solution, Equation 5-5 shows that the concentration of $CaSO_4^0$ complexes are constant. The law of mass action for the formation of $NaSO_4^-$ ion pairs may similarly be written

$$c_{NaSO_4^-}^{int} = c_{Na^+}^{int} \cdot c_{SO_4^{2+}}^{int} \frac{\gamma_{Na^+}^{int} \cdot \gamma_{SO_4}^{int} \cdot K_{NaSO_4^-}}{\gamma_{CaSO_4}^{int}} = c_{Na^+}^{int} \cdot c_{SO_4^{2+}}^{int} \cdot \widetilde{K}_{NaSO_4^-} \tag{5-6}$$

The requirement of charge neutrality is furthermore stated

$$2 \cdot c_{Ca^{2+}}^{int} + c_{Na^+}^{int} - c_{NaSO_4^-}^{int} - 2 \cdot c_{SO_4^{2+}}^{int} = c_{IL} \tag{5-7}$$

Combining Equations 5-5 to 5-7 gives a second order equation for $c_{SO_4^{2+}}^{int}$

$$\left(c_{SO_4^{2-}}^{int}\right)^2 + c_{SO_4^{2-}}^{int} \frac{\left(c_{IL} - c_{Na^+}^{int}\right)}{\left(c_{Na^+}^{int} \cdot \widetilde{K}_{NaSO_4^-} + 2\right)} - \frac{2 \cdot \widetilde{K}_{anhydrite}}{\left(c_{Na^+}^{int} \cdot \widetilde{K}_{NaSO_4^-} + 2\right)} = 0 \tag{5-8}$$

with the solution

$$c_{SO_4^{2-}}^{int} = \frac{\left(c_{Na^+}^{int} - c_{IL}\right) + \sqrt{\left(c_{Na^+}^{int} - c_{IL}\right)^2 + 8 \cdot \widetilde{K}_{anhydrite} \cdot \left(c_{Na^+}^{int} \cdot \widetilde{K}_{NaSO_4^-} + 2\right)}}{2 \cdot \left(c_{Na^+}^{int} \cdot \widetilde{K}_{NaSO_4^-} + 2\right)} \tag{5-9}$$

Equation 5-9 gives the equilibrium concentration of the SO_4^{2-} species as a function of the interlayer concentration of the species Na^+. The total sodium concentration can be compared to the initial exchanger occupancy in the cation exchange model $[NaX]_{init}$ (Section 5.1.1). For 100 % sodium, $[NaX]_{init}$ = 3 mol/kg.

Figure 5-4 shows the solubility of anhydrite as a function of the initial amount of sodium in the interlayer (and can thus be directly compared with the plots in Section 5.1.1). For this plot, a specific choice of the interlayer activity coefficients is made, as listed in Table 5-3. The activity coefficients for sodium and calcium are chosen so that $\left(\gamma_{Na}^{int}\right)^2 / \gamma_{Ca}^{int} = 1$, giving a Ca/Na selectivity coefficient of $K_{Ca/Na}$ = 2 kg/mol x c_{IL} = 6 (Equation 2-38), which is the same value as used in the model of Section 5.1.1. Note that the evaluation of experimental data made in Section 4.1.1, suggests a value of $\left(\gamma_{Na}^{int}\right)^2 / \gamma_{Ca}^{int} \approx 2$ for compacted MX-80 bentonite. However, the point here is to have the same value of the Ca/Na selectivity coefficient in the different models for comparison.

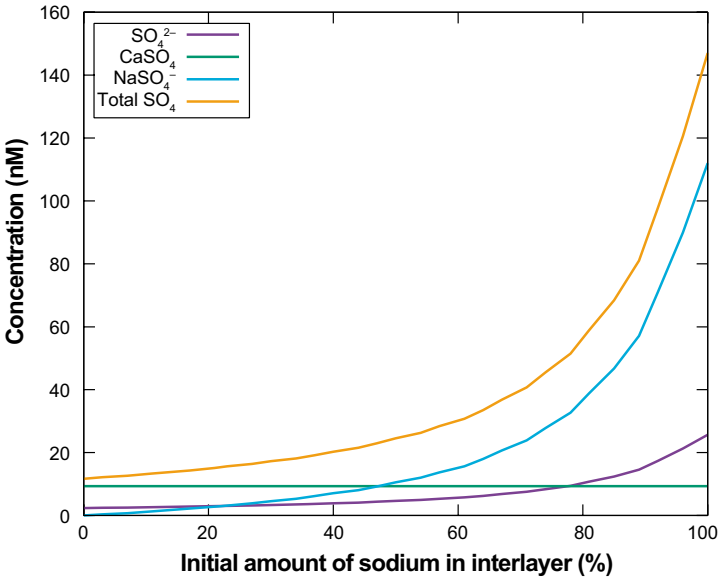

Figure 5-4. *Solubility of anhydrite in bentonite as a function of sodium content.*

The solubility of anhydrite differs in an interlayer as compared to pure water for two reasons: 1) due to possible presence of calcium cations required to compensate surface charge upon partial complexation between sodium and sulfate, and 2) due to differences in activity coefficients – the ionic strength is huge in the interlayer under all conditions, and for this reason alone it is expected that activity coefficients may differ strongly from their values at the solubility limit in pure water.

Note that the results derived in this section do not make any reference at all to a bulk solution, i.e. the ion equilibrium framework is not invoked.

Table 5-3. Chosen constant interlayer activity coefficients used in the calculation of anhydrite solubility in the interlayer-only model (Birgersson 2019).

$\gamma_{Ca^{2+}}^{int}$	$\gamma_{SO_4^{2-}}^{int}$	$\gamma_{Na^{+}}^{int}$	$\gamma_{NaSO_4^{-}}^{int}$	$\gamma_{CaSO_4^{0}}^{int}$
0.495	0.03	0.704	0.07	1.0

5.1.3 Hybrid model

Results from performing anhydrite equilibration in the hybrid model is displayed in Figure 5-5 for three choices of bulk water porosity, corresponding to 3 %, 32 %, and 91 % of the total amount of water. This figure shows the total amount of sulfate as a function of the initial amount of sodium in the interlayer. The results are also compared to the corresponding result of the interlayer-only model (Section 5.1.2) and the Phreeqc cation exchange model (Section 5.1.1). In order to get a relevant comparison, the calculations performed in the hybrid model have adopted the same values of interlayer activity coefficients as was used in the pure interlayer model (Table 5-3). Furthermore, the activity coefficients in the bulk solution have been calculated using Phreeqc.

Figure 5-5 shows that the result of the hybrid model depends on the choice of volume ratio between the bulk solution and the interlayer solution. When the amount of bulk water becomes large (approaching 100 %), the result of the hybrid model resembles that of the Phreeqc cation exchange model in the same limit (i.e. 100 % bulk water). In the other limit, however, with the amount of bulk water taking a small value, the hybrid model instead resembles the pure interlayer model. For intermediate values, the results of the hybrid model lie between these limiting values. Moreover, the Phreeqc cation exchange model is seen to resemble the hybrid model only in the limit of 100 % bulk water.

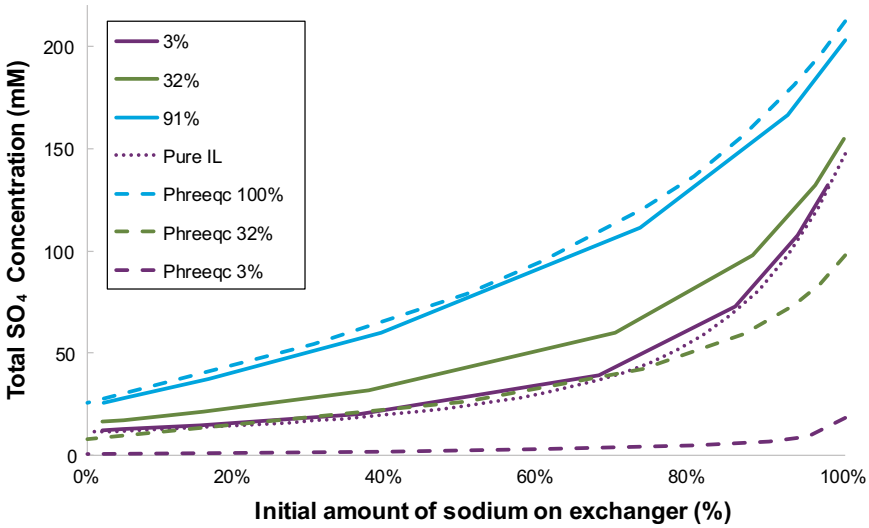

Figure 5-5. *Total sulfate concentration in the hybrid model as a consequence of anhydrite dissolution in pure Ca/Na-montmorillonite for three different choices of φ^{bulk} (corresponding to 3 %, 32 %, and 91 % of the total amount of water). Also displayed are the corresponding results for the pure interlayer model, as well as for the Phreeqc models with bulk porosity corresponding to 3 %, 32 %, and 100 %.*

It should be noticed, that although the total concentrations agree with the pure interlayer model in the limit of small φ^{bulk}, the actual concentrations in the bulk solution are very far from the values of the total concentrations. Figure 5-6 shows the corresponding bulk solution concentrations at the solubility limit for anhydrite in the hybrid model with $\varphi^{bulk} = 0.014$ (3 % bulk water). For a pure Ca bentonite (no initial sodium in the interlayer) the bulk solution corresponds to the ordinary solution obtained when dissolving anhydrite in pure water, while in the limit of a "pure" Na bentonite, the bulk solution ionic strength is as high as 0.6 M.

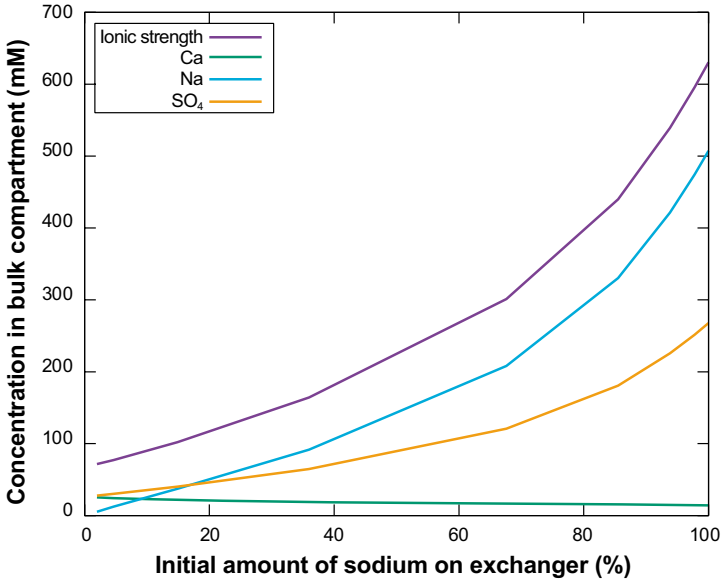

Figure 5-6. *Total concentrations of calcium, sodium, and sulfate in the bulk solution at the anhydrite solubility limit in the hybrid model for 3 % bulk water.*

5.2 Model for implementation testing

Here a model system is defined, in order to test the implementation of the hybrid model as well as compare it with other approaches. It is in essence an extension of the test system established in Section 5.1.

5.2.1 Case 2: Only transport

The model, presented schematically in Figure 5-7, is 1D, and consists of a single 5 mm long bentonite domain with a total porosity of $\varphi = 0.452$. In model case 2, the domain initially contains only pure Ca-montmorillonite. CEC is set to 0.9 eq/kg, and the interlayer and bulk pore diffusion coefficients are $D_c = D_p = 10^{-10}$ m^2/s.

The bentonite is contacted on the left side by a bulk solution reservoir of 0.17 M $NaSO_4$, which in the model is represented by a constant concentration boundary condition on this side (Figure 5-7). This condition implies an infinite reservoir volume (alternatively, it may be thought to represent a well flushed boundary). Additionally, the reservoir is spiked by a neutral tracer of constant concentration 0.1 M. The right-side boundary is closed.

Case 2 was set up both in the hybrid model and in a traditional Phreeqc model. The traditional Phreeqc model treats interlayers as exchange sorption sites and all transport (and chemistry) occurs within a bulk water phase. To make the two models as comparable as possible, the following model specific parameter choices were made. In both set-ups, the bulk water phase was chosen to be 32 % of the total porosity (i.e. $\varphi^{bulk} = 0.145$). This choice implies that the parameter c_{IL} in the hybrid model was set to $c_{IL} = 4.42$ M ($c_{IL} = (\varphi/\varphi^{int})\cdot CEC/w$). For the corresponding Phreeqc model, the choice of bulk water porosity implies an amount of exchange sites of 9.317 mol/(l bulk water) ($[X] = (\varphi/\varphi^{bulk})\cdot CEC/w$). Table 5-4 summarizes the data used for each model.

Table 5-4. Summary of the different models used to implement the verification test model. IL stands for interlayer.

Parameter	Hybrid model	Traditional (Phreeqc)	Pure IL model	Traditional + IL diffusion (Phreeqc)
Interlayer water (%)	68	As exchanger	100	Exchanger + transport capacity
Bulk water (%)	32	32	0	32
c_{IL} (mol/L)	4.41		3.0	
Exchange sites, X (mol/$L_{bulk\ water}$)	0	9.371	0	9.371

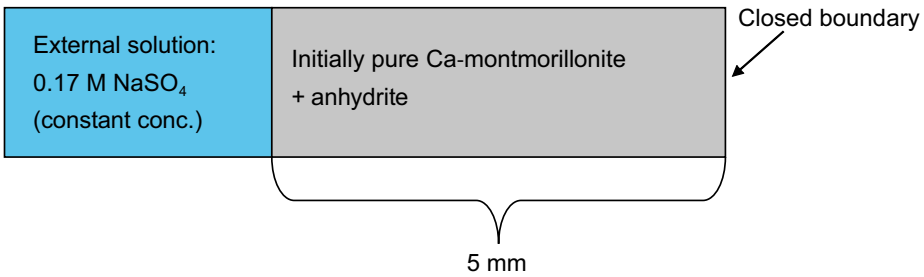

Figure 5-7. *Schematics of the verification case models. In model case 2 the bentonite component initially contains only pure Ca-montmorillonite and no anhydrite. In model case 3, the bentonite initially consists of pure Ca-montmorillonite and 1.4 wt% anhydrite.*

The implementation of the Donnan equilibrium in the Hybrid Model has been verified by calculating the Donnan factor externally with the bulk concentrations and activity coefficients obtained after 100 000 seconds. As can be seen in Figure 5-8, the Donnan factor calculated by iCP in the Hybrid Model is in good agreement with the external calculation.

Figure 5-9 shows a comparison between the results of Case 2 in the hybrid and the traditional Phreeqc model. In order to make the comparison as clear as possible, most of the results in this figure are plotted in terms of moles per total volume (L medium, including both water and solids). Tracer transport results show that concentrations of neutral species evolve slower in the hybrid model due to a buffering effect of the bulk water, see Section 2.4.2. From this figure, it is clear that charged species evolve differently in the two models. Due to the interlayer transport capacity of the hybrid model, ions have time to propagate considerably farther as compared to the traditional Phreeqc model. Note that this is not an effect of increased mobility (as demonstrated by the results for the neutral tracer) but of the fact that much less charge is immobilized in the hybrid model. In the Phreeqc model, all ions associated with the interlayer (i.e. the exchanger, in this model) are "sorbed", while all interlayer ions are mobile by definition in the hybrid model. In contrast, while all mass transfer occurs in the bulk phase in the Phreeqc model, the bulk water ions in the hybrid model are, in a sense, immobilized (see Section 2.4.2).

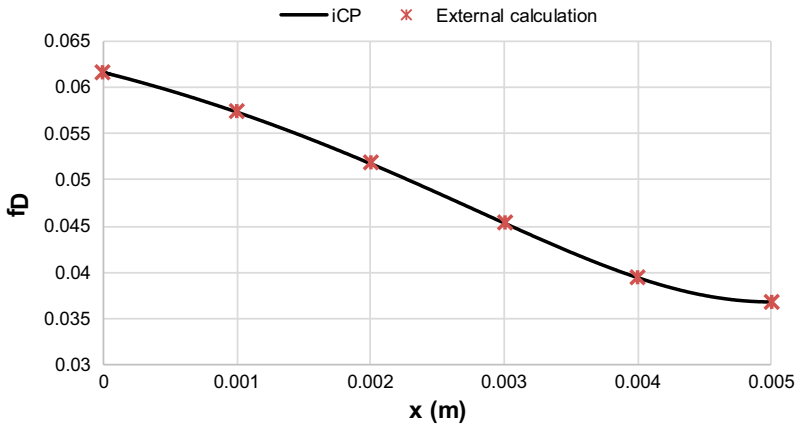

Figure 5-8. *Donnan factor obtained with the iCP hybrid models after 100.000 seconds (black line) compared to the Donnan factor calculated externally with Equation 2-21 and the bulk concentrations and activity coeffcients obtained with iCP (red crosses).*

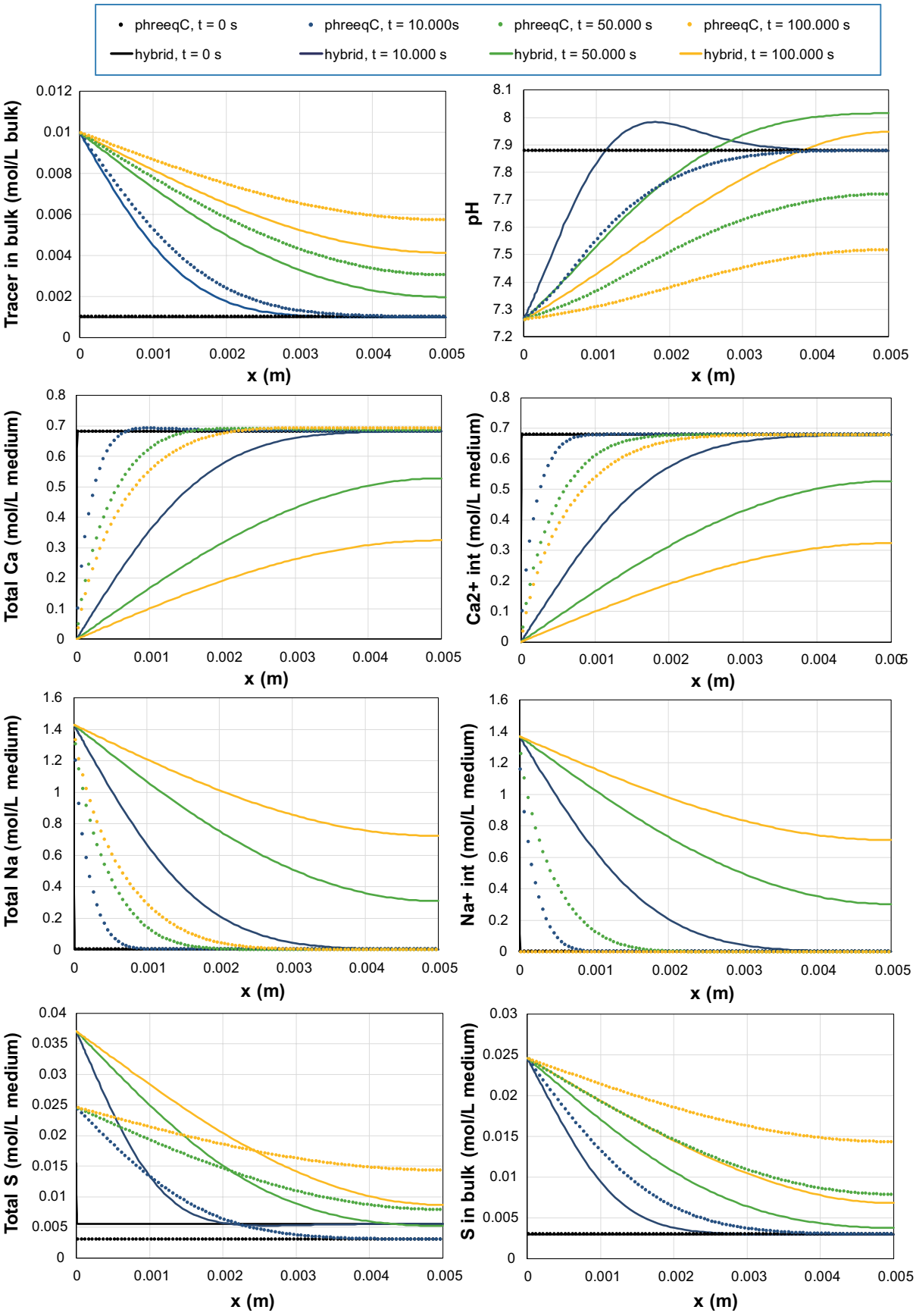

Figure 5-9. *Concentration profiles after 10 000 s, 50 000 s, and 100 000 s of Case 2 in the hybrid model and the traditional Phreeqc model.*

5.2.2 Case 3: Transport and dissolution

In a second modelling stage, 1.4 wt.% of anhydrite was added in the initial state of the bentonite under isothermal conditions. In this model, anhydrite will dissolve/precipitate due to Na in-diffusion and replacement of Ca in the exchanger/interlayer. In addition to the two modelling approaches adopted in the previous case (hybrid and traditional Phreeqc), this case was also simulated using two additional approaches. The first one is an interlayer-only approach (see Section 5.1.2), while a second one consists of a Phreeqc model which allows for interlayer diffusion (diffusion in the domain of "sorbed" cations) in addition to the diffusion in the bulk porosity. For the hybrid model and the traditional Phreeqc models, exactly the same parameter choices were made as for modelling case 1. This is also true for the Phreeqc model with interlayer transport simulation. It is noted that in the pure interlayer model mineral dissolution there is no bulk solution by definition. This implies that mineral reactions take place in the interlayer water. This model has as an additional parameter, the diffusion coefficient in the interlayer domain, which was varied in order to study the influence of allowing interlayer transport.

For the interlayer-only simulation, obviously no partition between bulk and interlayer water is made. In order to be consistent with the CEC value, the c_{IL} value for this model was chosen to be $c_{IL} = CEC/w$ = 0.9 eq/kg/0.3 = 3 eq/kg. Moreover, interlayer activity coefficients for the species under consideration were chosen as in Section 5.1.2.

Figure 5-10 shows a comparison of some key results between the different models. From this figure, it is evident that the evolution of anhydrite precipitation/dissolution occurs very differently in the hybrid model as compared to the traditional Phreeqc model. While the Phreeqc model predicts major precipitation at the interface to the bulk solution, the hybrid model predicts a dissolution front which has propagated considerably farther into the clay. Qualitatively similar dissolution fronts are also observed in the pure interlayer model and in the Phreeqc model with interlayer diffusion. It thus appears as if the inclusion of interlayer transport qualitatively changes the chemical evolution. This finding is explored further in Figure 5-11, which shows results of the Phreeqc multiporosity model for various choices of the interlayer diffusion coefficient. The larger the value of this parameter (relative to the bulk diffusion coefficient), the more pronounced becomes the anhydrite dissolution front.

5.3 Case 4: solute transport

Equation 2-48 was tested for a neutral tracer diffusion by performing simulations that consider only transport with different interlayer/bulk porosity partitions. These simulations were performed with the iCP hybrid model and with Comsol in order to verify the implementation of the hybrid model. Figure 5-12 shows the solutions at three different snapshots for the cases of having interlayer/bulk porosity partitioning of 50/50 and 68/32 respectively. The hybrid and Comsol models are seen to give identical results. Moreover, the 50/50 case is "delayed" in comparison to the 68/32 case, as predicted by Equation 2-47.

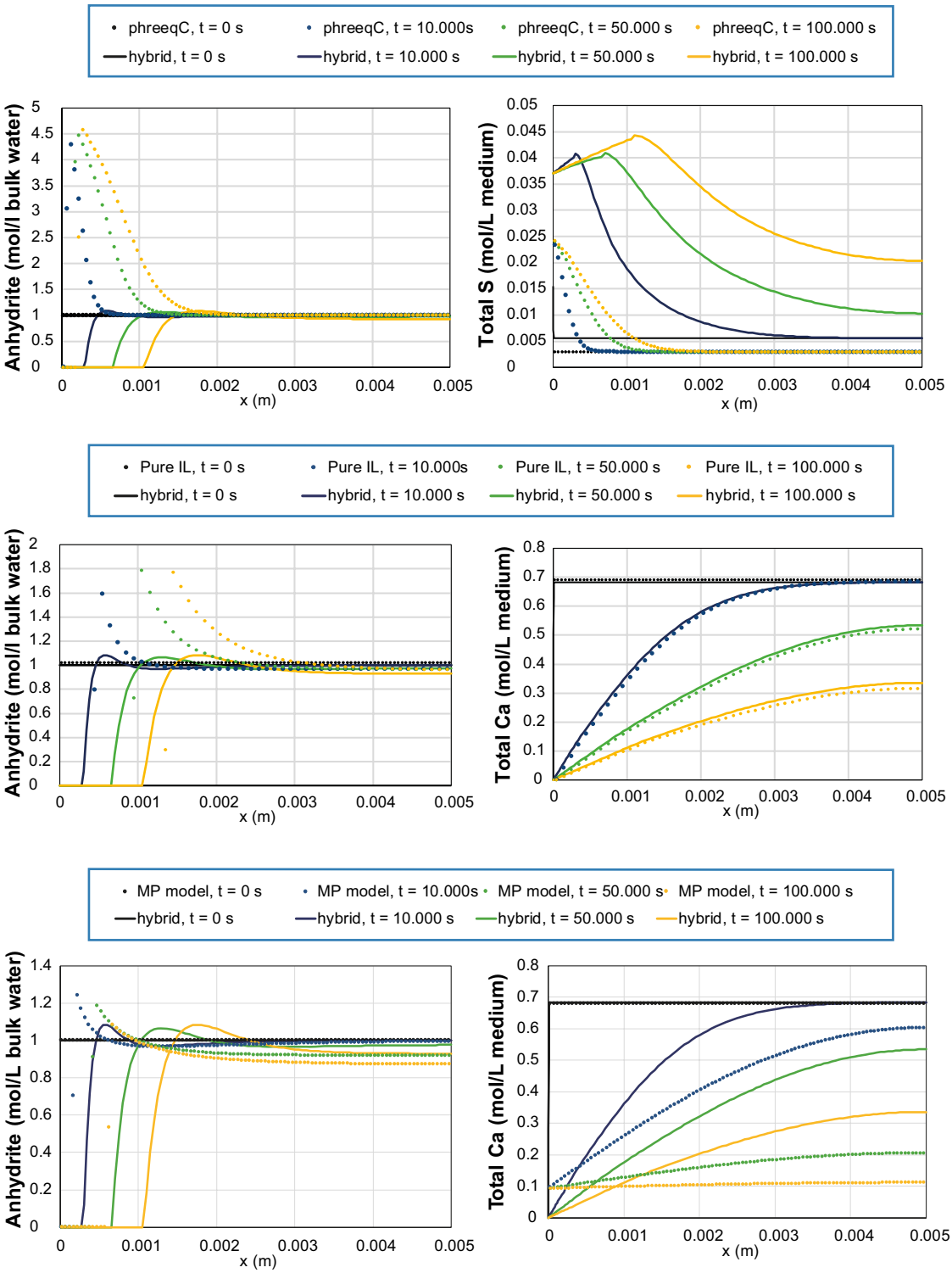

Figure 5-10. *Left: Comparison of evolution of anhydrite precipitation/dissolution in the hybrid model with traditional Phreeqc (top), interlayer only (mid), and the multiprosity model implemented in Phreeqc (bottom). Right: The evolution of total sulfur occur very differently in the traditional Phreeqc model (top). Evolution of calcium is similar in the hybrid model as compared to pure interlayer (mid) and multiporosity (bottom) models.*

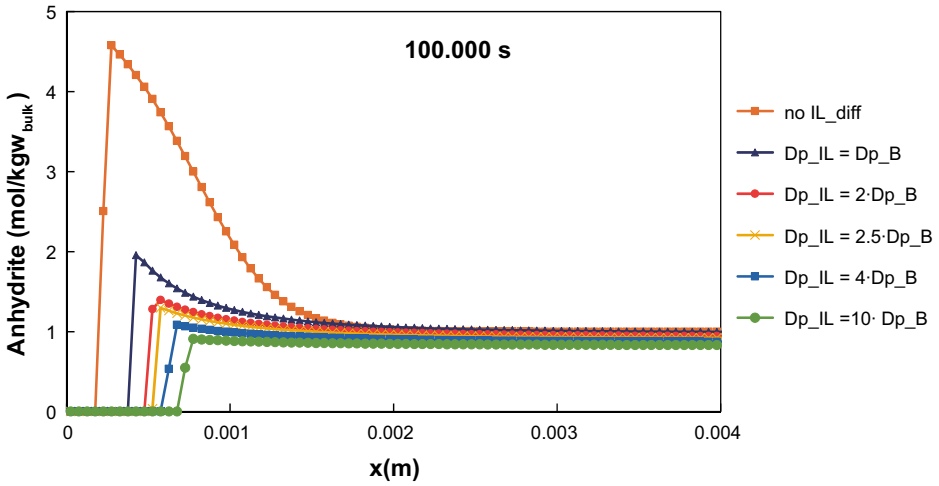

Figure 5-11. *Anhydrite preciptiation in Phreeqc model with included interlayer transport. The curves show anhydrite distribution after 100 000 s for various values of interlayer diffusion coefficient: 0, 1, 2, 2.5, 4, and 10 times the value of the bulk diffusion coefficient (10^{-10} m^2/s).*

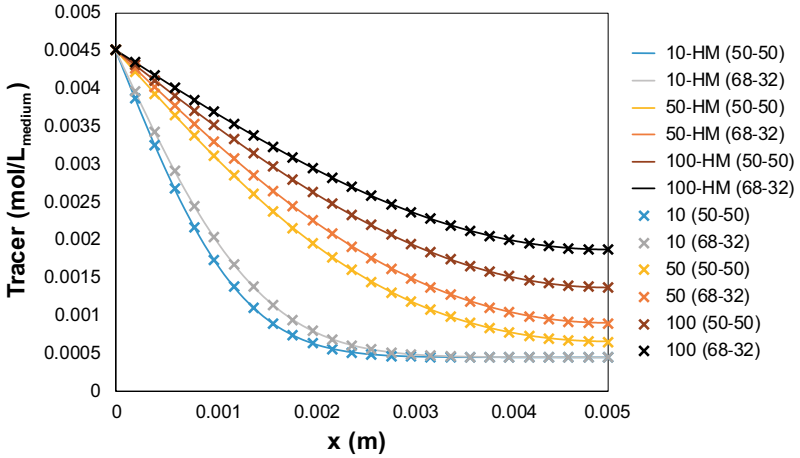

Figure 5-12. *Results for the infiltration of a neutral tracer in hybrid model (HM) for the two interlayer/ bulk porosity partitioning 50/50 and 68/32 at 10 000 s, 50 000 s, and 100 000 s. Also plotted are the corresponding models solved with Comsol.*

6 Modelling sulfide in the KBS-3V near-field

6.1 Background

The main goal of the Integrated Sulfide Project is the assessment of copper corrosion in the canister of a KBS-3V repository due to the presence of sulfide. To this end, conceptual and numerical models of the fate of sulfide in the near-field are needed to quantify the different processes concerning sulfide production, transport and consumption.

SKB and Posiva have defined, in collaboration with the different modelling teams involved in the project, a Base Case to model the main physical and chemical processes affecting sulfide fate in the near-field. In the following sections, the Base Case is presented and adapted to be implemented in two different reactive transport approaches and the results are presented. The results of the other two modelling teams can be found elsewhere (Pękala et al. 2019, King and Kolář 2019). The first approach considered in the present study consists of a traditional reactive transport model. In this approach, bentonite is modelled as a single bulk porosity system; interlayer pores are represented by cation exchange sorption sites, with zero volume (bulk porosity equals total or physical porosity). In the second approach, the hybrid model presented in sections 2 and 3 is used, which accounts for diffusion of species in the interlayer.

In Section 6.2, the Base Case is described in detail. Results of the simulation of the Base Case over 100 000 years using a traditional reactive transport model are presented and discussed in Section 6.3. Moreover, a simplified case is also presented with the aim of obtaining a simpler model that can be more easily compared to the hybrid model results. Section 6.4 presents the setup and results of the Base Case simulated using the hybrid model.

6.2 Description of the Base Case

The conceptual model is limited to the near-field of a KBS-3V repository, i.e. a square box of approx. 10 m around a deposition hole (Figure 6-1a). The copper canister is surrounded by an engineered barrier, the buffer, made of compacted MX-80 bentonite, which fills the deposition hole. The deposition tunnel is filled with backfill material, also composed of compacted bentonite, although with different properties. The host rock is treated as an Equivalent Continuous Porous Medium (ECPM), i.e. fractures reaching the deposition tunnel and/or the deposition hole (Figure 6-1b) are not explicitly considered as sources of inflowing water. Between the rock and engineered barriers interfaces are formed, which are referred to here as Rock-Tunnel Interface (RTI) and Rock-Deposition Hole-Interface (RDI). Figure 6-1b shows the different domains and their dimensions. No water flow is considered, and thus solute transport occurs exclusively by diffusion, as indicated by the schematic representation shown in Figure 6-2. Fully water saturated conditions, no remaining O_2, and isothermal system at 25 °C is considered to study the evolution of the sulfide concentrations in the repository near-field.

A full representation of the Base Case would require a 3D geometry, but a 1D simplification is considered here in order to achieve feasible calculation times, especially with the hybrid model. The geometry of the system considers a vertical profile (section A-A' in Figure 6-2) from the canister top lid (0.05 m) to the RTI (0.3 m), traversing the buffer (2.5 m) and backfill (4.4 m) domains. The bedrock is modelled as an additional domain with a length of 5 m.

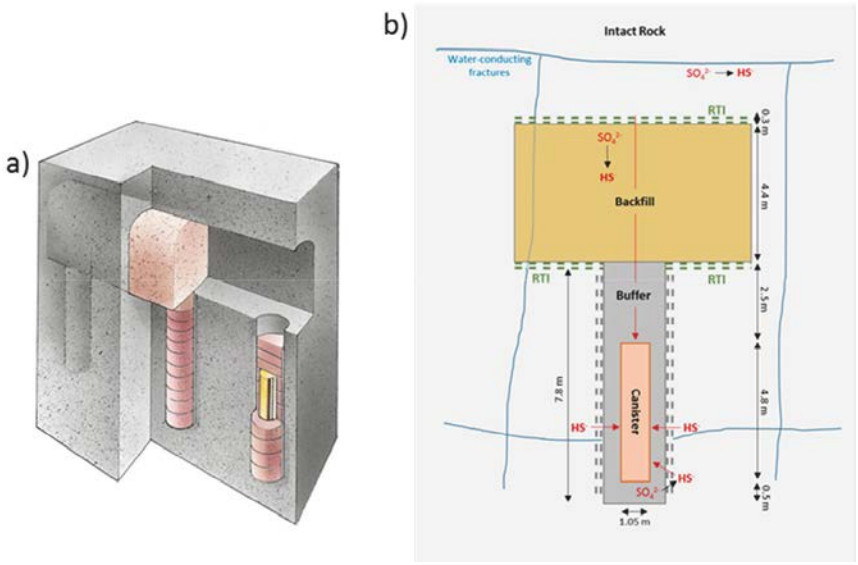

Figure 6-1. *a) The KBS-3 system with canisters deposited one by one in vertical holes. b) Dimensions of the near-field in a KBS-3 repository for OL1&2 canisters (from Wersin et al. 2014). Estimated sulfate/ sulfide fluxes in the near field are indicated in the same figure.*

It should be noted that this 1D representation excludes the impact of the RDI on canister corrosion and evaluates only the sulfide flux from the RTI towards the canister. Thus, the 1D model used in this work under-estimates canister corrosion significantly as the RDI is expected to generate higher sulfide fluxes than the RTI due to a much shorter distance to the canister and the presence of siderite in the backfill. This siderite is a source of iron that causes sulfide precipitation as mackinawite (FeS) along the RTI – canister diffusion path. It should be noted, however, that the duration of significant sulfide production is longer at the RTI due to the high availability of organic matter and sulfate. Moreover, the variant cases analysed here consider different hypotheses involving the backfill, which could not be tested using a radial model including the RDI. A 3D analysis of the entire system using a traditional reactive transport approach is presented and discussed in Pękala et al. (2019).

A general description of the Base Case chemistry is in Section 6.2.1, while a more detailed description and parametrization is given for each domain in sections 6.2.2 to 6.2.6.

6.2.1 General setup

Given that the main goal of the Base Case is to estimate the sulfide production rates and concentrations in the near field, no sulfate, sulfide or dissolved organic matter is considered in the groundwater from the rock (their concentrations are set to zero). The reason behind this simplification is to exclusively assess sulfide production and diffusion in the components of the engineered barrier system.

Sulfate is typically present as an accessory mineral (i.e. gypsum) of the buffer and especially the backfill. In the same way, the source of organic matter considered in the model is also in the buffer and backfill. The bentonite barriers represent the only pool of sulfate and organic matter in the model. Under specific conditions, sulfate can be reduced to sulfide. However, given the high dry density of the barriers, it is expected that bacterial activity is minimal or even absent. Therefore, the Base Case assumes that sulfate will not be reduced in the engineered barriers, but only in the RTI and RDI. Pyrite (iron sulfide) may be present in the backfill and buffer materials, but it is very insoluble under anoxic conditions and is not considered in the Base Case. Mackinawite precipitation is the only process potentially able to control sulfide concentrations in the Base Case.

The interplay between the above-mentioned processes will ultimately determine the amount of sulfide reaching the canister. The main components of the different domains are shown in Figure 6-2.

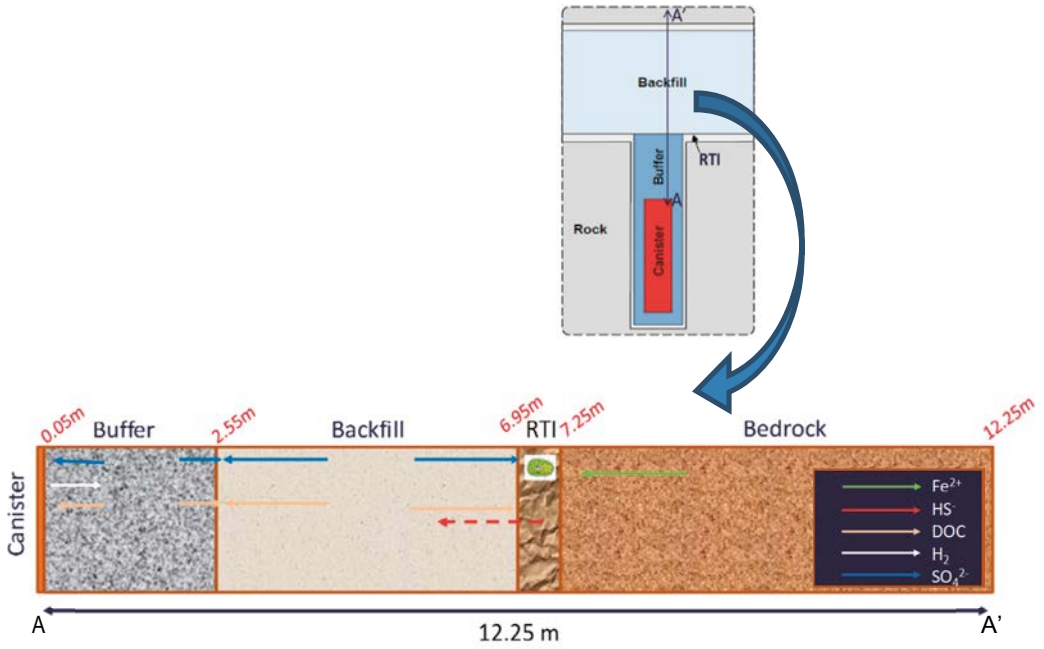

Figure 6-2. *Schematic representation of a vertical profile (A-A') from the canister top lid to the rock, showing the sulfate/sulfide pathways along the five domains considered in the Base Case model.*

In the Base Case, bacterial activity is only allowed in the RTI and RDI. In these regions, sulfide can be produced by microbially-mediated sulfate reduction. These chemical reactions require a source of carbon and energy for bacteria activity. Two different pathways for sulfate reduction are considered, depending on the available electron donor. In the first case, a reaction induced by the presence of CH_2O is considered (Equation 6-1). The second pathway refers to the sulfate reduction induced by the presence of dissolved H_2. The main source of aqueous CH_2O in the RTI is the dissolved organic matter (DOM) that diffuses from the buffer and the backfill towards the RTI and acts as an electron donor according to Equation 6-1 (Figure 6-2).

$$2CH_2O + 4H_2O \rightarrow 2HCO_3^- + 10H^+ + 8e^- \quad (6\text{-}1)$$

Sulfate is the electron acceptor and it is reduced to sulfide (HS^-) according to:

$$SO_4^{2-} + 9H^+ + 8e^- \rightarrow HS^- + 4H_2O \quad (6\text{-}2)$$

If sulfide reaches the canister, H_2 is expected to be generated as a sub-product of the corrosion process (Figure 6-2) according to:

$$2Cu + HS^- + H_2O \rightarrow Cu_2S + H_2 + OH^- \quad (6\text{-}3)$$

If dissolved hydrogen reaches the RTI, it is available for bacteria and a second sulfate reduction process will be activated:

$$4H_2 + SO_4^{2-} + H^+ \rightarrow HS^- + 4H_2O \quad (6\text{-}4)$$

Reactions given in Equations 6-2 and 6-4 produce aqueous sulfide. In the Base Case, mackinawite precipitation (FeS in the reaction below) is the only process potentially able to control sulfide concentrations in the system (Equation 6-5).

$$Fe^{2+} + HS^- \rightarrow H^+ + FeS \quad (6\text{-}5)$$

The interplay of this chemical reaction sequence will determine HS^- concentrations in the whole system and, as a consequence, the canister corrosion depth.

The corrosion depth (d, in meters) is calculated from the moles of Cu consumed in the reaction 6-3 as follows:

$$d = Cu \cdot V_m \cdot \frac{1}{A} \quad (6\text{-}6)$$

In this equation, Cu denotes the mass of copper consumed (mol), V_m is the molar volume of copper ($7.087 \cdot 10^{-6}$ m^3_{Cu}/mol) and A ($m^2_{mineral}$) is the surface area of the copper canister (1 m^2 in the present work). All chemical reactions in the model are considered under thermodynamic equilibrium and solved using the ThermoChimie thermodynamic database v9b (Giffaut et al. 2014). The only exceptions are the Monod kinetics (Jin et al. 2013) implemented in the RTI to simulate the reduction of sulfate to sulfide in the RTI domain (see Equations 6-7 and 6-8 below). Redox states for S and H_2 are considered decoupled in the database, so no redox equilibrium is considered for these two systems.

A summary of the geochemical processes and parameters of each domain is given in Appendix B. The Base Case stipulates that production of sulfide only occurs in the RTI and RDI domains. As shown below, the rate-limiting factor for sulfide production is transport of reductants (CH_2O and H_2) towards the RTI, since the kinetic rates of sulfide production are much faster than the diffusion rates. At the same time, the effective diffusion coefficient in the RTI/RDI is more than 2 orders of magnitude lower than that of the bentonite barriers. Sulfide reaching the canister surface is consumed in the corrosion reaction assuming an instantaneous reaction (Equation 6-3).

6.2.2 Intact rock

The bedrock domain is included as an Equivalent Continuous Porous Medium (ECPM) representation of the rock matrix and fractures, with a porosity corresponding to fractured rock (Table 6-1). Diffusive transport is assumed between the intact rock and the RTI/RDI and zero groundwater flow is considered. Diffusion coefficients are shown in Table 6-1 (Posiva 2013). The sulfate-rich brackish water defined in Hellä et al. (2014) is the reference groundwater prescribed for this domain (Table 6-2). However, as reasoned above, sulfate and sulfide concentrations were initially set to zero. Constant boundary properties (fixed groundwater concentrations) were imposed at a distance of 5 m from the RTI. Calcite and mackinawite are the only minerals allowed to precipitate as secondary minerals.

Table 6-1. Physical parameters of the host rock (Posiva 2013).

Parameter	Value	Observations
Total porosity (ϕ)	0.00515	Rock represented as ECPM (matrix and fractures) From rock matrix porosity and a kinematic porosity of 0.15 % on p.22, Table 2-5 and p.57, Table 4-2 of Hartley et al. (2013).
Diffusion accessible porosity (Rock matrix porosity)	0.005	Groundwater flow modelling in Hartley et al. (2013) referred to in Posiva (2013, Section 6.1 (p.169) and Section 7.8, Table 7-13 (p.578))
Molecular diffusion coefficient in water (D_w)	$1.0 \cdot 10^{-9}$ m^2/s	Posiva (2013, Table I-1, p.733)
Effective diffusion coefficient (D_e) for intact rock matrix	$6 \cdot 10^{-14}$ m^2/s	Posiva (2013, Table I-1, p.733)
Effective diffusion coefficient (D_e) for fractured rock	$2 \cdot 10^{-13}$ m^2/s	Estimated in this project to provide diffusion in a ECPM representation of the rock

6.2.3 Rock-Tunnel Interface (RTI)

The rock-tunnel interface is represented as an ECPM, with a porosity of about 4 times the value for intact rock (Figure 6-1, Table 6-3). Groundwater composition and minerals in equilibrium in the RTI are the same than those for the intact rock (Hellä et al. 2014, Table 6-2). However, as the porosity in the RTI is higher than in the intact rock, the effective diffusion coefficient is higher and equal to $5 \cdot 10^{-13}$ m^2/s (Table 6-3).

As mentioned above, Sulfate Reducing Bacteria (SRB) activity is restricted to the RTI/RDI. A constant concentration of biomass [X] of $3.54 \cdot 10^{-5}$ mol/L_{H2O} ($3.54 \cdot 10^{-4}$ mol/$m^3{}_{medium}$) is assumed. This value is calculated from the total number of cells of SRB by assuming an average cell dry mass of 5×10^{-13} g/cell and an average formula of $C_5H_7O_2N$ with a molar mass of 113.115 g/mol. In the Base Case, [X] corresponds to the attached cells in the fracture surfaces as well as suspended in groundwater. No minerals are included in the RTI as an initial condition. The only secondary minerals allowed to precipitate are calcite and mackinawite.

Table 6-2. Chemical composition of references waters for the different domains (from Hellä et al. 2014, Table 6-3). Concentrations in mg/L unless otherwise stated.

	From Brackish water			From Brackish water			From sulfate-rich brackish water	
BUFFER	Sample	OLKR6_135_8	BACKFILL	Sample	OLKR6_135_8	INTACT ROCK and RTI	Sample	OLKR6_135_8
	log p(CO_2)	−2.7		log p(CO_2)	−2.7		Depth (z, m)	−101
	pH	7.23		pH	7.21		pH	7.6
	Eh (mV)	−207		Eh (mV)	−201		Eh (mV)	−240
	Alk. (eq/L)	$7.5 \cdot 10^{-4}$		Alk. (meq/L)	0.73		Alk. (HCO_3)	111
	Ionic strength (eq/L)	0.2712		Ionic strength (eq/L)	0.2451		TDS (g/l)	7.2
	Na	150.8		Na	110.24		Na	1760
	K	0.9		K	0.67		K	19
	Mg	144.4		Mg	16.04		Mg	180
	Ca	30.7		Ca	35.35		Ca	650
	Cl	222.3		Cl	176.01		Cl	4010
	S(VI)	9.4		S(VI)	18.5		S(VI)	460
	S(-II)	0.0012		S(-II)	0.0006		S(-II)	0.02
	CO_{3tot}	0.9		CO_{3tot}	0.865		DIC	22.3
	Sr	0.2		Sr	0.167		Sr	8.1
	Si	0.17		Si	0.173		SiO_2	11
	Mn	0.041		Mn	0.033		Mn	1.2
	Fe	0.011		Fe	0.018		Fe	0.32
	F	0.032		F	0.025		F	0.3
	Br	0.33		Br	0.265		Br	13.2
	B	0.11		B	0.089		B	0.62
	NH_4	-		NH_4	-		NH_4	0.33
	PO_4	-		PO_4	-		PO_4	0.03
	Table E-2 (Posiva 2013)			Table F-2 (Posiva 2013)			Table 6-3 (Hellä et al. 2014)	

Table 6-3. Physical properties of the rock-tunnel interface (RTI) and rock-deposition hole interface (RDI). Data from Posiva (2013) and Hartley et al. (2013).

Rock-tunnel interface (RTI). Underground openings data (Posiva 2013)		
Parameter	**Value**	**Source**
Thickness, except below tunnel floor	0.3 m	Agreed in this project
Thickness below tunnel floor	0.4 m	Section 5.1.5, p.80 and Table E-1, p.234 in Hartley et al. (2013)
Porosity	0.01	Table E-1, p.234 in Hartley et al. (2013)
Effective diffusion coefficient (D_e)	$5 \cdot 10^{-13}$ m^2/s	Estimated as $D_e = D_w F_f$, with $F_f = 0.71\ \theta^{1.58}$ (Figure 3-5 in Byegård et al. 2008, p.45), and $\theta = 0.01$
Rock-Deposition hole interface (RDI)		
Parameter	**Value**	**Source**
Thickness of affected area	0.1 m	p.74, and Table E-1, p.234 in Hartley et al. (2013)
Porosity of affected area	0.02	Table E-1, p.234 in Hartley et al. (2013)
Effective diffusion coefficient (D_e)	$1.5 \cdot 10^{-12} m^2/s$	Estimated as $D_e = D_w F_f$, with $F_f = 0.71\ \theta^{1.58}$ (Figure 3-5 in Byegård et al. 2008, p.45), and $\theta = 0.02$

Sulfate reduction to sulfide is assumed to occur *via* two different processes, i.e. using either CH_2O or H_2 as electron donor. These reactions were implemented as Monod kinetics rate expressions, as follows:

$$\frac{d[SO_4^{2-}]}{dt} = -\frac{d[HS^-]}{dt} = -[X] \cdot k_{max} \cdot \frac{[H_2]}{K_{H_2}+[H_2]} \frac{[SO_4^{2-}]}{K_{SO_4^{2-}}+[SO_4^{2-}]} \quad (6\text{-}7)$$

$$\frac{d[SO_4^{2-}]}{dt} = -\frac{d[HS^-]}{dt} = -[X] \cdot k_{max} \cdot \frac{[CH_2O]}{K_{CH_2O}+[CH_2O]} \frac{[SO_4^{2-}]}{K_{SO_4^{2-}}+[SO_4^{2-}]} \quad (6\text{-}8)$$

where the k_{max} value for the H_2–mediated reaction is $6.4 \cdot 10^{-5}$ s^{-1} (Maia et al. 2016) and the k_{max} value for the CH_2O–mediated reaction is $1.5 \cdot 10^{-4}$ s^{-1} (Jin et al. 2013). The values of the half-saturation constants K_{H_2}, K_{CH_2O} and $K_{SO_4^{2-}}$ are $4.0 \cdot 10^{-6}$ M (Maia et al. 2016), $5.0 \cdot 10^{-6}$ M (Jin et al. 2013) and $1 \cdot 10^{-5}$ M (Nethe-Jaenchen and Thauer 1984), respectively.

Initially, there are no reductants (CH_2O, H_2) in the RTI/RDI. Sulfate and organic matter are supplied from the backfill and buffer. In turn, dissolved H_2 is a product of the sulfide-induced corrosion of the canister, which can diffuse through the bentonite barriers towards the RTI. Mackinawite precipitation is allowed in the entire model domain as a secondary mineral (except in the canister).

6.2.4 Backfill

The composition of the reference porewater, derived from brackish water (Table 6-2), is taken from Posiva (2013). The main material properties for the backfill are included in Table 6-4 and its mineralogical composition in Table 6-5. The only reactive minerals included in the simulations are calcite, gypsum, organic matter and siderite. Mackinawite is not initially present in the backfill, but is allowed to precipitate. Cation exchange with a constant cation exchange capacity (CEC) is implemented in the model, based on the mass fraction of montmorillonite. No montmorillonite dissolution is considered. Selectivity coefficients for Na^+, Ca^{2+}, Mg^{2+} and K^+ are adopted from Bradbury and Baeyens (2002). Fe^{2+} exchange was also considered, assuming a selectivity coefficient for $Na^+ – Fe^{2+}$ of K = 2.51 (Charlet and Tournassat 2005). The potential impact of iron contained in the montmorillonite layer structure in the form of Fe(II/III) on redox reactions is not considered in the model.

It is assumed that 0.1 wt.% of the solid organic matter (SOM) concentration is prone to degradation and subsequently available as dissolved CH_2O (i.e. 10 % of 1 wt.% of the backfill in weight). An aqueous concentration of 2 mg/l (mg of C) is assumed for CH_2O in equilibrium with the SOM. This is implemented as a chemical reaction in thermodynamic equilibrium between the DOM and the SOM, with an equilibrium constant fitted to maintain the assumed aqueous concentration until all dissolvable SOM is exhausted.

Table 6-4. Physical properties of the backfill (data from Hellä et al. 2014 and Posiva 2013). Effective diffusion coefficients and porosity values agreed upon by the members of the project.

Parameter	Value
Pore diffusivity D_p (m^2/s)	$5.00 \cdot 10^{-11}$
ϕ(physical bulk porosity)	0.43
Effective diffusivity D_e (m^2/s)	$2.15 \cdot 10^{-11}$
Dry density (kg/m^3)	1720
CEC (eq/L)	2.12

Table 6-5. Mineralogical composition of the buffer (Hellä et al. 2014, Table 7-5) and backfill (Hellä et al. 2014, Table 7-11). Solid organic carbon assumed in this work.

Minerals	Composition (wt.%)		Composition (mol/kg_{water})	
	Buffer	Backfill	Buffer	Backfill
Calcite	1.40	2.20	0.51	0.88
Gypsum	0.40	1.90	0.08	0.44
Siderite	0.50	1.10	0.16	0.38
Montmorillonite	75.00	48.60	4.99	3.54
Kaolinite	0	6.20	0	0.96
Illite	0	15.40	0	1.58
Mica	0	4.30	0	0.43
Quartz	15.20	16.10	9.24	10.72
Feldspar	8.00	1.10	1.05	0.16
Dolomite	0	0.30	0	0.07
Pyrite	0.30	0.80	0.09	0.27
Tridymite	0	0.90	0	0.60
Goethite	0	0.30	0	0.14
Hematite	0	0.20	0	0.05
Magnetite	0	0.30	0	0.05
Anatase	0	0.20	0	0.10
Organic Carbon	0.10	0.10	0.30	0.33

6.2.5 Buffer

The buffer is composed of compacted MX-80 bentonite. The initial porewater composition for the buffer corresponds to the one derived from brackish water (OLKR6_135_8), as given in Table 6-2. The main physical properties of the buffer are included in Table 6-6 and its mineralogical composition in Table 6-5. The only reactive minerals initially present in the buffer included in the model are calcite, gypsum, and solid organic matter. Mackinawite and siderite are not initially present but are allowed to precipitate. No montmorillonite dissolution is considered. Instead cation exchange with a constant cation exchange capacity (CEC) is implemented in the model, based on the mass fraction of montmorillonite and using the selectivity coefficients from Bradbury and Baeyens (2002), and Charlet and Tournassat (2005) for Fe^{+2}. Siderite is not considered to be initially present in the buffer. The reason for this assumption is to be consistent with the input porewater in Table 6-2, which is not in equilibrium with siderite.

Calcite and gypsum are assumed to dissolve/precipitate under equilibrium conditions, while mackinawite and siderite precipitation is allowed as secondary phases (initial concentration set to zero). A fixed CH_2O concentration is assumed, i.e. 2 mg/L (mg of C), following the same constraints as for the backfill.

Table 6-6. Physical properties of the buffer (from Hellä et al. 2014 and Posiva 2013). Effective diffusion coefficients and porosity values agreed upon by the members of the project. The temperature is 25 °C.

Parameter	Value
Pore diffusivity D_p (m^2/s)	$5.00 \cdot 10^{-11}$
ϕ(physical bulk porosity)	0.43
Effective diffusivity D_e (m^2/s)	$2.15 \cdot 10^{-11}$
Dry density (kg/m^3)	1570
CEC (eq/L)	2.873
Grain density (kg/m^3)	2760

6.2.6 Canister

In this work, the interaction between the buffer porewater and the canister is considered using a porous medium representation of the canister domain with a thickness of 0.05 m and a pore diffusivity that is higher than that of the buffer. Canister corrosion is represented by a chemical process where HS^- is consumed to produce Cu_2S and H_2 according to the stoichiometry of reaction 6-3. Strictly speaking, this reaction should be limited by the solubility of Cu_2S ($\sim 10^{-14}$ M of sulfide under these conditions) but in the model presented here the canister domain acts as a perfect sulfide sink, producing H_2 at the same time. The H_2 produced is considered in the model to be decoupled from aqueous chemistry and can only react with SRB in the RTI to produce sulfide. The initial porewater in the canister has the same composition as that considered for the buffer (Table 6-2). No mineral reactions are considered in this domain. Transport properties are set arbitrarily high with a porosity of 0.5 and D_e value of $2.5 \cdot 10^{-10}$ m^2/s, so that the porous medium representation of the canister does not limit solute transport.

6.3 Traditional reactive transport model

6.3.1 Implementation of the model

The Base Case described above and summarized in Table 6-7 has first been implemented in the reactive transport code iCP (Nardi et al. 2014) using a traditional model. This model is considered traditional in the sense that bentonite is treated as a single bulk porosity system, while the interlayer is only considered *via* cation exchange reactions. The 12.25 m long model domain comprising (from left to right) the canister, buffer, backfill, RTI, and rock is discretized with cell sizes ranging from 10^{-5} m at the backfill-RTI interface to 0.05 m in the buffer and backfill domains (see Appendix C for details about the finite element mesh). Preliminary test cases showed that mesh refinement was needed at the RTI – backfill interface to ensure mass conservation, due to the sharp contrast in porosities at this interface (0.43 in the backfill and 0.01 in the RTI) and especially due to the kinetics of sulfide production at the interface.

The time span of the Base Case simulation is 100 000 years. The time step size for communication between the transport step and the chemical step is constant and equal to 1 year throughout the simulation. Within each time step, Comsol subdivides it to solve the diffusion of solutes, while Phreeqc also subdivides it to solve the kinetics in the RTI domain.

Boundary conditions for transport are no flux (i.e. closed boundary) at the left of the canister domain and at the rock right boundary. It is noted that preliminary simulations (not presented in this report) led to the conclusion that the contribution of the rock to the total sulfide mass balance was negligible even in the case that considers a fixed concentration of sulfide in the rock boundary (equal to 0 M). In consequence, most of the simulations presented in this work do not consider the rock domain at all.

6.3.2 Results of the Base Case

The evolution of the variables directly involved in the production of aqueous sulfide are presented in Figure 6-3. Sulfate concentrations remain virtually constant in all the modelled domains over time (Figure 6-3a). This is due to the large mass of gypsum available in the bentonite backfill. After 100 kyr, gypsum is still present in the entire backfill, with only partial dissolution near the RTI (Figure 6-4). The presence of gypsum thus controls the aqueous concentration of sulfate.

The consumption of organic matter within the RTI due to SRB activity follows the stoichiometry given by Equations 6-1 and 6-2. Two moles of organic matter (electron donor) are consumed per mole of sulfate (electron acceptor) consumed in the reactions. Moreover, the aqueous concentration of DOM in the backfill is much lower than the concentration of sulfate. Thus, the limiting factor for the reduction of sulfate is the availability of organic matter. This is observed in Figure 6-3, where the concentration of DOM suddenly drops to 0 at the RTI (Figure 6-3b), while sulfate concentration is hardly affected (Figure 6-3a).

Aqueous sulfide is produced by microbially-induced sulfate reduction in the RTI following the two paths described by the Monod reactions in Equations 6-7 and 6-8 (Figure 6-3c). That is, first as a result of the diffusion of sulfate and DOM from the barriers towards the RTI and later also from the diffusion of H_2 produced at the canister.

Table 6-7. Geochemical composition of each model domain in the full Base Case: minerals, porewater and exchanger. Na concentration is used for charge balancing the solutions.

Domain	Canister	Buffer	Backfill	RTI	Rock
Pore solution					
pH	7.2	7.2	7.2	7.1	7.1
pe	−3.4	−3.4	−3.4	−3.3	−3.3
Total concentrations (M)					
C	8.94E−04	8.94E−04	8.74E−04	1.73E−03	1.73E−03
Ca	4.04E−02	4.04E−02	3.58E−02	1.62E−02	1.62E−02
Cl	2.22E−01	2.22E−01	1.76E−01	1.13E−01	1.13E−01
DOM	1.67E−04	1.67E−04	1.67E−04	0	0
Fe	1.11E−05	1.11E−05	1.82E−04	5.70E−06	5.70E−06
Na	1.51E−01	1.51E−01	1.11E−01	6.69E−02	6.69E−02
S(-II)	1.20E−06	1.20E−06	6.00E−07	0	0
S(VI)	1.96E−02	1.96E−02	1.95E−02	0	0
K	9.00E−04	9.00E−04	6.74E−04	4.70E−04	4.70E−04
Mg	1.44E−02	1.44E−02	1.62E−02	7.45E−03	7.45E−03
Si	1.70E−04	1.70E−04	1.73E−04	1.80E−04	1.80E−04
Cation exchange (mol/kg_{water})					
NaX	-	9.84E−01	5.84E−01	-	-
CaX_2	-	7.34E−01	5.61E−01	-	-
MgX_2	-	1.98E−01	1.97E−01	-	-
KX	-	2.50E−02	1.49E−02	-	-
FeX_2	-	2.04E−04	2.91E−03	-	-
Mineral phases (mol/kg_{water})					
Calcite	-	5.10E−01	8.79E−01	0	0
Gypsum	-	8.48E−02	4.41E−01	-	-
SOM	-	3.04E−01	3.33E−01	-	-
Siderite	-	0	3.80E−01	-	-
Mackinawite	-	0	0	0	0

As it is produced, sulfide either diffuses across the bentonite barriers towards the canister (where it is consumed by the corrosion of copper according to reaction 6-3), migrates into host rock (Figure 6-3c), or precipitates as mackinawite (Figure 6-4a). The sulfide concentration near the RTI is observed to continuously increase during 100 kyr. This is a result of the continuous biotic sulfate reduction in the RTI domain. It is noted that mackinawite precipitation in this region controls the aqueous sulfide concentration. However, the release of H^+ from the sulfate reduction (Equations 6-1 and 6-2) and from mackinawite precipitation (Equation 6-5) leads to a gradual decrease in the pH of the backfill porewater (Figure 6-5). As a result, the solubility of mackinawite changes and higher sulfide concentrations are needed to maintain equilibrium.

The corrosion of copper leads to the generation of H_2, which diffuses towards the RTI (Figure 6-3d). Its concentration is maximal at the canister and continuously increases with time. After 100 kyr, it reaches a value of 0.8 μM, much lower than the solubility of H_2 at 5 MPa and 25 ºC (~0.0385 M). Therefore, no gas phase is expected to form in these conditions. When H_2 reaches the RTI, a second sulfate reduction reaction (Equation 6-4) is triggered, contributing to sulfide production. This second sulfate reduction process has a much lower impact on sulfide concentrations than the first one, which is to be expected given the small H_2 concentrations.

Iron concentration rapidly equilibrates due to diffusive transport and chemical buffering of iron minerals (siderite and mackinawite) and iron in the exchanger (see Figure 6-3e and Figure 6-6c). Thereafter, it remains with minor changes over time. As Fe^{2+} is being predominantly governed by the presence of iron minerals, its behaviour is analysed simultaneously with the evolution of these phases (Figure 6-4).

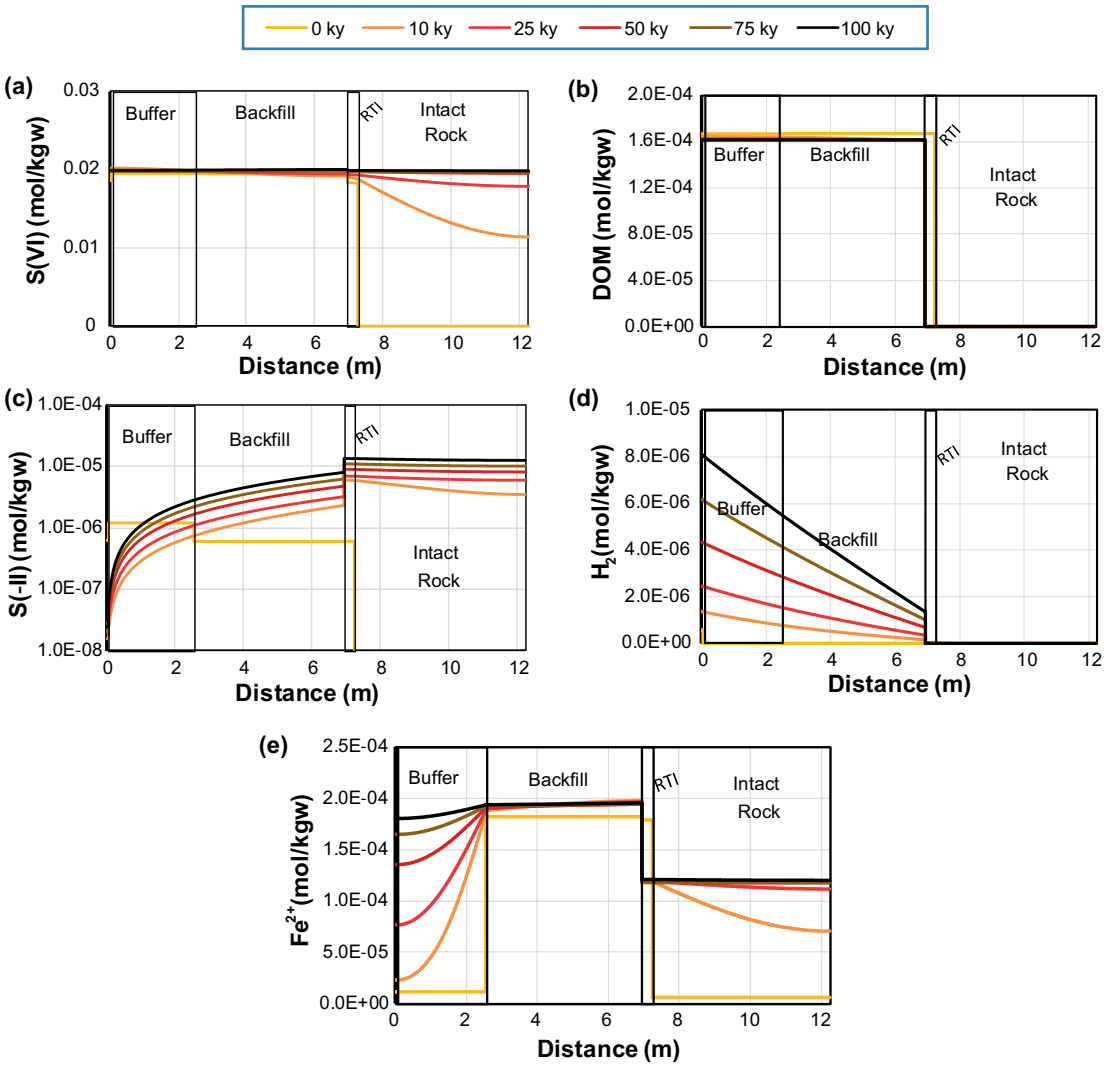

Figure 6-3. *Longitudinal profiles of aqueous concentrations (mol/kg$_{water}$) of (a) total sulfate, (b) dissolved organic matter (DOM), (c) total sulfide, (d) dissolved H_2, and (e) total Fe^{2+} for different times in the modelled system.*

As a consequence of sulfide production, mackinawite precipitates within the RTI and also at the interface between backfill and RTI due to the high availability of sulfide and Fe^{2+} (Figure 6-4a). Fe^{2+} is supplied by diffusion from the backfill towards the RTI, triggering partial dissolution of siderite (Figure 6-4c). Mackinawite formation is a key process that has two major effects:

1. To act as the main sulfide sink (see Equation 6-5)
2. To limit the sulfide concentration by its solubility control on HS^-.

The first effect is a very important sulfide buffer, acting as a sink for more than 90 % of the sulfide produced at the RTI. The second effect limits the concentration gradient that drives diffusion of sulfide from the RTI towards the canister.

Figure 6-4 (b to d) also shows that the sources of sulfate, organic matter, and iron, represented by gypsum, SOM, and siderite, respectively, are far from being exhausted. This means that the same governing processes described above will control sulfide production and consumption for a much longer period than the simulated time of 100 kyr.

The evolution of pH in the model domain over a period of 100 kyr is shown in Figure 6-5. The reduction of sulfate to sulfide in the RTI by means of the organic matter path causes a decrease of pH in the whole system that is still present after 100 kyr. Very small changes in the cation exchange composition are observed over the whole simulated period (Figure 6-6).

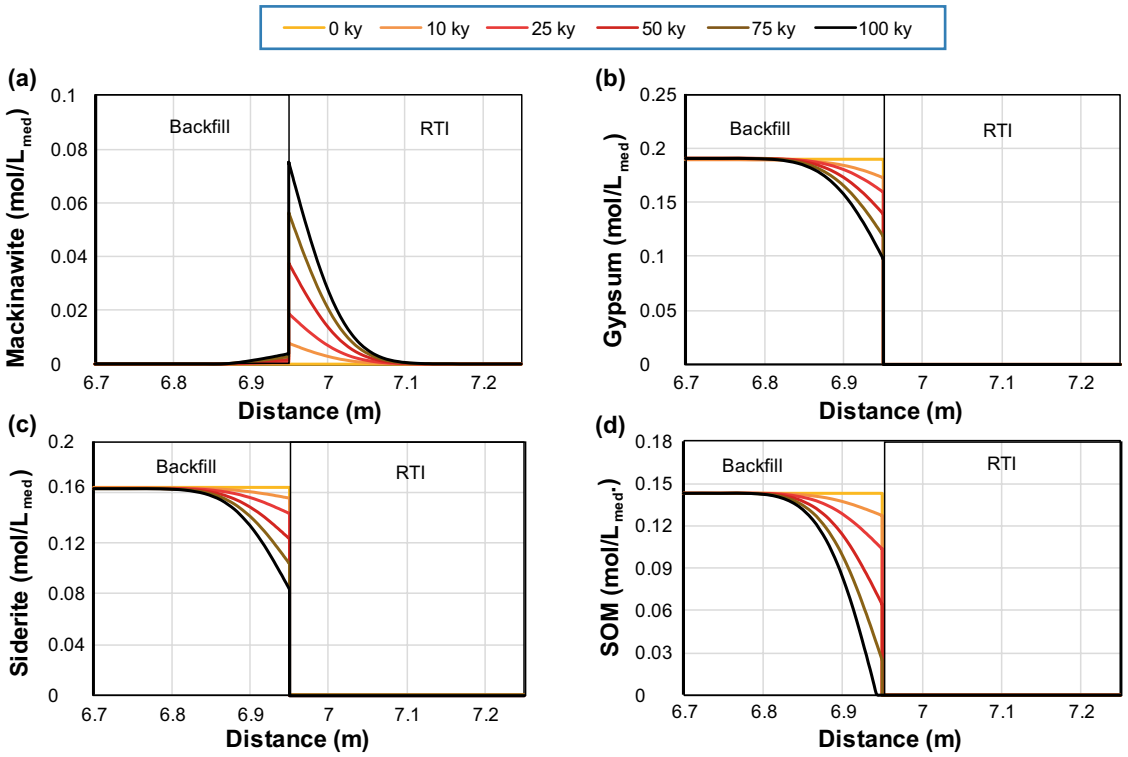

Figure 6-4. *Longitudinal profiles of mineral phases near the interface between backfill and RTI for different times: (a) mackinawite, (b) gypsum, (c) siderite, and (d) solid organic matter (SOM).*

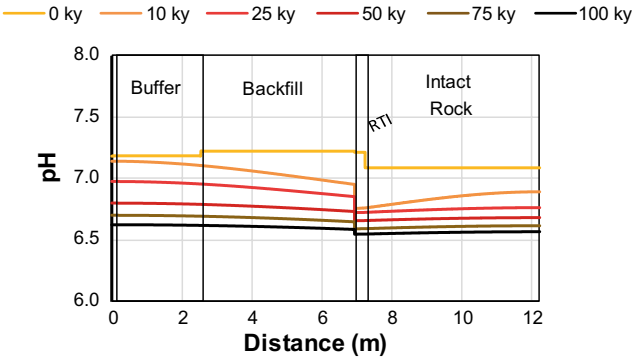

Figure 6-5. *Longitudinal profiles of pH for different times in the modelled system.*

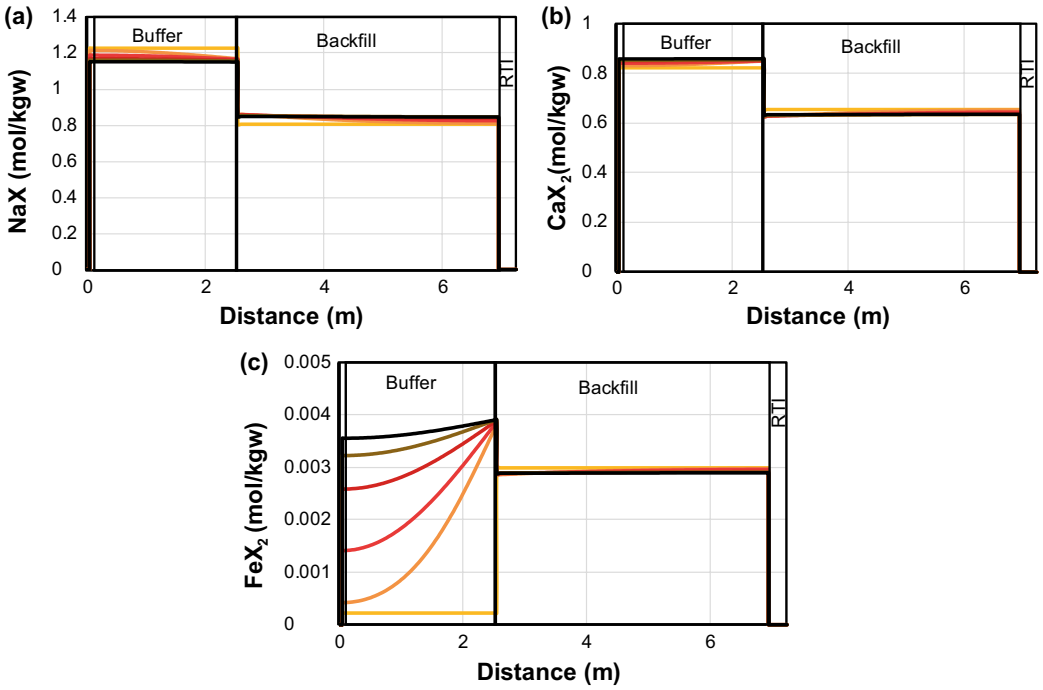

Figure 6-6. *Longitudinal profiles of Na^{+}, Ca^{2+}, and Fe^{2+} in the exchanger of the buffer and backfill domains.*

The global sulfide production associated with reactions 6-2 and 6-4 clearly highlights the higher impact of biotic sulfide production via the organic matter path as compared to the H_2 path (Figure 6-7). In a period of 100 kyr, around 3.54 moles of sulfide are produced by biotic reactions linked to organic matter, while only $7.61 \cdot 10^{-3}$ moles are produced by the H_2 path.

Figure 6-8 (a and b) shows the global consumption of sulfide by mackinawite formation and corrosion as a function of time. As stated before, mackinawite precipitation is the only retardation process that effectively controls the concentration of sulfide and ultimately the copper corrosion. In a period of 100 kyr, 3.50 moles of mackinawite are produced (Figure 6-8a). Note that this process is controlled by the availability of Fe^{2+}, which in turn is controlled by partial dissolution of siderite present in the backfill (Figure 6-4c).

All the above-mentioned processes determine sulfide fluxes reaching the canister (Figure 6-8c), which vary between $2 \cdot 10^{-7}$ and $2 \cdot 10^{-6}$ mol/(m^2 y) during the course of the 100 kyr simulation. There is a sulfide flux decrease after 100 years due to an increase in mackinawite precipitation (Figure 6-8a), caused by an increase in iron concentrations in the backfill (Figure 6-3e). After about 2 kyr, the hydrogen formed by canister corrosion reaches the RTI (Figure 6-3d), producing sulfide (Figure 6-7b) and increasing sufide fluxes. The results indicate that only a total amount of 0.044 moles of sulfide are consumed at the canister in the corrosion process (per m^2 of canister surface). The estimated corrosion depth over time is shown in Figure 6-8d. After 100 kyr the corrosion depth is ~0.624 µm. It is noted that the corrosion depth is highly dependent on geometrical assumptions of the adopted 1D model. This is due to the fact that the distance of the sulfide source to the canister is very important in determining the concentration gradients and the time needed by sulfide to diffuse towards the canister. Indeed, a more realistic value should result from a 3D representation of the near-field system. In the present simulations, the geometry represents a vertical profile traversing the RTI, the backfill, the buffer, and the canister. This assumption is not conservative, as the source of sulfide in the model (the RTI domain) is at a distance that is much larger than the RDI and the rock tunnel interface below the tunnel floor.

The budget of total sulfide at 100 kyr is presented in Table 6-8. It is clearly seen that the path of sulfate reduction that governs the system is *via* organic matter (CH_2O), accounting for more than 99 % of the total sulfide produced. The H_2 path only produces the remaining 0.8 %.

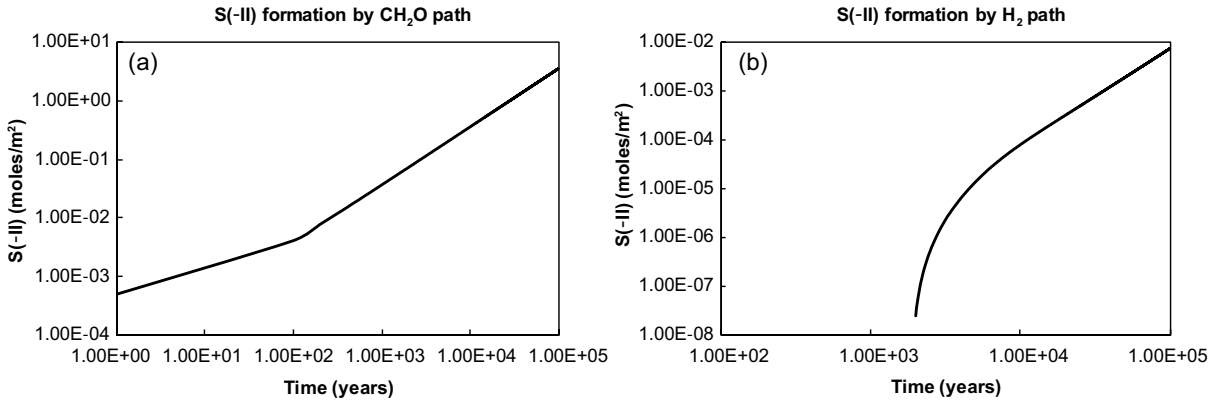

Figure 6-7. *Cumulative Global production of sulfide by microbial-induced sulfate reduction in the RTI domain as a function of time, considering a cross-section of 1 m^2: (a) CH_2O path and (b) H_2 path.*

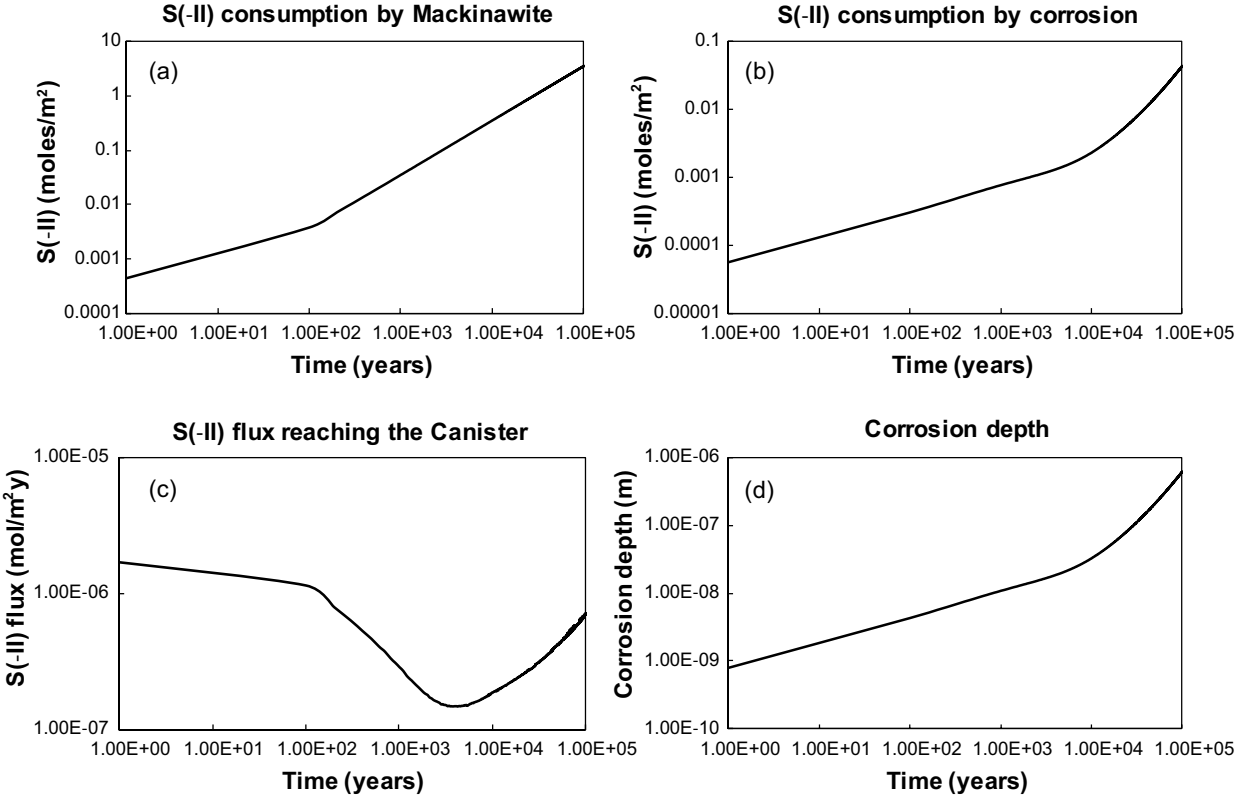

Figure 6-8. *Cumulative aqueous sulfide consumption by (a) mackinawite precipitation and (b) corrosion in moles (considering a cross-section of 1 m^2), flux of sulfide reaching the canister (c), and corrosion depth over time (d).*

Of the total sulfide produced, less than 1 % accumulates as dissolved sulfide in the porewater of the different domains, while most of the total sulfide produced (~99 %) precipitates as mackinawite at the expense of siderite dissolution in the backfill. Only ~1 % of the sulfide produced reaches the canister and corrodes the copper. Sulfide escaping the system through the rock boundary at 5 m from the RTI is negligible ($<2.5 \cdot 10^{-10}$ moles/year). This is mainly due to the very low porosity and diffusivity of the rock, which results in a very small diffusive flux of sulfide out of the system even though the concentration gradient is relatively large.

Table 6-8. Sulfide budget of the Base Case.

Produced sulfide (moles/m²)			Consumed sulfide (moles/m²)				Corrosion depth (µm)
CH_2O path	H_2 path	Total	Mackinawite	Porewater	Corrosion	Total	
3.54	0.00761	3.55	3.50 (98.71 %)	0.00948 (0.27 %)	0.044 (1.24 %)	3.55	0.624

The results of the Base Case indicate that the sulfate reduction processes in the RTI are limited by the flux of dissolved organic matter from the backfill. As seen in Figure 6-3, DOM concentrations tend to zero in the RTI (a value of $1 \cdot 10^{-8}$ M is the threshold under which kinetic reactions of sulfide production are deactivated in the model for numerical efficiency and stability). At the same time, sulfate concentrations are high, controlled by gypsum in the backfill. This means that kinetic reactions are faster than diffusive fluxes of DOM from backfill to RTI.

To analyse this in more detail, the Damköhler number (D_a) for DOM at the interface between backfill and RTI is estimated. This dimensionless number is the ratio between the reaction rate (mol/s) and the diffusion rate (mol/s) (for a purely diffusive transport scenario). A value much higher than 1 indicates that kinetics is faster than diffusion and therefore that diffusion is the limiting process. The details of this calculation are presented in Table 6-9. It can be observed that the value is ~2200, which is much higher than 1. This is so even when considering that the volume of RTI where sulfide production occurs is limited to 1 cm from the interface (i.e. a volume of 10 litres, cross-section of 1 m^2). This calculation indicates that DOM is consumed much faster in the RTI than the transport capacity of the system at the interface.

Table 6-9. Damköhler number (D_a) of the diffusion-reaction of dissolved organic matter (DOM) across the backfill-RTI interface.

Process	Term	Quantity	Unit
DOM consumption by sulfate reduction	MT= Monod Terms (reaction 6-7)	0.167	-
	k_{max}	1.5E−04	1/s
	[X]	3.54E−07	mol/L_{medium}
	V = volume RTI (assuming 1 cm)	10.0	L_{medium}
	Reaction rate: $R = V \cdot [X] \cdot k_{max} \cdot MT \cdot 2$	1.77E−10	mol/s
Diffusion of DOM across interface	$De_{interface}$ (assuming RTI value)	5.0E−13	m^2/s
	ϕ (porosity)	0.01	m^3_{H2O} / m^3_{medium}
	∇c (concentration gradient assuming 1 cm)	16.1	mol/ ($m^3_{H2O} \cdot m$)
	A (cross-section area)	1.0	m^2
	$J_{diff} = A\phi\, De_{interface} \nabla c$	8.05E−14	mol/s
$D_a = R / J_{diff}$	$D_a = R / J_{diff}$	2198	-

6.3.3 Base Case simplifications

A simplified model of the Base Case has been implemented to obtain a reduced system that effectively captures all the features described in the previous section, both qualitatively and quantitatively. The objectives of developing this model are:

- To test the sensitivity of the results to a number of simplifications of the system
- To obtain a simple model that can be more easily implemented in and compared with the hybrid model.

A summary of the simplifications that have been applied is presented in Table 6-10. Firstly, aqueous species that presented concentrations below a threshold value of 10^{-6} M throughout the simulation time and over the entire model domain in the full Base Case were eliminated from the database. A list of the species considered in each case is presented in Appendix D. Moreover, the chemical elements K, Mg, and Si were excluded from the system. This simplification is based on the limited contribution of these elements to the processes affecting sulfide production, transport, and consumption in the present setup. Finally, the rock domain was removed and replaced by a

closed boundary at the RTI-rock interface. This is supported by the negligible impact of the rock in the sulfide budget (Section 6.3.2). The geochemical composition of each domain implemented in the model is given in Table 6-11.

Table 6-10. Summary of simplifying assumptions made in the simplified Base Case with respect to the full Base Case. Aqueous chemical species that do not present concentrations above the threshold value during the whole full Base Case simulation are removed from the the thermodynamic database Thermochimie v9b (Giffaut et al. 2014).

Simulation	Threshold value (mol/kg_{water})	K, Mg and Si included	Species in exchanger	Rock
Full Base Case	None	Yes	Na, K, Ca, Mg, Fe	Yes
Simplified Base Case	$1 \cdot 10^{-6}$	No	Na, Ca, Fe	No

Table 6-11. Geochemical composition of each model domain in the simplified Base Case: minerals, porewater and exchanger. Na is used for charge balancing the solutions.

Domain	Canister	Buffer	Backfill	RTI
Pore solution				
pH	7.17	7.17	7.21	7.07
pe	−3.4	−3.4	−3.4	−3.3
Total concentrations (mol/kg_{water})				
C	8.92E−04	8.92E−04	8.72E−04	1.72E−03
Ca	3.99E−02	3.99E−02	3.51E−02	1.62E−02
Cl	2.22E−01	2.22E−01	1.76E−01	1.13E−01
DOM	1.67E−04	1.67E−04	1.67E−04	1.00E−10
Fe	1.10E−05	1.10E−05	1.79E−04	5.70E−06
Na (charge)	1.80E−01	1.80E−01	1.43E−01	8.23E−02
S(-II)	1.20E−06	1.20E−06	6.00E−07	0
S(VI)	1.87E−02	1.87E−02	1.84E−02	0
Cation exchange (mol/kg_{water})				
NaX	-	1.23E+00	8.07E−01	-
CaX_2	-	8.21E−01	6.54E−01	-
FeX_2	-	2.23E−04	2.98E−03	-
Mineral phases (mol/kg_{water})				
Calcite	-	5.10E−01	8.79E−01	0
Gypsum	-	8.48E−02	4.41E−01	-
SOM	-	3.04E−01	3.33E−01	-
Siderite	-	0	3.80E−01	-
Mackinawite	-	0	0	0

As shown in Figure 6-9 and Table 6-12, these simplifications do not affect the final results obtained for the temporal evolution of key parameters to any significant extent. The evolution of sulfide production and corrosion depth is virtually unaffected. Therefore, the simplifications will be applied to all simulation cases presented in the following sections, including all variant cases and hybrid models. The simplified Base Case is referred to as Base Case from now on and is used for comparison purposes.

6.3.4 Effect of surface complexation

A model was implemented using the traditional reactive transport approach that includes surface complexation reactions due to mineral edge sites in the backfill and buffer domains. The motivation for this is that surface complexation can buffer changes in pH to some extent and thus affect the transport of sulfide from the RTI towards the canister. The thermodynamic constants for protonation and deprotonation reactions and site capacities were set according to the surface complexation model proposed by Bradbury and Baeyens (1997), with a dry density of 1,570 kg/m^3.

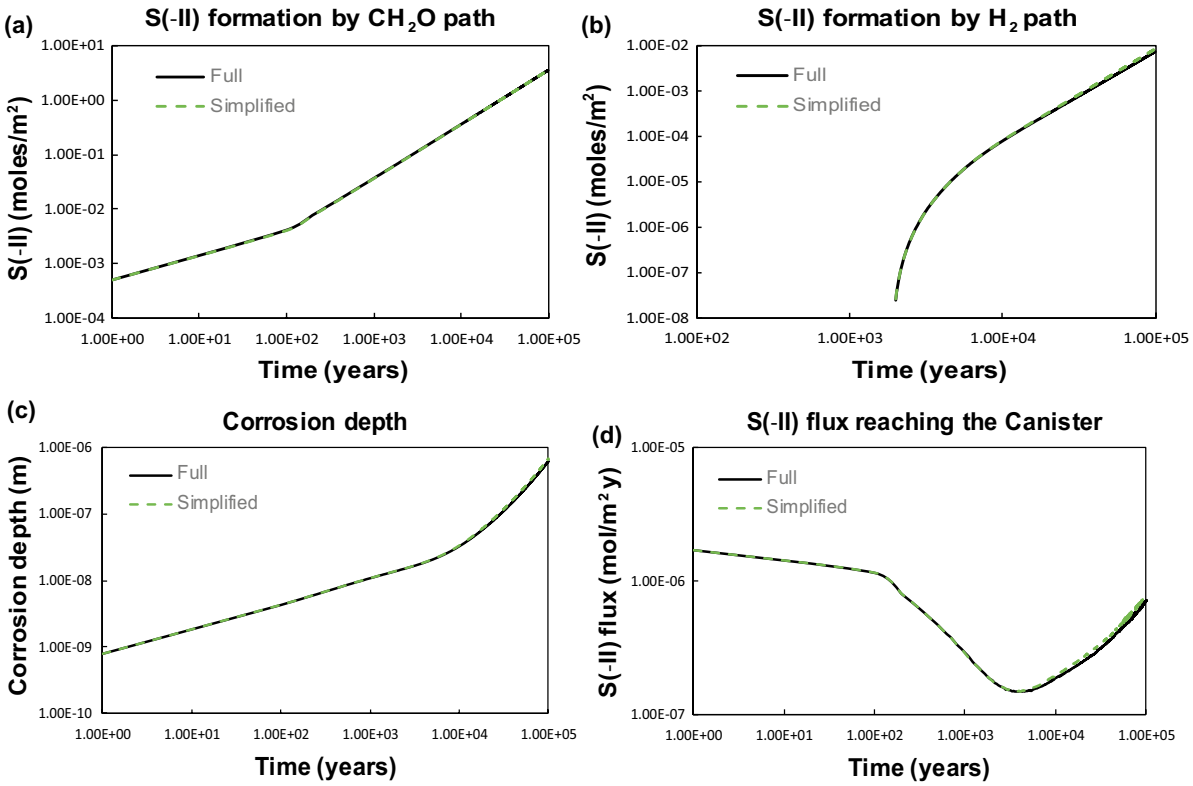

Figure 6-9. *Comparison of results: Full Base Case vs. simplified Base Case (corrosion depth, sulfide budget plots): cumulative sulfide generation (in moles/m^2) by (a) CH_2O path and (b) H_2 path, (c) corrosion depth (m), and (d) sulfide flux reaching the canister (moles/m^2 year).*

Figure 6-10 displays the pH buffering effect of including surface complexation reactions and its impact on the sulfide concentrations. Including protonation/deprotonation reactions has the effect of buffering the pH. As a result, the pH decreases more slowly near the RTI in the case with surface complexation. After 100 kyr, the pH drops to 6.5 in the case without surface complexation reactions, while including the Bradbury and Baeyens (1997) model buffers the pH to a value of 6.7. The effect of a different pH is a shift in the mackinawite – sulfide equilibrium, ultimately leading to lower concentrations of aqueous sulfide (Figure 6-10b). Figure 6-11 shows the total sulfide and HS^- concentrations in equilibrium with mackinawite at different pH values using ThermoChimie for the geochemical conditions of the backfill. As can be observed, sulfide concentrations are highly dependent on the pH value, with changes of several orders of magnitude even in the pH range going from 6 to 8.

A summary of sulfide production and consumption for both cases is given in Table 6-12. Mackinawite precipitation is increased by only 0.6 % in the case with surface complexation reactions (Figure 6-12c), and canister corrosion decreases by 33 % after 100 kyr (Figure 6-12e). Therefore, it may be concluded that the effect of including surface complexation reactions is not significant, although it is not negligible. Nonetheless, surface complexation reactions are not considered in the simulations of the variant cases (Section 7), except for the case studying interface metals.

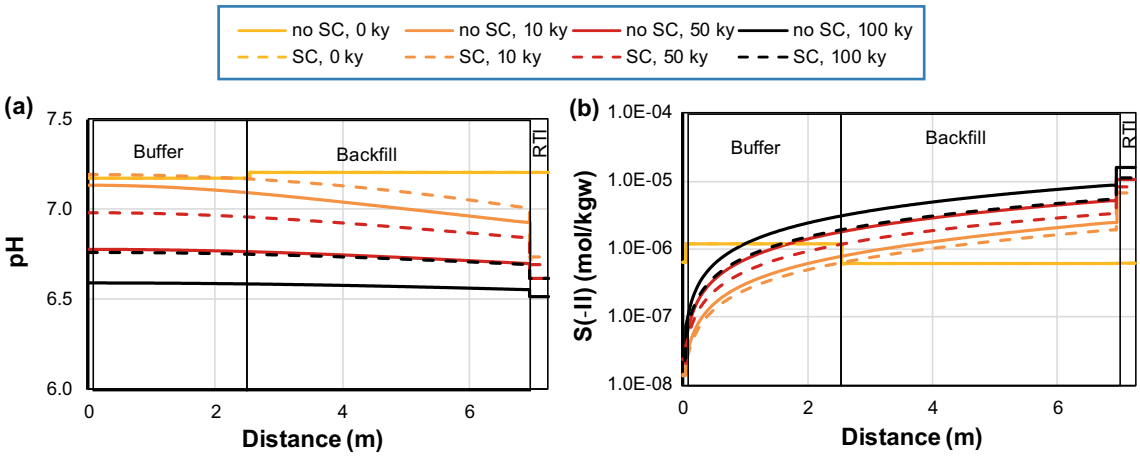

Figure 6-10. Longitudinal profiles of (a) pH and (b) aqueous sulfide for different times in the modelled system for the Base Case with (SC) and without (no SC) surface complexation.

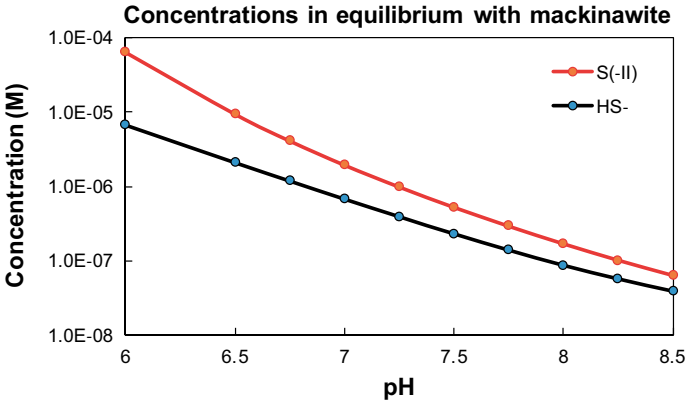

Figure 6-11. Equilibrium concentration (in M) of total sulfide and of species HS^- obtained after equilibrating mackinawite with the initial backfill pore solution (with a fixed Fe concentration of $1.82 \cdot 10^{-4}$ M) for different values of pH.

Table 6-12. Sulfide budget in the modelled system at 100 000 years: production, consumption, and accumulation. Amount of sulfide in moles, considering a cross-section of 1 m^2. Percentages are given with respect to total sulfide produced.

Case	Produced sulfide (moles)			Consumed sulfide (moles)				Corrosion depth (μm)
	CH_2O path	H_2 path	Total	Mackinawite	Porewater	Corrosion	Total	
Base Case	3.54	7.61E−03	3.55	3.50 (98.7 %)	9.48E−03 (0.268 %)	4.40E−02 (1.24 %)	3.55	0.624
Simplified Base Case	3.55	8.21E−03	3.56	3.50 (98.6 %)	1.02E−02 (0.287 %)	4.76E−02 (1.34 %)	3.56	0.675
Base Case with Surface Complexation	3.55	5.62E−03	3.56	3.52 (99.0 %)	5.49E−03 (0.15 %)	3.18E−02 (0.89 %)	3.56	0.451

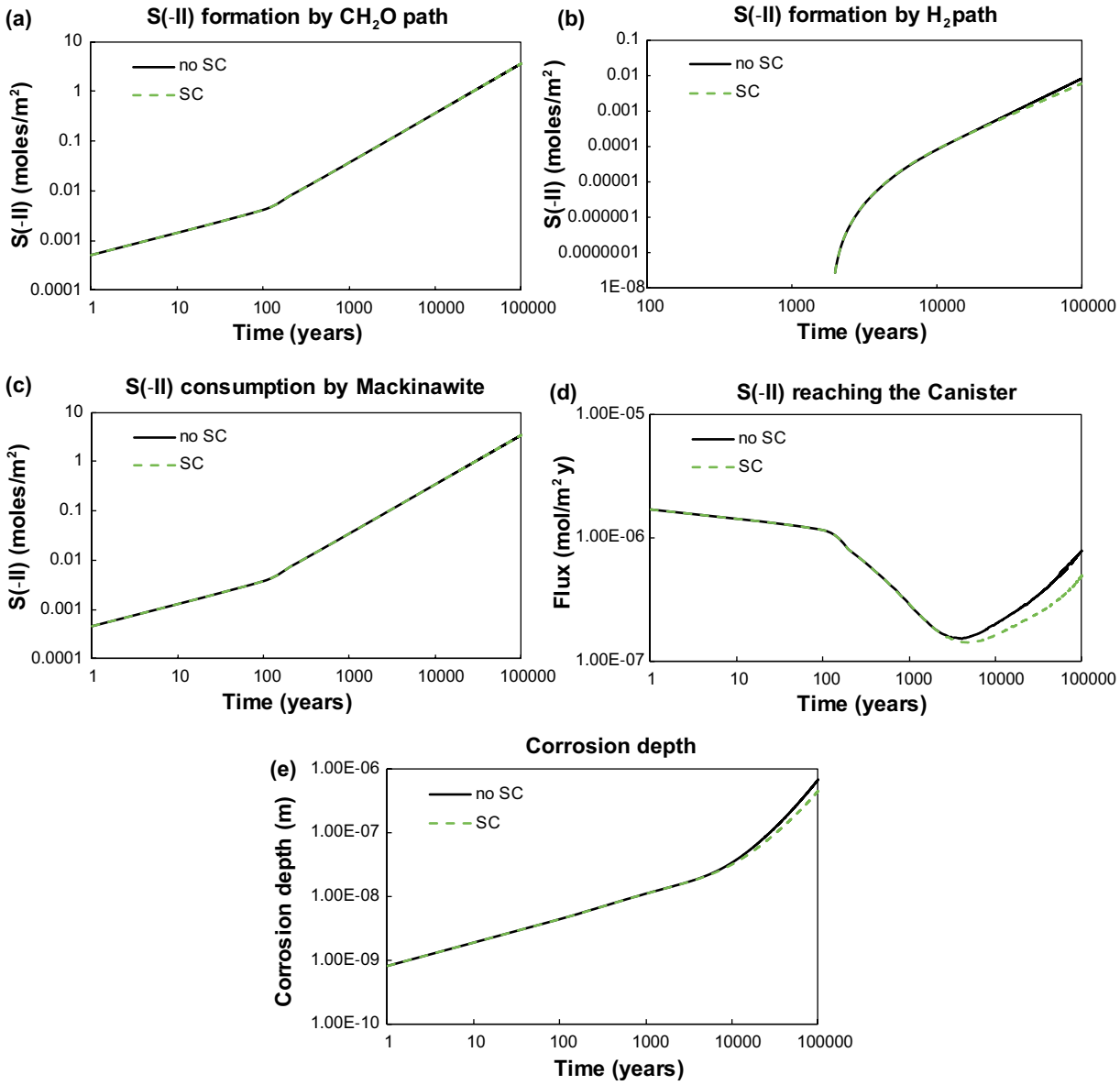

Figure 6-12. *Comparison of results: Base Case vs. Base Case with surface complexation reactions (corrosion depth, sulfide budget plots): cumulative sulfide generation (in moles/m^2) by (a) CH_2O path and (b) H_2 path, (c) sulfide consumption by mackinawite precipitation, (d) sulfide flux reaching the canister (moles/m^2 year), and (e) corrosion depth (m).*

6.4 Hybrid model

In this section, the Base Case presented in sections 6.2 and 6.3 is adapted to the hybrid model (Section 2). The objective of this simulation case is to assess the effect of considering a different conceptual model of reactive transport in compacted bentonite on the estimates of sulfide production and corrosion depth. This assessment is based on comparing the hybrid model with the (simplified) Base Case implemented using the traditional single-porosity and cation exchange reactive transport approach (Section 6.3).

6.4.1 Model setup and implementation

The geometry of the system is identical to the simplified Base Case and considers a vertical profile from the canister top lid to the RTI (0.3 m), traversing the buffer (2.5 m) and backfill (4.4 m) domains. The bedrock is not modelled in this case, given the negligible impact on the results when compared to the full Base Case (see previous section). Closed boundary conditions (zero diffusive flux) are considered at the RTI-bedrock interface and at the left of the canister (x = 0 m).

The modelled processes are exactly the same as in the Base Case presented in sections 6.2 and 6.3, and so is the mineralogical composition, total porosity, and dry density. For simplification purposes, the cation exchange capacity of the buffer and backfill are considered the same and equal to that of the backfill (2.12 eq/kg).

Total porosity is partitioned into interlayer and bulk porosities. Given the lack of reliable data on the distribution of porosities, it is assumed here for the buffer and backfill that for a dry density of 1,570 kg/m^3, 90 % of the total porosity is interlayer water. The remaining 10 % represents the disconnected bulk porosity (Table 6-13). The effect of using different porosity distributions on solute transport has been analysed in Section 2.4.2 and has been tested in Section 5.3. Results indicate that increasing the fraction of bulk porosity slows down solute transport. On the other hand, increasing the bulk porosity has the effect of higher reactivity of the system, which in the hybrid model depends on the bulk water mass to solid mass. Table 6-13 summarizes the distribution of porosities in the different model domains. Pore diffusion coefficients are also given in Table 6-13.

Table 6-13. Porosity distributions and pore diffusion coefficients in each model domain.

Domain	ϕ_{tot}	ϕ^{bulk}	ϕ^{int}	$D_p = D_c$ (m^2/s)
Canister	0.43	0.043	0.387	$5 \cdot 10^{-10}$
Buffer	0.43	0.043	0.387	$5 \cdot 10^{-11}$
Backfill	0.43	0.043	0.387	$5 \cdot 10^{-11}$
RTI	0.01	0.010	0.000	$5 \cdot 10^{-11}$

Given the partition of total porosity between bulk and interlayer porosities in the hybrid model, the porewater composition of each domain needs to be calculated. This can be done in several ways. In this work, the assumption is that the water composition of the bulk porosity is the same as the one reported for the simplified Base Case (Table 6-11). The reason behind this assumption is the need to have a model that is as similar as possible to the Base Case setup, for comparison purposes. The interlayer water composition is calculated as a function of the bulk composition using Equation 2-15 and the CEC value of the backfill (Table 6-14 and Table 6-15). It is noted that with this methodology the initial interlayer porewater composition does not depend on the choice of bulk/interlayer porosity distribution.

Table 6-14. Backfill porewater compositions for bulk and interlayer porosities, and variables used to calculate these compositions. z_i is the species charge, c_{bulk} and c_{int} the species concentrations in the bulk and interlayer waters respectively, γ_{bulk} and γ_{int} the species activity coeficients in the bulk and interlayer waters respectively, and Γ the ratio between the activity coefficients in the bulk and interlayer solutions (Equation 2.16). The pH of the bulk water is 7.21 and of the interlayer water 6.30. The initial value of the Donnan factor f_D is 0.123.

Species	z_i	c_{bulk} (mol/kgw)	Bulk activity	γ_{int}	γ_{bulk}	Γ	c_{int} (mol/kgw)	$c_{int} \cdot z_i$	$c_{bulk} \cdot z_i$
OH^-	–1	2.26E–07	1.61E–07	0.711	0.711	1.00	2.77E–08	–2.77E–08	–2.26E–07
H^+	+1	8.55E–08	6.19E–08	0.724	0.724	1.00	6.97E–07	6.97E–07	8.55E–08
HCO_3^-	–1	6.84E–04	4.87E–04	0.711	0.711	1.00	8.39E–05	–8.39E–05	–6.84E–04
CO_2	0	6.79E–05	6.79E–05	1.000	1.000	1.00	6.79E–05	0	0
$Ca(HCO_3)^+$	+1	7.62E–05	5.52E–05	0.724	0.724	1.00	6.21E–04	6.21E–04	7.62E–05
$Na(HCO_3)$	0	2.69E–05	2.69E–05	1.000	1.000	1.00	2.69E–05	0	0
$CaCO_3$	0	5.50E–06	5.50E–06	1.000	1.000	1.00	5.50E–06	0	0
CO_3^{-2}	–2	1.33E–06	3.68E–07	0.030	0.277	9.25	1.85E–07	–3.69E–07	–2.65E–06
$Na(CO_3)^-$	–1	9.46E–07	6.73E–07	0.712	0.712	1.00	1.16E–07	–1.16E–07	–9.46E–07
$Fe(CO_3)$	0	7.76E–06	7.76E–06	1.000	1.000	1.00	7.76E–06	0	0
$FeH(CO_3)^+$	+1	7.98E–07	5.78E–07	0.724	0.724	1.00	6.50E–06	6.50E–06	7.98E–07
$Fe(CO_3)_2^{-2}$	–2	5.92E–10	1.64E–10	0.030	0.277	9.25	8.25E–11	–1.65E–10	–1.18E–09
Ca^{+2}	+2	2.91E–02	9.01E–03	0.949	0.309	0.33	6.30E–01	1.26E+00	5.83E–02
$CaCl^+$	+1	7.78E–04	5.63E–04	0.724	0.724	1.00	6.34E–03	6.34E–03	7.78E–04
CaCl2	0	3.07E–05	3.07E–05	1.000	1.000	1.00	3.07E–05	0	0
$Ca(SO_4)$	0	5.07E–03	5.07E–03	1.000	1.000	1.00	5.07E–03	0	0
Cl^-	–1	1.71E–01	1.22E–01	0.711	0.711	1.00	2.10E–02	–2.10E–02	–1.71E–01
NaCl	0	3.79E–03	3.79E–03	1.000	1.000	1.00	3.79E–03	0	0
$FeCl^+$	+1	1.00E–05	7.26E–06	0.724	0.724	1.00	8.16E–05	8.16E–05	1.00E–05
$FeCl_3^-$	–1	1.15E–06	8.19E–07	0.712	0.712	1.00	1.41E–07	–1.41E–07	–1.15E–06
DOM	0	1.67E–04	1.76E–03	10.552	10.552	1.00	1.67E–04	0	0
Fe^{+2}	+2	1.39E–04	4.31E–05	0.983	0.309	0.31	2.91E–03	5.82E–03	2.79E–04
$Fe(HS)^+$	+1	2.40E–07	1.74E–07	0.724	0.724	1.00	1.95E–06	1.95E–06	2.40E–07
H_2	0	1.99E–11	1.99E–11	1.000	1.000	1.00	1.99E–11	0	0
H_{tr}	0	1.00E–10	1.06E–10	1.055	1.055	1.00	1.00E–10	0	0
Na^+	+1	1.36E–01	9.84E–02	0.724	0.724	1.00	1.11E+00	1.11E+00	1.36E–01
$Na(SO_4)^-$	–1	3.32E–03	2.36E–03	0.712	0.712	1.00	4.08E–04	–4.08E–04	–3.32E–03
HS^-	–1	2.49E–07	1.84E–07	0.740	0.740	1.00	3.05E–08	–3.05E–08	–2.49E–07
H_2S	0	1.11E–07	1.11E–07	1.000	1.000	1.00	1.11E–07	0	0
SO_4^{-2}	–2	9.94E–03	2.76E–03	0.030	0.277	9.25	1.39E–03	–2.77E–03	–1.99E–02
$H(SO_4)^-$	–1	2.29E–08	1.63E–08	0.712	0.712	1.00	2.81E–09	–2.81E–09	–2.29E–08
$Fe(SO_4)^+$	+1	8.10E–20	5.87E–20	0.724	0.724	1.00	6.60E–19	6.60E–19	8.10E–20
							Totals	2.36E+00	6.23E–06

As stated in previous sections (Section 2.3.3 and Section 4), there are at present large uncertainties regarding the values of interlayer activity coefficients, as well as in the selectivity coefficients. Therefore, in this study it is assumed, as a first approximation, that most activity coefficients are equal in the interlayer and in the bulk solutions. The ratio between these two coefficients is therefore equal to 1 (Table 6-14 and Table 6-15). The exceptions are divalent cations (Ca^{2+} and Fe^{2+}) and divalent anions (SO_4^{2-}, $Fe(CO_3)_2^{2-}$, and CO_3^{2-}). For divalent cations, experimental data on selectivity coefficients for the exchange between Na^+ and Ca^{2+} or Fe^{2+} can be used to derive interlayer activity coefficients (see Section 2.3.4 and Section 4). For the Base Case, the selectivity coefficients dataset from Bradbury and Baeyens (2002) is used, as specified in Table 6-16. For Fe^{2+}, data from Charlet and Tournassat (2005) is used in the Base Case. Note that during the simulation the activity coefficients in the bulk and interlayer water may change, but the corresponding selectivity coefficients will remain constant.

Table 6-15. Buffer porewater compositions for bulk and interlayer porosities, and variables used to calculate these compositions. z_i is the species charge, c_{bulk} and c_{int} the species concentrations in the bulk and interlayer waters respectively, γ_{bulk} and γ_{int} the species activity coeficients in the bulk and interlayer waters respectively, and Γ the ratio between the activity coefficients in the bulk and interlayer solutions (Equation 2.16). The pH of the bulk water is 7.17 and of the interlayer water 6.31. The initial value of the Donnan factor f_D is 0.137.

Species	z_i	c_{bulk} (mol/kgw)	Bulk activity	γ_{int}	γ_{bulk}	Γ	c_{int} (mol/kgw)	$c_{int} \cdot z_i$	$c_{bulk} \cdot z_i$
OH^-	–1	2.10E–07	1.47E–07	0.699	0.699	1.00	2.88E–08	–2.88E–08	–2.10E–07
H^+	+1	9.46E–08	6.75E–08	0.713	0.713	1.00	6.90E–07	6.90E–07	9.46E–08
HCO_3^-	–1	6.93E–04	4.85E–04	0.699	0.699	1.00	9.50E–05	–9.50E–05	–6.93E–04
CO_2	0	7.37E–05	7.37E–05	1.000	1.000	1.00	7.37E–05	0.00E+00	0.00E+00
$Ca(HCO_3)^+$	+1	8.43E–05	6.01E–05	0.713	0.713	1.00	6.15E–04	6.15E–04	8.43E–05
$Na(HCO_3)$	0	3.31E–05	3.31E–05	1.000	1.000	1.00	3.31E–05	0.00E+00	0.00E+00
$CaCO_3$	0	5.50E–06	5.50E–06	1.000	1.000	1.00	5.50E–06	0.00E+00	0.00E+00
CO_3^{-2}	–2	1.29E–06	3.36E–07	0.030	0.260	8.66	2.11E–07	–4.21E–07	–2.59E–06
$Na(CO_3)^-$	–1	1.09E–06	7.61E–07	0.699	0.699	1.00	1.49E–07	–1.49E–07	–1.09E–06
$Fe(CO_3)$	0	4.58E–07	4.58E–07	1.000	1.000	1.00	4.58E–07	0.00E+00	0.00E+00
$FeH(CO_3)^+$	+1	5.20E–08	3.71E–08	0.713	0.713	1.00	3.79E–07	3.79E–07	5.20E–08
$Fe(CO_3)_2^{-2}$	–2	3.41E–11	8.85E–12	0.030	0.260	8.66	5.55E–12	–1.11E–11	–6.81E–11
Ca^{+2}	+2	3.36E–02	9.86E–03	0.922	0.293	0.32	5.69E–01	1.14E+00	6.73E–02
$CaCl^+$	+1	1.07E–03	7.60E–04	0.713	0.713	1.00	7.77E–03	7.77E–03	1.07E–03
CaCl2	0	5.10E–05	5.10E–05	1.000	1.000	1.00	5.10E–05	0.00E+00	0.00E+00
$Ca(SO_4)$	0	5.09E–03	5.09E–03	1.000	1.000	1.00	5.09E–03	0.00E+00	0.00E+00
Cl^-	–1	2.15E–01	1.50E–01	0.699	0.699	1.00	2.95E–02	–2.95E–02	–2.15E–01
NaCl	0	5.78E–03	5.78E–03	1.000	1.000	1.00	5.78E–03	0.00E+00	0.00E+00
$FeCl^+$	+1	8.09E–07	5.77E–07	0.713	0.713	1.00	5.90E–06	5.90E–06	8.09E–07
$FeCl_3^-$	–1	1.42E–07	9.90E–08	0.700	0.700	1.00	1.94E–08	–1.94E–08	–1.42E–07
DOM	0	1.67E–04	1.78E–04	1.067	1.067	1.00	1.67E–04	0.00E+00	0.00E+00
Fe^{+2}	+2	9.49E–06	2.78E–06	0.955	0.293	0.31	1.55E–04	3.10E–04	1.90E–05
$Fe(HS)^+$	+1	4.86E–08	3.47E–08	0.713	0.713	1.00	3.55E–07	3.55E–07	4.86E–08
H_2	0	2.02E–11	2.02E–11	1.000	1.000	1.00	2.02E–11	0.00E+00	0.00E+00
H_{tr}	0	1.00E–10	1.07E–10	1.067	1.067	1.00	1.00E–10	0.00E+00	0.00E+00
Na^+	+1	1.71E–01	1.22E–01	0.713	0.713	1.00	1.24E+00	1.24E+00	1.71E–01
$Na(SO_4)^-$	–1	3.83E–03	2.68E–03	0.699	0.699	1.00	5.25E–04	–5.25E–04	–3.83E–03
HS^-	–1	7.76E–07	5.70E–07	0.735	0.735	1.00	1.06E–07	–1.06E–07	–7.76E–07
H_2S	0	3.76E–07	3.76E–07	1.000	1.000	1.00	3.76E–07	0.00E+00	0.00E+00
SO_4^{-2}	–2	9.73E–03	2.53E–03	0.030	0.260	8.66	1.59E–03	–3.17E–03	–1.95E–02
$H(SO_4)^-$	–1	2.33E–08	1.63E–08	0.699	0.699	1.00	3.19E–09	–3.19E–09	–2.33E–08
$Fe(SO_4)^+$	+1	5.25E–21	3.74E–21	0.713	0.713	1.00	3.83E–20	3.83E–20	5.25E–21
							Totals	2.36E+00	4.38E–05

Table 6-16. Selectivity coefficients (K) for Na^+, Ca^{2+}, and Fe^{2+} from Bradbury and Baeyens (2002) and Charlet and Tournassat (2005), and resulting interlayer activity coefficients (assuming that the value for Na^+ is the same as in bulk water). See Section 2.3.4 for more details.

Exchange reaction	K	γ_{int} (backfill)	γ_{int} (buffer)
$X^- + Na^+ = NaX$	1.0	0.724	0.713
$2X^- + Ca^{2+} = CaX_2$	2.6	0.949	0.922
$2X^- + Fe^{2+} = FeX_2$	2.51	0.983	0.955

For the divalent anion SO_4^{2-}, interpretation of experimental data (Birgersson 2019) suggests that the activity coefficient in interlayer water is much lower than in bulk water. The estimated value is ~0.03 (instead of ~0.3 in bulk water). By analogy, the same activity coefficient for the interlayer is assumed for $Fe(CO_3)_2^{2-}$, and CO_3^{2-} species. The value of 0.03 is considered constant throughout the simulation.

It is important to note that the hybrid model considers both interlayer and bulk porewaters, as opposed to the traditional model that considers bulk porewater only. Therefore, the mass of solute in the interlayer in the hybrid model is in excess of what is considered in the traditional model. The exceptions are of course the cations Na^{+}, Ca^{+2}, and Fe^{+2}, which are consistent in both models since cation exchange reactions for these three cations are included in the traditional model. The aqueous sulfide and sulfate species in the bulk pore water include anions (HS^{-}, $H(SO_4)^{-}$, $Na(SO_4)^{-}$, SO_4^{2-}), but also neutral species (H_2S, $Ca(SO_4)$) and positively charged species ($Fe(HS)^{+}$, $Fe(SO_4)^{+}$). As a result, the total mass of sulfide and sulfate species in the interlayer water is substantial, especially when considering that the interlayer porosity is 90 % of the total porosity. This is illustrated in Table 6-17. As may be observed, the Donnan equilibrium constraint between bulk and interlayer water leads to a very different distribution of aqueous species in each porosity type. While in the bulk porosity sulfate and sulfide are mostly in the form of SO_4^{2-} (52 %) and HS^{-} (65 %), in the interlayer water these fractions are significantly reduced (22 % and 13 %, respectively). Initially, the mass of sulfate and sulfide aqueous species in the interlayer porosity is respectively 3.5 and 6.3 times that of the bulk porosity.

Table 6-17. Sulfide and sulfate aqueous species in the buffer porewater: z_i is the species charge and c_{bulk} and c_{int} the initial species concentrations in the bulk and interlayer waters respectively. Bulk and interlayer concentrations given in mol/kg of bulk and interlayer water, respectively.

Sulfate	z_i	c_{bulk} (mol/kg b.w.)	c_{int} (mol/kg i.w.)	Ratio bulk	Ratio int
$Ca(SO_4)$	0	0.00509	0.00509	0.273	0.707
$Na(SO_4)^{-}$	–1	0.00383	0.00052	0.205	0.073
SO_4^{-2}	–2	0.00973	0.00158	0.522	0.220
$H(SO_4)^{-}$	–1	2.329E–08	3.194E–09	1E–06	4E–07
$Fe(SO_4)^{+}$	1	5.247E–21	3.825E–20	3E–19	5E–18
			Total	1.000	1.000
Sulfide	**z_i**	**c_{bulk} (mol/kg b.w.)**	**c_{int} (mol/kg i.w.)**	**Ratio bulk**	**Ratio int**
$Fe(HS)^{+}$	1	4.863E–08	3.545E–07	0.041	0.424
HS^{-}	–1	7.756E–07	1.064E–07	0.646	0.127
H_2S	0	3.758E–07	3.758E–07	0.313	0.449
			Total	1.000	1.000

Interfaces between domains (canister, buffer, backfill, and RTI) are modelled as follows:

- The canister-buffer interface is considered as an extension of the bentonite buffer, which means that the canister is considered as a porous medium with the same porosity and CEC values as the buffer.
- Given that the CEC of the buffer and backfill are considered the same in this simplified case, the interface between these two domains does not imply any electrostatic potential drop (Section 2.3.1). Therefore, no specific treatment of this interface is needed.
- The backfill-RTI interface is more complex due to the fact that the RTI is treated as a porous medium with a single bulk porosity type. Therefore, at this interface the discontinuity between the transported species at each side of the interface needs to be explicitly solved (see Section 3). The interlayer concentrations in the backfill are in Donnan equilibrium with the bulk concentrations in the RTI. This equilibrium is calculated dynamically in the model taking into account the concentration discontinuity resulting from the electrostatic potential drop and ensuring mass conservation.

The 7.25 m long one-dimensional domain is discretized with finite elements ranging between 10^{-5} and 0.05 m (within the buffer and backfill) with the same mesh as in the traditional model, see Appendix C. In turn, temporal discretization is handled in iCP as follows. Communication times for the operator splitting procedure are manually set every 1 year. These define the times at which the coupling between physical and chemical processes occurs. For each time increment, Comsol solves the time dependent physics partitioning the time increment into substeps. In addition, for each time

increment, Phreeqc solves the time dependent system of equations using Runge-Kutta integration scheme for kinetic reactions (Parkhurst and Appelo 2013). More details can be found elsewhere (Nardi et al. 2014).

6.4.2 Results

In this section, the results of the Base Case hybrid model are presented and compared to the Base Case traditional model. First, the results in terms of sulfate and dissolved organic matter concentrations (DOM) in the bulk aqueous pore solution are shown in Figure 6-13. These are controlled respectively by gypsum and solid organic matter (SOM) solubilities and are very similar between both models. The small difference observed in sulfate concentrations between the traditional and hybrid models (Figure 6-13a) is probably be due to different calcium concentrations in both models, which affect the sulfate concentration in equilibrium with gypsum. As there is an excess of gypsum and SOM in the buffer and backfill, no significant changes in aqueous concentrations are observed. The production of sulfide in the RTI via the two sulfate reduction paths (see Section 6.2 for more details) is shown in Figure 6-14. Comparison with the results of the traditional model shows a relatively good agreement for the CH_2O path, which accounts for most of the total sulfide produced in the system. This result is to be expected, given that sulfide production is limited by transport of dissolved organic matter (DOM) from the backfill towards the RTI. Indeed, diffusive flux of CH_2O, a neutral species, towards the RTI is very similar in the hybrid model as compared to the traditional model. This is due to the fact that retardation induced by the bulk pores (see Equation 2-53) is in this case small (for a neutral species and the partition of porosity assumed in the Base Case, the diffusive flux is only 10 % smaller). Sulfate fluxes from backfill to RTI are also lower than in the traditional model. However, given that stoichiometrically 2 times more DOM than sulfate is needed to produce 1 mol of sulfide, and given the high sulfate concentrations in the backfill, the limiting factor is DOM diffusive fluxes entering the RTI domain.

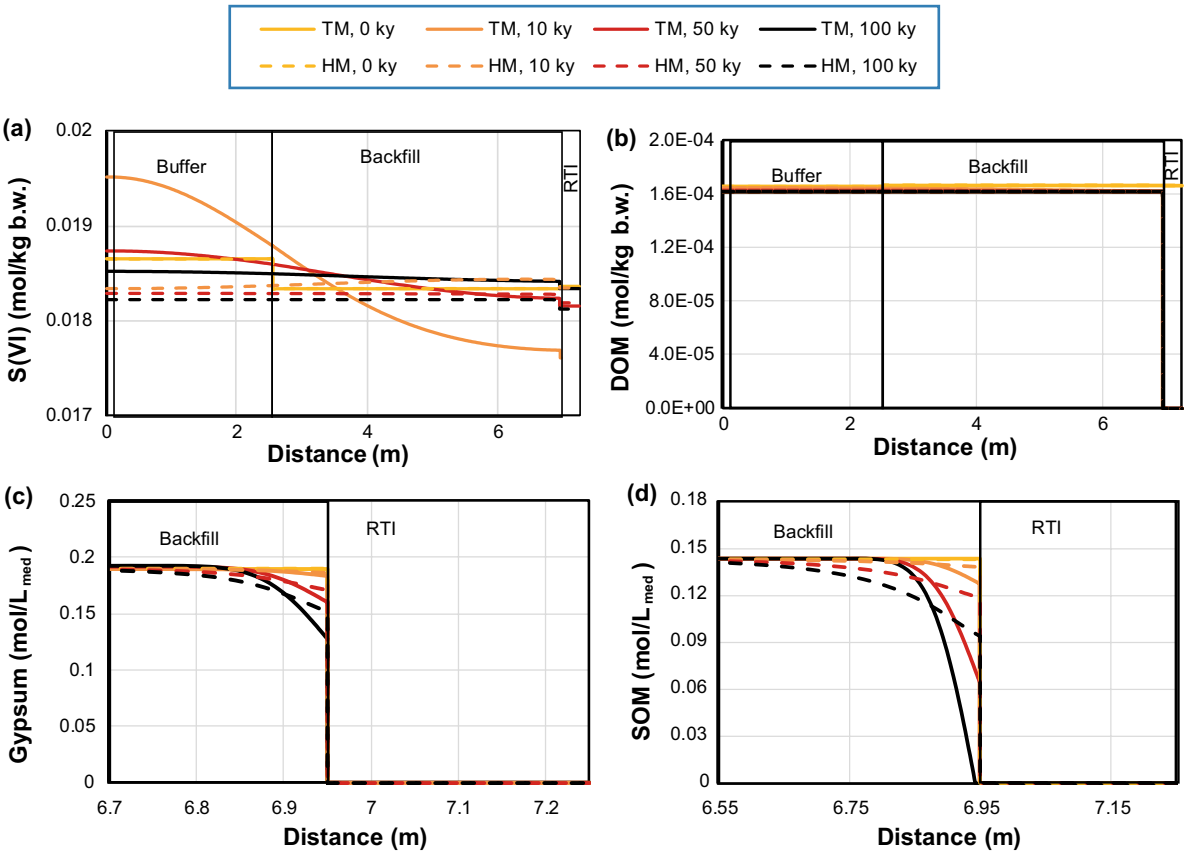

Figure 6-13. *Comparison of the results of the hybrid model (HM) and the traditional model (TM): longitudinal profiles of (a) sulfate, (b) dissolved organic matter (DOM), and zoom of the RTI-backfill interface for (c) gypsum, and (d) solid organic matter (SOM) concentrations at different times (0, 10, 50, and 100 kyr). Aqueous concentrations are given in mol per kg of bulk water while mineral concentrations are given in mol per litre of medium.*

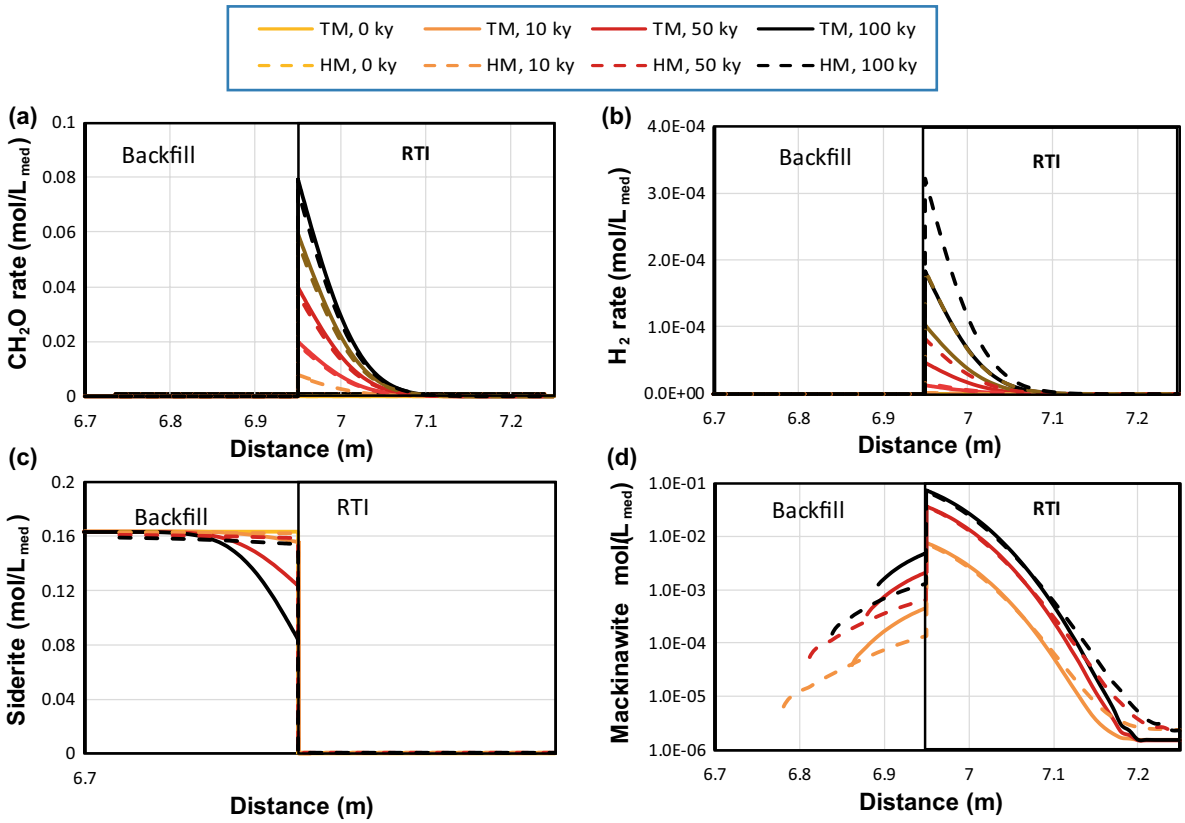

Figure 6-14. *Results of the hybrid model and comparison with the traditional model results at different times: 0, 10, 50, and 100 kyr. Longitudinal profiles in the RTI (a, b) and the backfill-RTI interface (c, d). Accumulated sulfide production at each point in the RTI via the (a) CH_2O path and (b) H_2 path and (c) siderite and (d) mackinawite concentrations in the backfill-RTI interface, in mol per litre of medium.*

On the other hand, the H_2 rate path produces more sulfide in the hybrid model than in the traditional model. This is due to larger corrosion rates in the long term for the hybrid model, as explained below. Still, the contribution to the total sulfide production is insignificant in both cases (below 1 %). The increase in sulfide concentrations in the RTI and the backfill triggers the precipitation of mackinawite. This precipitation is maintained in time due to the large availability of siderite (the source of iron), which gradually dissolves as the result of mackinawite formation. As shown in Figure 6-14c and d, there is more mackinawite precipitation and siderite dissolution in the traditional model, where this process is also more localized. In the hybrid model, the region of mackinawite precipitation is around 0.1 m larger than in the traditional model.

The sulfide concentrations, on the other hand, differ substantially as shown in Figure 6-15. This figure presents the total sulfide concentrations in the bulk porosity (Figure 6-15a), interlayer porosity (Figure 6-15b), and total porosity (Figure 6-15c). The hybrid model shows smaller sulfide concentrations in the bulk water (Figure 6-15a), due to the effect of pH on the thermodynamic equilibrium between mackinawite and sulfide (see Figure 6-16 and Figure 6-11). The pH near the RTI is in turn higher in the hybrid model due to the fact that less mackinawite precipitation releases less protons.

The sulfide concentrations in the total porewater, however, are significantly higher in the hybrid model (Figure 6-15c). This is due to the relatively high concentrations in the interlayer water (Figure 6-15b). Figure 6-17 gives more detailed information about the aqueous speciation of sulfide species in the interlayer after 100 kyr. As may be observed, most of the sulfide in the interlayer is in the form of a cation, $Fe(HS)^+$, accounting for more than 80 % of the total. The diffusive flux of this cation, given its high concentration gradient in the interlayer water, is much larger than that of the anion HS^- in the hybrid model, or even than the diffusion rate of the traditional model.

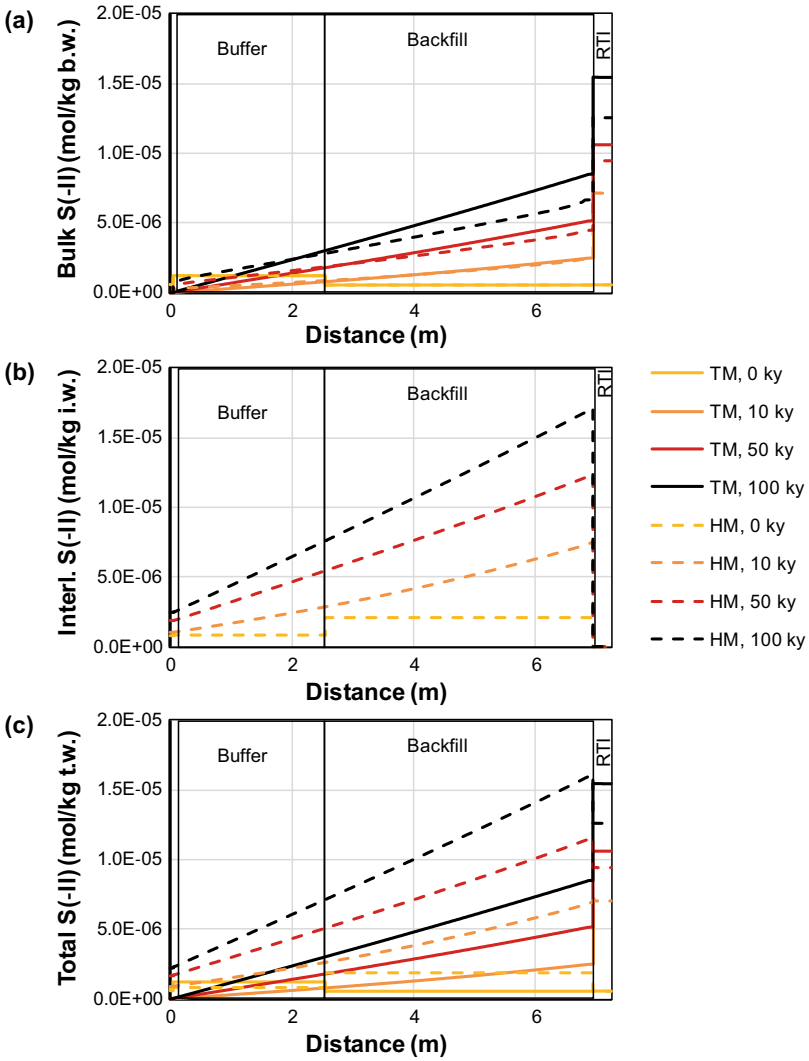

Figure 6-15. *Results of the hybrid model and comparison with the traditional model results in terms of longitudinal profiles of total sulfide concentrations (a) in bulk water (mol/kg bulk water), (b) in interlayer water (mol/kg interlayer water), and (c) in total water (mol kg of total water) at different times: 0, 10, 50, and 100 kyr.*

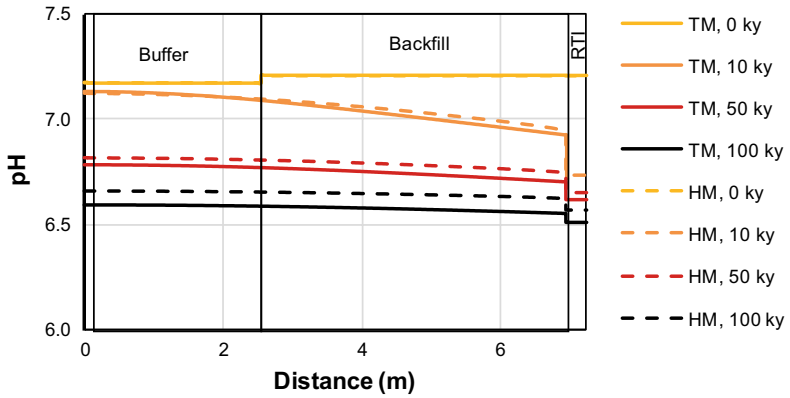

Figure 6-16. *Longitudinal profiles of pH obtained with the hybrid model and comparison with the traditional model results at different times: 0, 10, 50, and 100 kyr.*

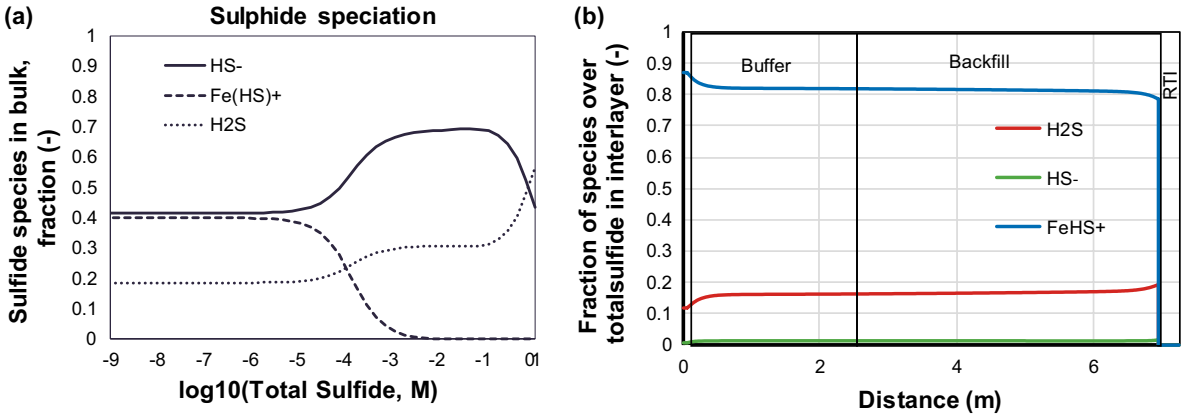

Figure 6-17. *(a) Speciation of sulfide in the bulk porosity (calculation done in Phreeqc using Thermochimie) and (b) results of the hybrid model in terms of longitudinal profiles of sulfide aqueous species in the interlayer water, relative to the total amount of sulfide in the interlayer at 100 kyr.*

Figure 6-18, Figure 6-19 and Table 6-18 present the global production and consumption of sulfide in the system as a function of time, respectively, for the hybrid model and the traditional model. The production of sulfide by the CH_2O path is very similar in both models. The hybrid model predicts a 6.5 % decrease in the amount of sulfide produced. On the other hand, the production of sulfide by H_2, generated in the corrosion process, increased by a factor of 1.74 in the hybrid model after 100 kyr. This is due to the higher corrosion rates in the long term. Higher corrosion rates are obtained in the hybrid model due to the larger transport capacity of sulfide in the hybrid model resulting from the high concentration of the cation $Fe(HS)^+$ in the interlayer water (Figure 6-17).

The canister corrosion is almost doubled in the hybrid model as compared to the traditional model after 100 kyr, see Figure 6-19b and Table 6-18, due to a higher diffusive flux of sulfide in the hybrid model, as described above and displayed in Figure 6-20. It is noted that during the first 1 000 years, sulfide fluxes are lower in the hybrid model. The reason for this is that initially the buffer presents low iron concentrations (see Figure 6-3e), which results in a low $Fe(HS)^+$ fraction.

As there is relatively more sulfide consumption by canister corrosion in the hybrid model, the relative sulfide consumption by mackinawite precipitation decreases slightly (Figure 6-19b and Table 6-18).

Table 6-18. Sulfide budget in the Base Case obtained with a traditional and a hybrid model at 100 000 years: production, consumption, and accumulation. Amount of sulfide in moles, considering a cross-section of 1 m². Percentages are given with respect to total sulfide produced.

Case		Produced sulfide (moles/m²)			Consumed sulfide (moles/m²)				Corrosion depth (µm)
		CH_2O path	H_2 path	Total	Mackinawite	Porewater	Corrosion	Total	
Base Case	TM	3.55	8.21E−03	3.56	3.50 (98.6 %)	1.02E−02 (0.287 %)	4.76E−02 (1.34 %)	3.56	0.675
	HM	3.32	1.43E−02	3.33	3.20 (96.2 %)	2.23E−02 (0.67 %)	8.30E−02 (2.49 %)	3.31	1.18

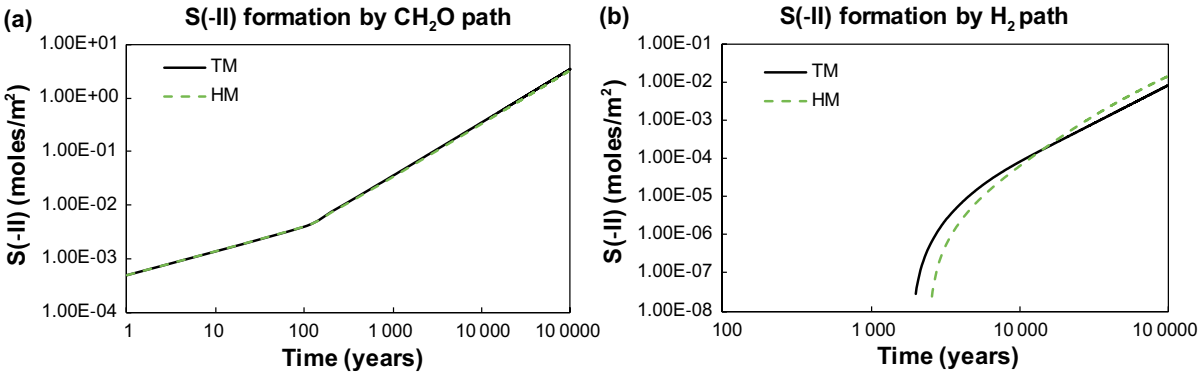

Figure 6-18. *Results of the hybrid model and comparison with the traditional model results in terms of cumulative sulfide global production (in moles, considering a cross-section of 1 m^2) over 100 kyr by microbial-induced sulfate reduction in the RTI domain: (a) CH_2O path and (b) H_2 path.*

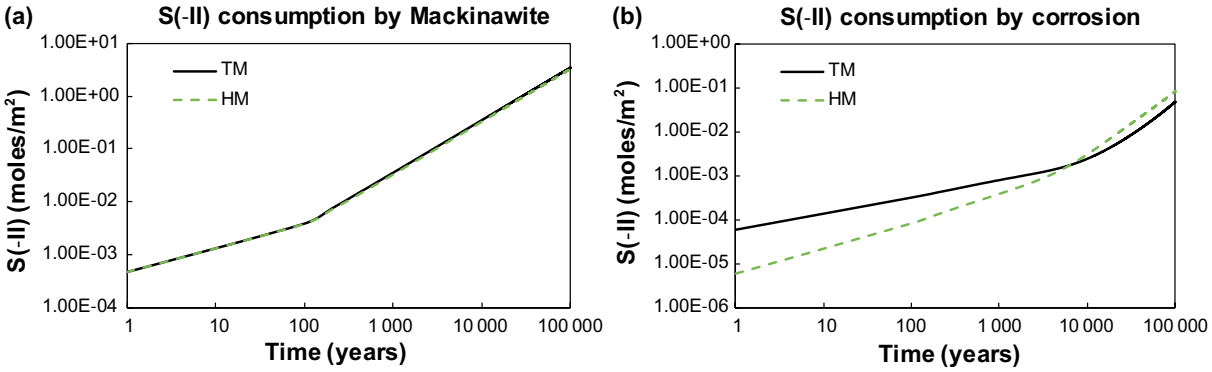

Figure 6-19. *Results of the hybrid model and comparison with the traditional model results in terms of cumulative sulfide global consumption (in moles, considering a cross-section of 1 m^2) over 100 kyr by (a) mackinawite precipitation and (b) corrosion.*

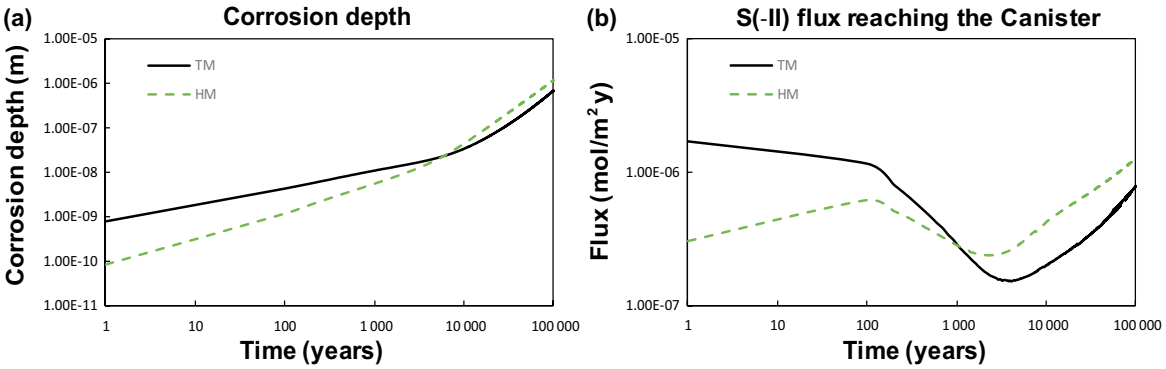

Figure 6-20. *Results of the hybrid model and comparison with the traditional model results in terms of (a) corrosion depth and (b) sulfide flux reaching the canister over 100 kyr.*

7 Variant cases

In this section, a set of sensitivity cases are presented to assess the impact of several processes on the corrosion of the canister. These cases are presented in Table 7-1.

Table 7-1. List and description of sensitivity cases simulated in this work.

Case	Description	Models used
Backfill Density	Backfill density low enough to sustain SRB activity in its entire volume	Traditional and Hybrid
Interface Metals	Interfaces metal corrosion: effect of rock bolts and stretch metal producing H_2 and magnetite	Traditional and Hybrid
Organic Matter	Effect of changing organic matter content in buffer and backfill	Traditional and Hybrid
Fe(II) Minerals	Effect of changing the amount of Fe(II) minerals that can react with sulfide in the buffer and backfill	Traditional and Hybrid

7.1 Backfill Density

In the Base Case model, SRB activity was limited to the RTI domain. This variant case, on the other hand, considers a backfill density that is low enough to sustain SRB activity and thus sulfide production. Sulfate reduction in the backfill follows the same Monod reaction rates as in the RTI given by Equations 6-7 and 6-8. The parameters for these reactions are also the same as for the RTI, except for the biomass concentration. Two subcases of this variant case were simulated using different biomass concentrations in the backfill. Given that the rate is linearly proportional to the biomass concentration, a 'fast case' is simulated that corresponds to $2 \cdot 10^8$ cells/L of biomass, while a 'slow case' corresponds to a value of $1 \cdot 10^5$ cells/L.

7.1.1 Traditional model

Figure 7-1a shows SOM consumption in the two Backfill Density cases (considering the "fast" and "slow" SRB rates), where they are compared to the Base Case. In the "fast" Backfill Density case, the SOM of the backfill is completely consumed in only 40 years, while in the "slow" case this process takes ~100 kyr. The final state of both simulations, however, is very similar: the backfill SOM is completely consumed, and DOM is diffusing from the buffer to the backfill, where it is consumed by the sulfate reduction process. In both simulations, reducing the backfill density causes a much higher SOM consumption as compared to the Base Case.

The sulfate reduction reaction by the CH_2O path taking place in the backfill produces a high amount of sulfide, two orders of magnitude higher than the same reaction in the RTI in the Base Case (see Figure 7-1b and Figure 7-2a). Within 40 years, 315 moles of sulfide are produced by the consumption of organic matter from the backfill. After 100 kyr, sulfide production increases up to 341 moles due to the contribution of organic matter from the buffer (Figure 7-2a). This is much more than the 3.55 moles of sulfide produced in the Base Case. In turn, mackinawite precipitation in the entire backfill is significant in these variant cases (Figure 7-1c). Due to the difference in biomass concentration, the production of sulfide is faster initially in the fast Backfill Density case (Figure 7-2a). After 40 years, however, when the backfill SOM is exhausted, this process is slowed down as it is limited by the in-diffusion of DOM from the buffer. The result is that at 100 kyr both variant cases present similar values of total sulfide produced by the CH_2O path. The increase in sulfate reduction rates in the cases with low backfill density causes a pH decrease from 7.2 to 5.5 (see Figure 7-1d) which increases sulfide solubility under mackinawite equilibrium by almost two orders of magnitude (Figure 7-1b).

In the Backfill Density cases, similar to the Base Case, most of the sulfide precipitates as mackinawite (see Table 7-1), but in the whole backfill domain (Figure 7-1c), while in the Base Case precipitation is limited to the interface between backfill and RTI (see Figure 6-4a).

Due to the increase in sulfide production, corrosion of the canister is significantly increased in both variant cases and, as a consequence, also the sulfide production by the H_2 path (see Figure 7-2d and b). The corrosion depth at 100 kyr obtained with the fast case is higher than that of the slow case, but Figure 7-2d indicates that this tendency can change in the next 10 kyr, as the corrosion rate in the slow case is faster by the end of the simulation.

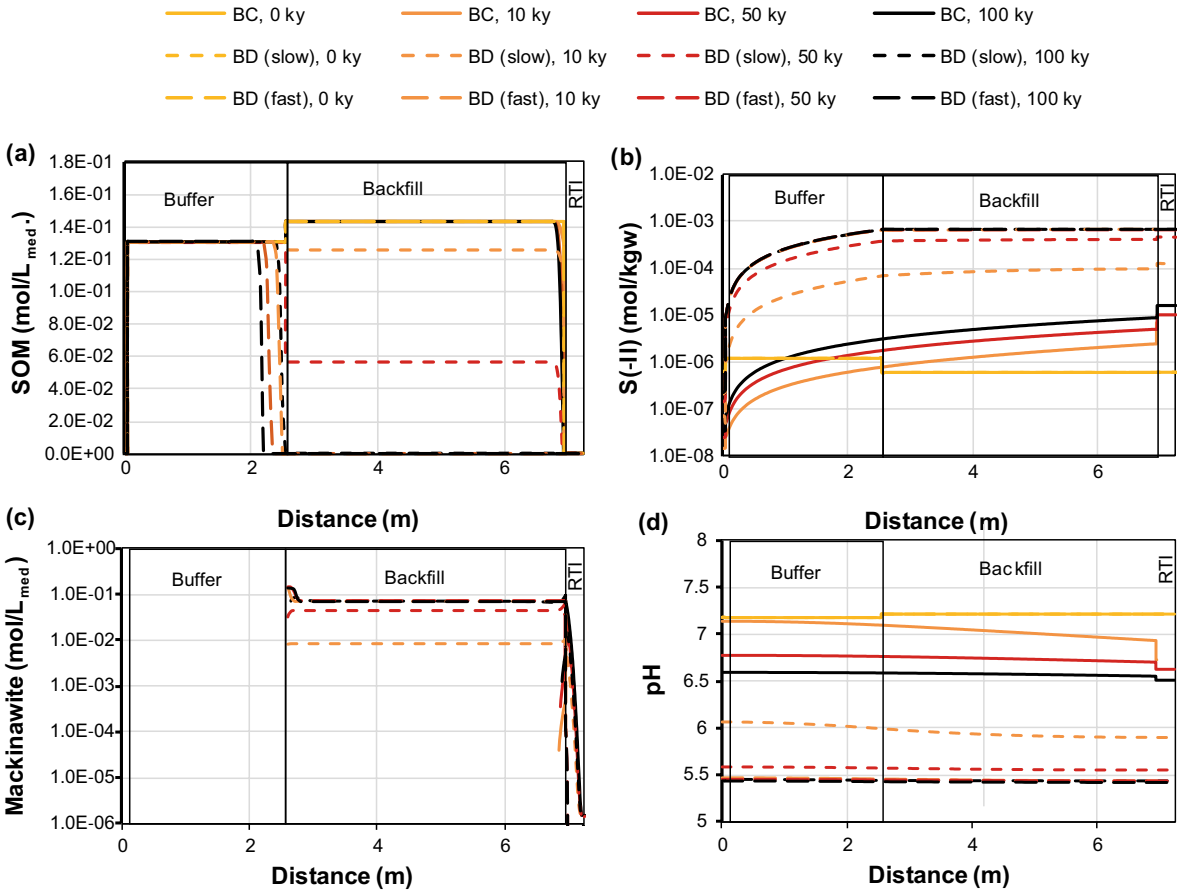

Figure 7-1. *Longitudinal profiles of (a) solid organic matter (SOM), (b) total sulfide concentration and (c) mackinawite for different times in the traditional model Backfill Density (BD) cases as compared to the Base Case (BC). Aqueous concentrations are given in mol per kg of water while mineral concentrations are given in mol per litre of medium.*

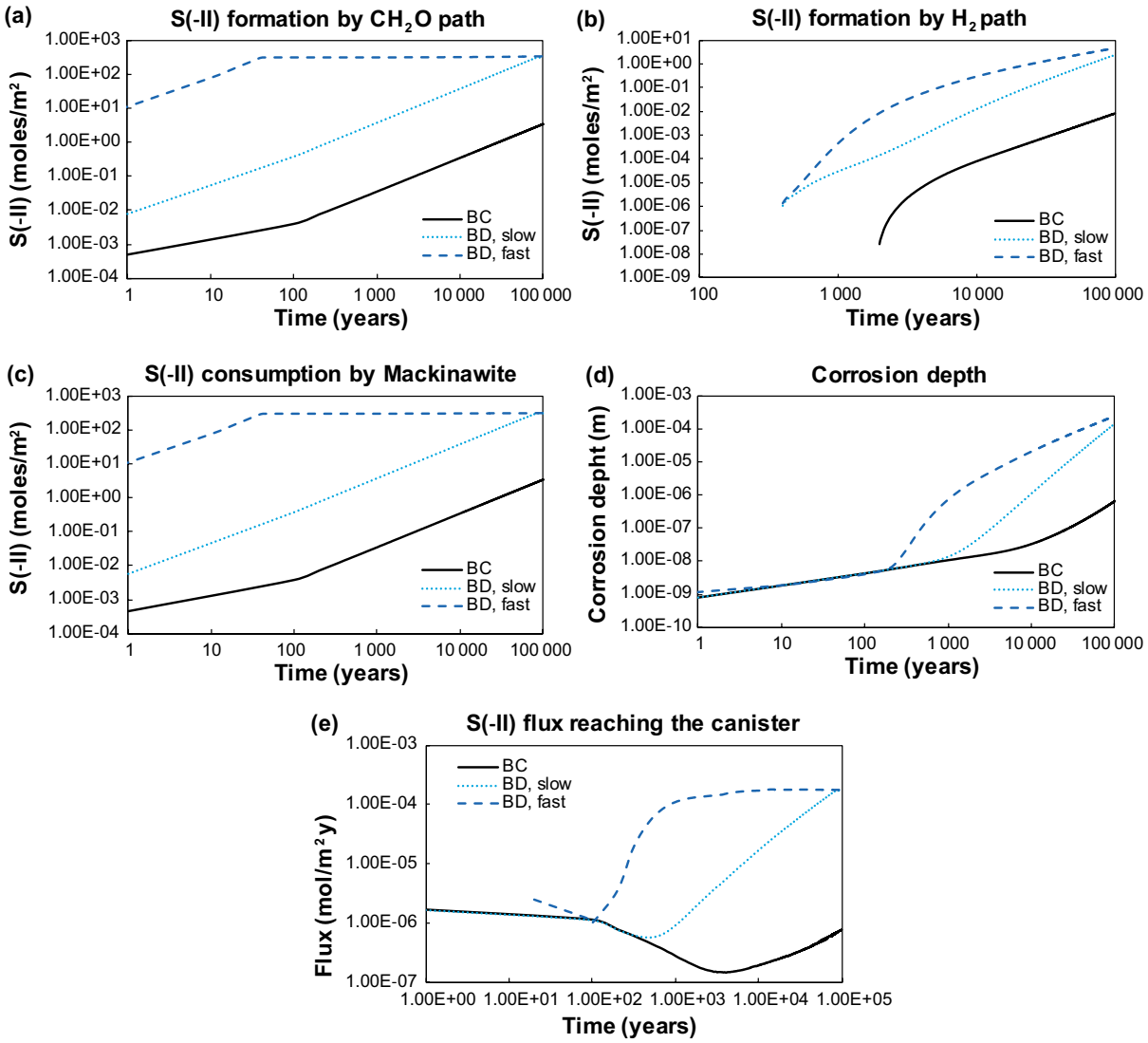

Figure 7-2. *Comparison of the traditional model Backfill Density variant case results (corrosion depth, S(-II) budget plots): cumulative sulfide generation (in moles/m^2) by (a) CH_2O path and (b) H_2 path, (c) cumulative sulfide consumption by mackinawite precipitation (in moles/m^2), (d) corrosion depth (m), and (e) sulfide flux reaching the canister (moles/m^2 year).*

7.1.2 Hybrid model

In this section, the hybrid model results of the Backfill Density cases are compared to the traditional model results.

Figure 7-4 and Figure 7-5 present the results of the slow and fast Backfill Density cases, respectively. These figures and Table 7-1 show that, in general, the traditional and hybrid models of the Backfill Density cases do not differ much, especially in the longer term.

Sulfide formation via the CH_2O path is slightly lower in the hybrid models, for the same reason as in the Base Case: there is 10 % less porosity available for SOM diffusion in the hybrid models. This should not have an effect at the beginning of the simulations, as there is organic matter present in the backfill itself. Once this organic matter in the backfill has been consumed completely, however, the reaction is limited by in-diffusion from the buffer.

As there is less sulfide production, there is also less mackinawite precipitation in the hybrid models (see Figure 7-4c, Figure 7-5c and Table 7-1).

When it comes to sulfide transport through bentonite, the use of a hybrid model results in two competing effects: a reduction of porosity available for diffusion reduces the effective diffusion coefficient, whereas the high concentration of cations in the interlayer causes a larger sulfide gradient. In the Base Case, the hybrid model resulted in much higher sulfide concentration gradients through the buffer and backfill than the traditional model (Figure 6-15) which caused higher sulfide fluxes into the canister in the long term (Figure 6-20b). In the Backfill Density cases, on the other hand, using a hybrid model increases sulfide concentration gradients to a much lesser extent (Figure 7-3). The overall effect of these concentration gradients and a reduced effective diffusion coefficient are slightly smaller sulfide fluxes reaching the canister in the hybrid models (Figure 7-4e and Figure 7-5e). Smaller sulfide fluxes in turn, imply less canister corrosion, less hydrogen formation and less sulfate reduction by the H_2 path (see Figure 7-4, Figure 7-5 and Table 7-1).

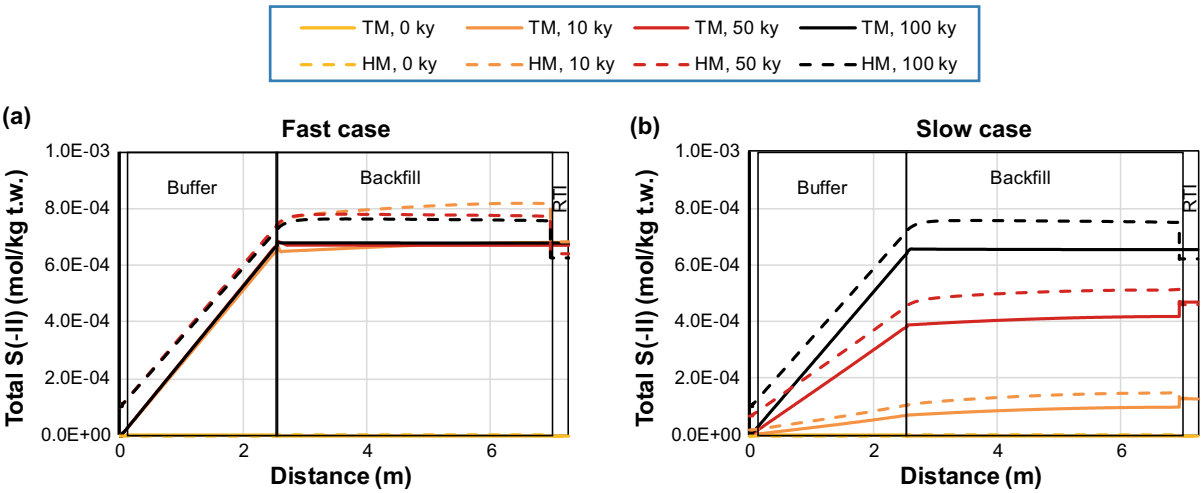

Figure 7-3. *Results of the hybrid model and comparison with the traditional model results for the fast (a) and slow (b) Backfill Density cases in terms of longitudinal profiles of total sulfide concentrations in total water (mol/kg t.w., i.e. total water) at different times: 0, 10, 50, and 100 kyr.*

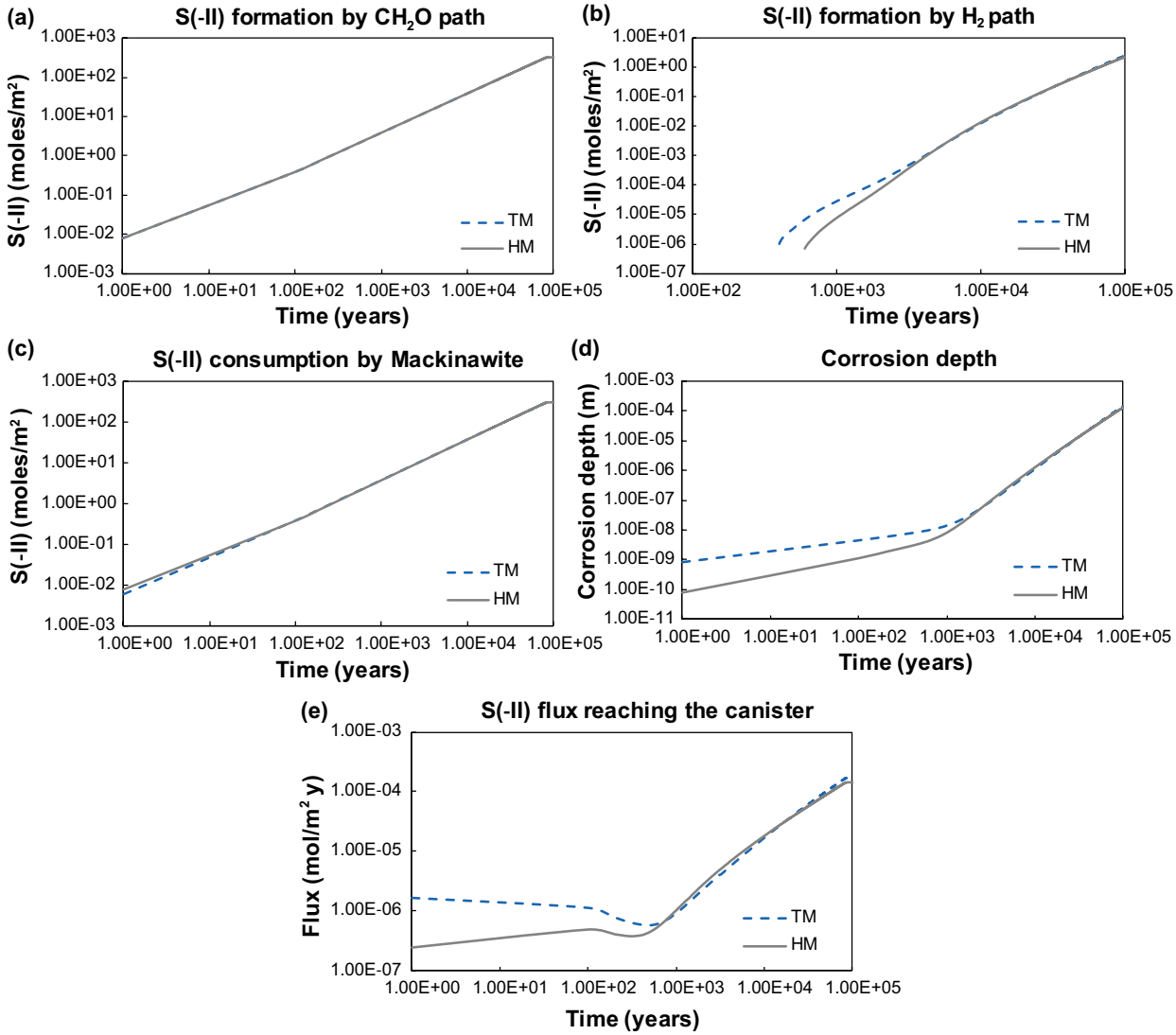

Figure 7-4. *Comparison of slow Backfill Density case results: Traditional vs. hybrid model (corrosion depth, S(-II) budget plots): cumulative sulfide generation (in moles/m^2) by (a) CH_2O path and (b) H_2 path, (c) sulfide consumption by mackinawite precipitation (in moles/m^2), (d) corrosion depth (m), and (e) sulfide flux reaching the canister (moles/m^2 year).*

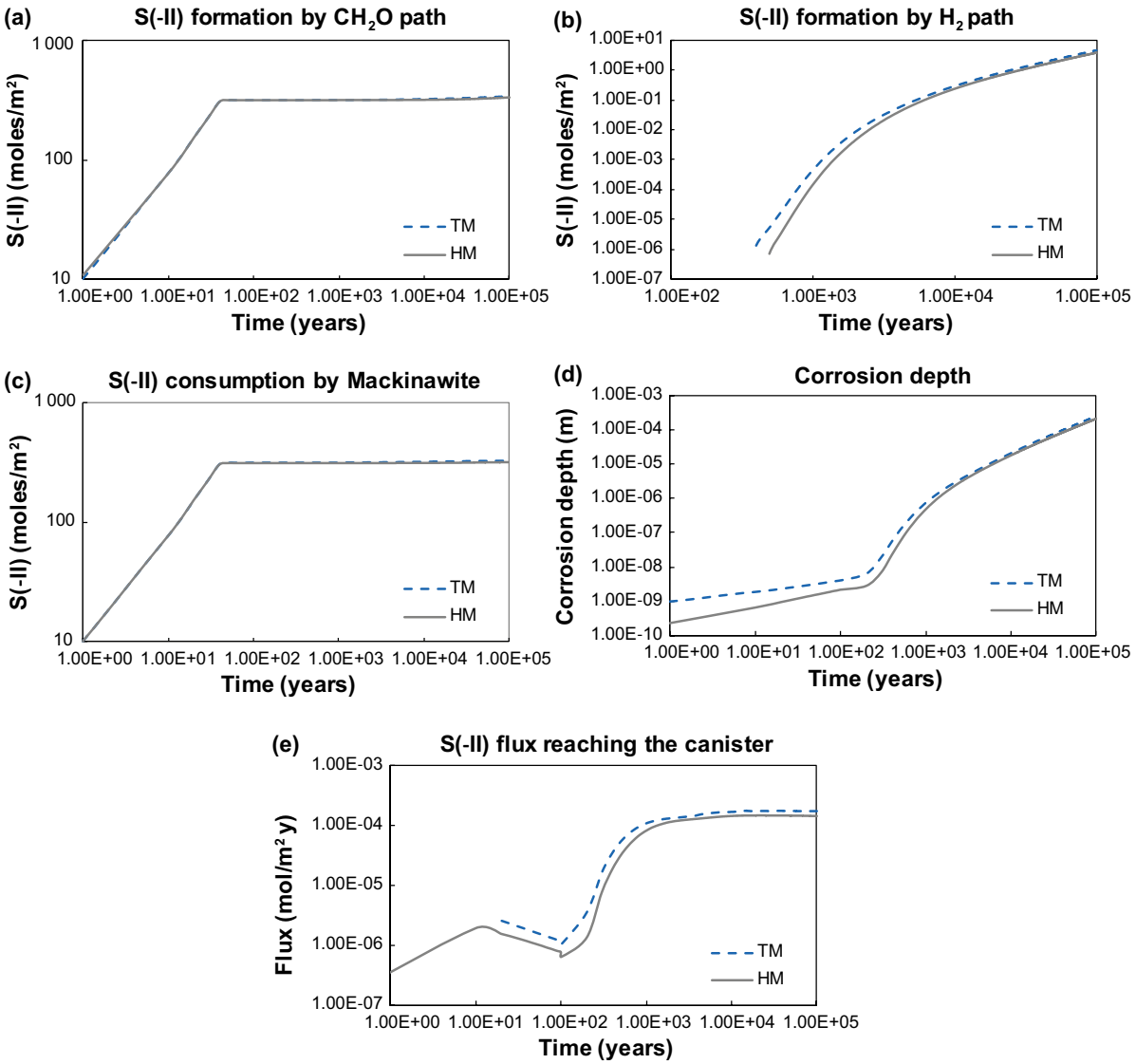

Figure 7-5. *Comparison of fast Backfill Density case results: Traditional vs. hybrid model (corrosion depth, S(-II) budget plots): cumulative sulfide generation (in moles/m^2) by (a) CH_2O path and (b) H_2 path, (c) cumulative sulfide consumption by mackinawite precipitation (in moles/m^2), (d) corrosion depth (m), and (e) sulfide flux reaching the canister (moles/m^2 year).*

Table 7-2. Produced and consumed sulfide at 100 kyr in the Backfill Density cases and the Base Cases. Percentages are given with respect to total sulfide produced.

Case	Model	Produced sulfide (moles/m²)			Consumed sulfide (moles/m²)				Corrosion Depth (µm)
		CH_2O path	H_2 path	Total	Mackinawite	Porewater	Corrosion	Total	
Base Case	TM	3.55	0.00821	3.56	3.50 (98.6 %)	0.0102 (0.287 %)	0.0476 (1.34 %)	3.56	0.675
	HM	3.32	0.0143	3.33	3.20 (96.2 %)	0.0223 (0.67 %)	0.0830 (2.49 %)	3.31	1.18
Backfill Density (fast)	TM	341	4.36	345	326 (94.3 %)	1.64 (0.48 %)	17.6 (5.11 %)	345	250
	HM	333	3.75	337	319 (94.7 %)	1.89 (0.56 %)	15.4 (4.57 %)	336	218
Backfill Density (slow)	TM	320	2.38	322	311 (96.4 %)	1.59 (0.49 %)	9.78 (3.03 %)	322	139
	HM	319	2.17	321	310 (96.5 %)	1.87 (0.58 %)	9.05 (2.82 %)	320	128

7.2 Interface Metals

The concept of the KBS-3V repository considers supporting the deposition tunnels with rock bolts and stretch metal. The objective of performing this variant case is to evaluate the effect of corroding steel from rock bolts and stretch metal in the rock-backfill interface on sulfide sinks and sources. In the model, anaerobic steel corrosion leads to the production of hydrogen (H_2) and magnetite.

This variant case includes an additional domain, the Backfill Steel Interface, or BSI, which represents the steel embedded in the backfill material. The domain, located next to the RTI, is assumed to have a thickness of 0.05 m and has the same properties as the backfill, with the difference that steel is added. Steel is assumed to be regularly distributed in the walls and ceiling with a mass of 14 kg/m tunnel. The steel concentration in the BSI is, then, 25.93 kg/m^3 BSI medium using a combined perimeter of walls and ceiling of 10.8 m (see Hansen et al. 2010, Figure 2-1, reactors OL 1-2), and a BSI thickness of 0.05 m.

Steel corrosion follows the reaction:

$$Fe(s) + 2H_2O \rightarrow Fe^{+2} + 2\,OH^{-} + H_2 \qquad (7\text{-}1)$$

The corrosion rate is assumed constant and equal to 2.8 µm/y. For metal wires with a circular cross-section with 3 mm diameter this is equivalent to $6.39 \cdot 10^{-11}$ mol/(s·kg$_w$). Thus, the metal will be fully corroded after only 536 years. In this case, the time step used during the first 1 000 years of simulation is 0.1 years, while for the rest of the time it is maintained at 1 year. Magnetite, a product of steel corrosion, is added to the model as a secondary phase and can precipitate and dissolve under thermodynamic equilibrium following the reaction:

$$2\,Fe^{+3} + Fe^{+2} - 8\,H^{+} + 4\,H_2O \leftrightarrow Fe_3O_4(s) \qquad (7\text{-}2)$$

The H_2 produced by steel corrosion is considered in the model to be decoupled from aqueous chemistry and can only be consumed by SRB in the RTI to produce sulfide.

7.2.1 Traditional model

The interface metals present in the BSI domain are fully corroded after 536 years, as shown in Figure 7-6a. This corrosion produces a significant amount of H_2 (Figure 7-6b). Its concentration reaches a maximum of 0.022 M after 536 years at the BSI and then decreases with time. The maximum concentration is still lower than the solubility of H_2 at 5 MPa and 25 ºC (~ 0.0385 M). Therefore, no gas phase is expected to form in these conditions. The concentration of hydrogen

along the modelled domain is shown in Figure 7-7 at different times. During the first 500 years, hydrogen generation at the BSI (right boundary in the figure) leads to a constant increase in concentration at this side. Thereafter, its concentration decreases at the BSI as hydrogen diffuses towards the RTI and the canister. Hydrogen accumulates in the buffer and backfill until it is slowly consumed in the RTI, which has a limited transport capacity. This is due to the fact that (1) the diffusion across the bentonite barriers is much faster than towards the RTI, and (2) that the much lower porosity of the RTI (0.01 vs. 0.43 in the backfill) leads to very small mass loss in the backfill for large changes in concentrations in the RTI. This initial hydrogen accumulation in the buffer and backfill and slow consumption by SRB activity in the RTI is the reason why after 5 000 years the concentration gradient of hydrogen is clearly from the canister towards the RTI.

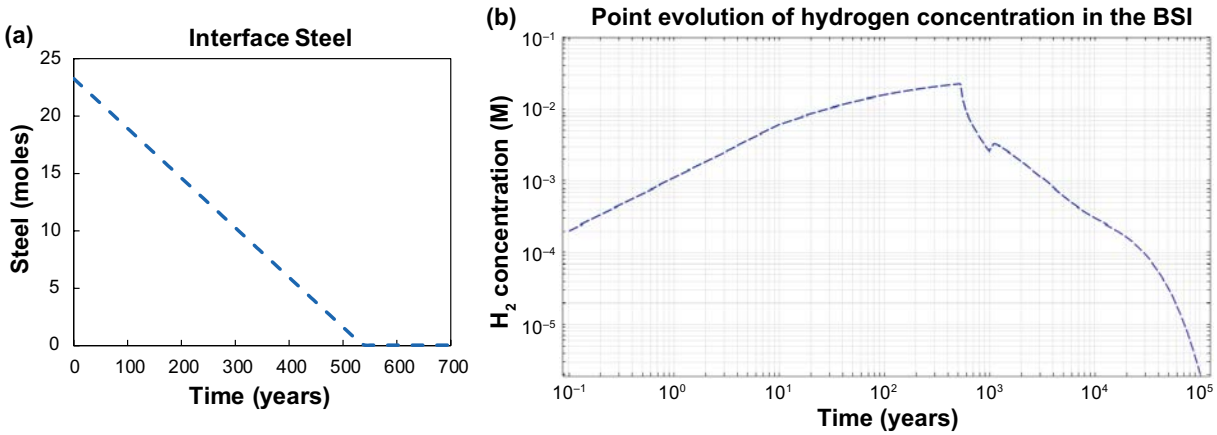

Figure 7-6. *(a) Steel consumption by corrosion in the BSI domain as a function of time (in moles, considering a cross-section of 1 m^2) and (b) concentration of H_2 in the mid-point of the BSI domain in the Interface Metals simulation.*

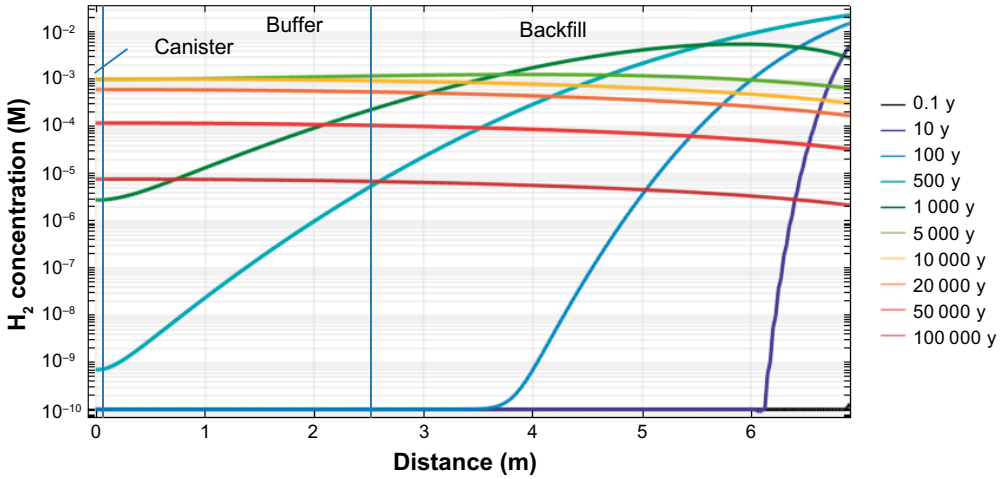

Figure 7-7. *Concentration of H_2 (in M) in the longitudinal profile of the modelled domain (except the RTI, where H_2 tends to 0) in the Interface Metals simulation at different times: 0.1, 10, 100, 500, 1 000, 5 000, 20 000, 50 000, and 100 000 years.*

As a result of the steel corrosion, sulfide production from the H_2 path increases by more than 2 orders of magnitude as compared to the Base Case (see Figure 7-8b and Table 7-3). However, it is noted that this reduction rate decreases significantly after ~1 000 years due to a gradual decrease of hydrogen concentrations (Figure 7-7). The cumulative sulfide production by the CH_2O path is initially higher in the Interface Metals case, probably due to the use of smaller time steps during the first 1 000 years. However, cumulative sulfide production is similar in both cases in the long term (2 % higher in the Interface Metals case). The total amount of produced sulfide after 100 kyr increases by a factor of 2.7, mainly due to the hydrogen generated by steel corrosion.

Iron is released into the pore solution of the BSI by steel corrosion and, to a lesser extent, by siderite dissolution (Figure 7-9c). This iron reprecipitates as magnetite (Figure 7-9a) and mackinawite (Figure 7-9b). Figure 7-10a shows these processes in more detail. Magnetite reaches its maximum concentration at full corrosion of the steel. Thereafter, it slowly dissolves at the expense of siderite reprecipitation and more mackinawite formation due to in-diffusion of sulfide from the RTI.

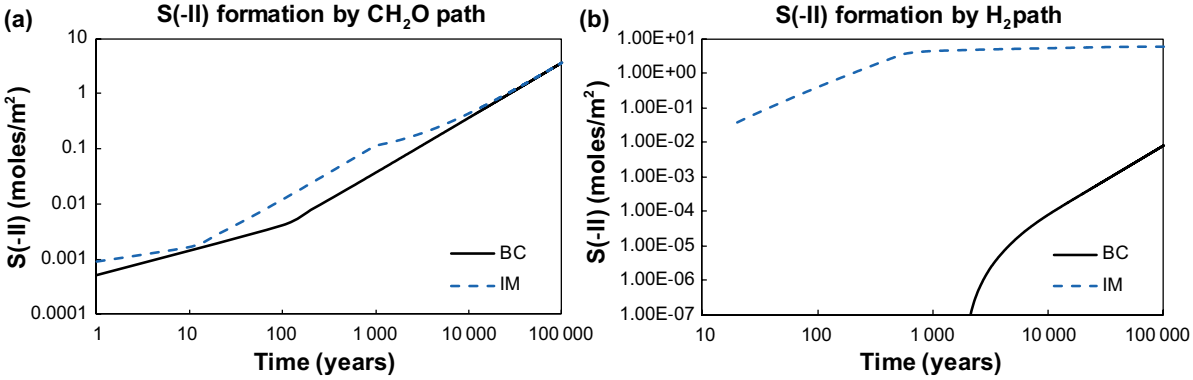

Figure 7-8. Cumulative sulfide global production (in moles, considering a cross section of 1 m^2) over 100 kyr by microbial-induced sulfate reduction in the RTI domain in the Interface Metals (IM) and Base Case (BC) traditional models: (a) CH_2O path and (b) H_2 path.

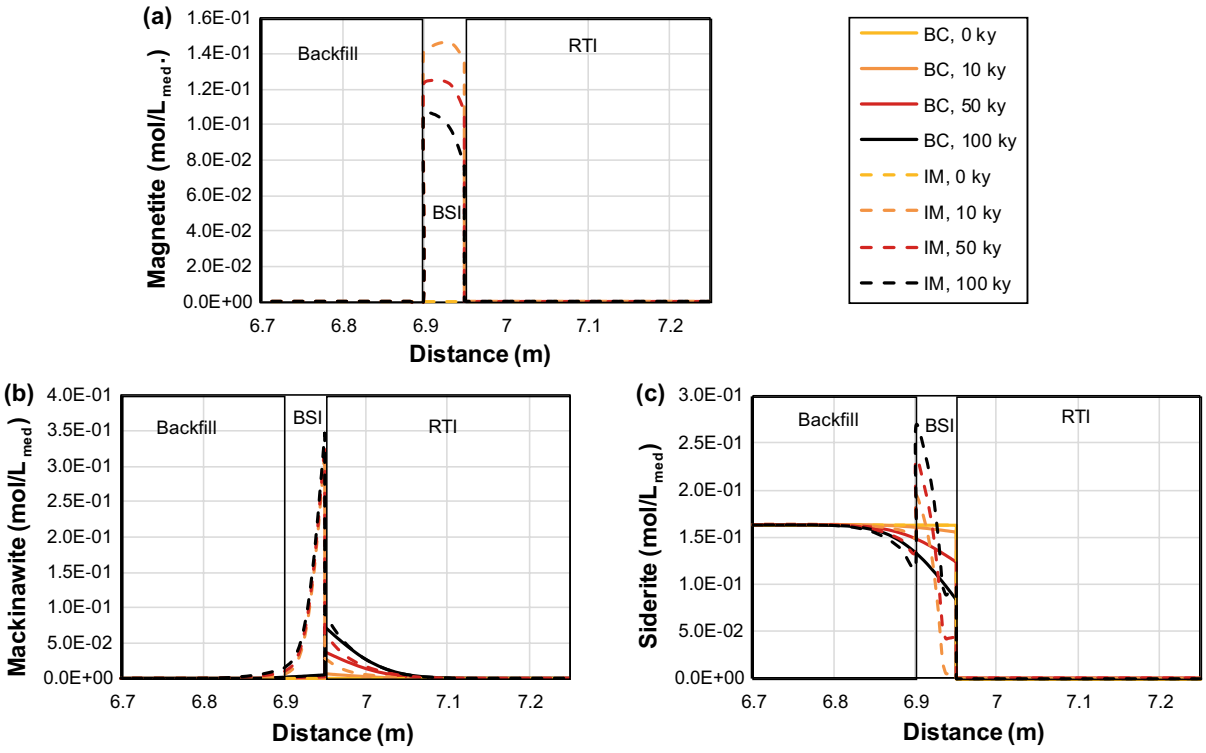

Figure 7-9. Longitudinal profiles of (a) magnetite, (b) mackinawite and (c) siderite concentrations, in mol per litre of medium, in the BSI domain for different times in the Interface Metals (IM) and Base Case (BC) traditional models.

In the present model setup, hydrogen is also produced by magnetite precipitation in the BSI. This leads to an increase in the pH of the system as a result of the redox control in Phreeqc (which limits the stability of water by the reduction of water to hydrogen). This is shown in Figure 7-10b and Figure 7-11b, where a maximum pH value of 8.5 is reached right after full corrosion of the steel (between 500 and 600 years). Batch simulations performed with PhreeqC indicate that this increase in pH is buffered by magnetite equilibrium in the BSI during the whole simulation (Figure 7-9a and Figure 7-10a).

The increase in pH in the Interface Metals case results to be a key process by which the equilibrium between mackinawite and sulfide is shifted towards much lower concentrations of sulfide than the Base Case. This is similar to what is explained in Section 6.3.4 (Figure 6-11). The result is a much lower sulfide concentration in the backfill next to the RTI and thus lower concentration gradients towards the canister, as shown in Figure 7-11a.

In terms of canister copper corrosion, the effect of adding steel to the system near the RTI is a quite significant reduction in the corrosion depth compared to the Base Case (96 % reduction after 100 kyr, see Figure 7-12c and Table 7-3).

Figure 7-12 (a and b) shows the global consumption of sulfide by mackinawite formation and corrosion as a function of time. Compared to the Base Case, a much larger amount of mackinawite forms in this case, which also forms much more rapidly. On the other hand, sulfide consumption by copper corrosion is naturally reduced compared to the Base Case.

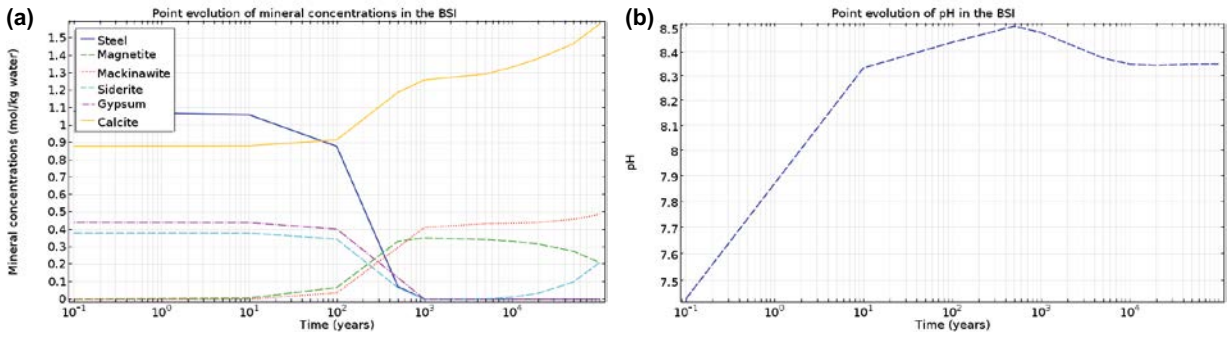

Figure 7-10. *Time evolution of (a) mineral concentrations (mol/kg$_{water}$) and (b) pH in the mid-point of the BSI domain in the Interface Metals simulation.*

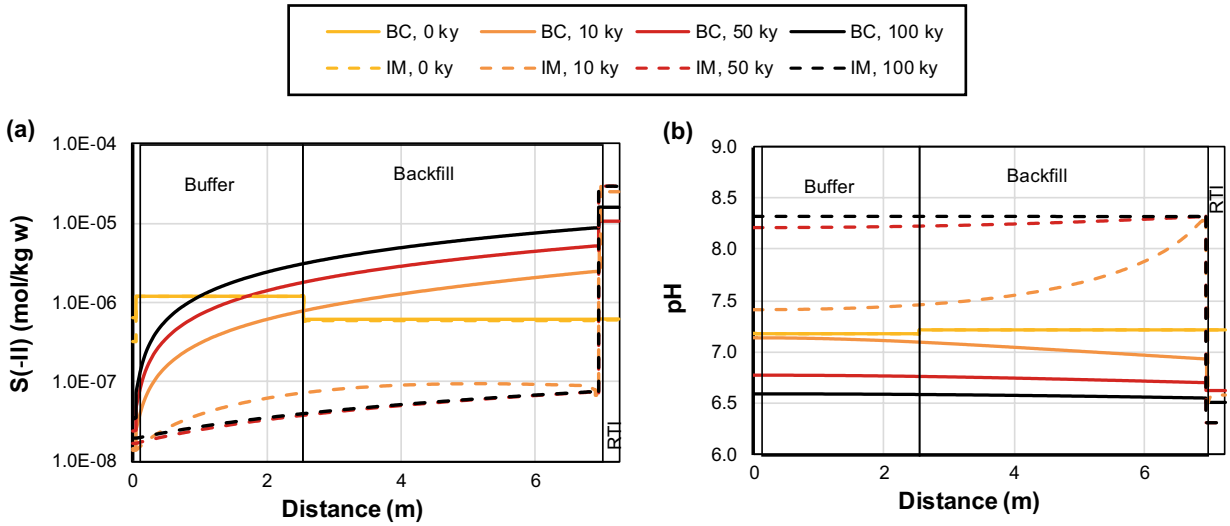

Figure 7-11. *Longitudinal profiles of (a) sulfide concentration and (b) pH for different times in the Interface Metals (IM) and Base Case (BC) traditional models.*

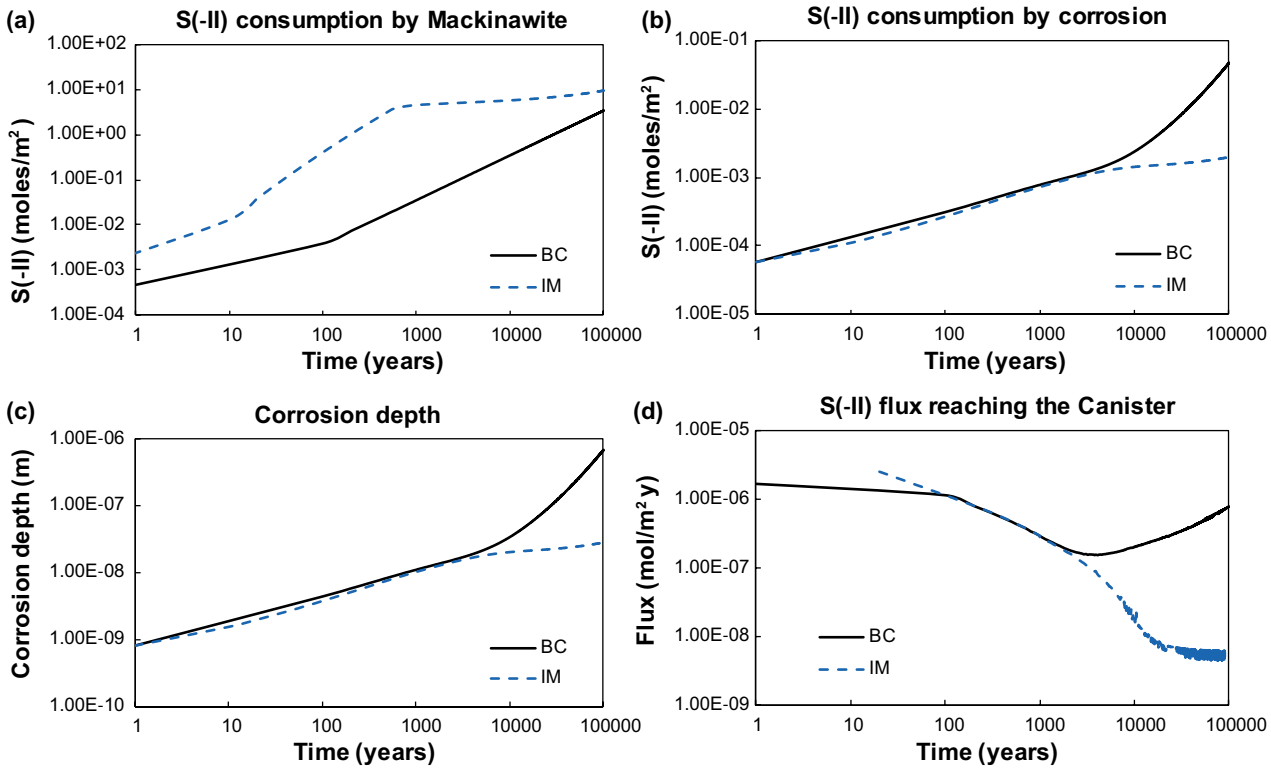

Figure 7-12. *Cumulative sulfide consumption by (a) mackinawite precipitation, and (b) canister corrosion (in moles, considering a cross section of 1 m^2), (c) canister corrosion depth and (d) sulfide flux reaching the canister over 100 kyr in the Interface Metals (IM) and Base Case (BC) traditional models.*

7.2.2 Effect of surface complexation

It has been concluded above that pH variations have a significant effect on sulfide transport and corrosion of the canister in this sensitivity case. As discussed in Section 6.3.4, surface complexation reactions could buffer the pH to some extent. Therefore, this sensitivity case was tested with the same surface complexation model as the Base Case, see Section 6.3.4.

Longitudinal profiles of pH and sulfide concentration of the Interface Metals case with and without surface complexation reactions are compared in Figure 7-13. In the case with surface complexation, the increase in pH is buffered by protonation/deprotonation reactions in the backfill and buffer domains. At the backfill-RTI interface, however, pH is similar in both cases.

Even though the effect of surface complexation on pH is significant away from the BSI, the global effect on sulfide concentration and transport (Figure 7-13b) and canister corrosion (Figure 7-14) is small. The increase in canister corrosion is only of 7 % (see Table 7-3).

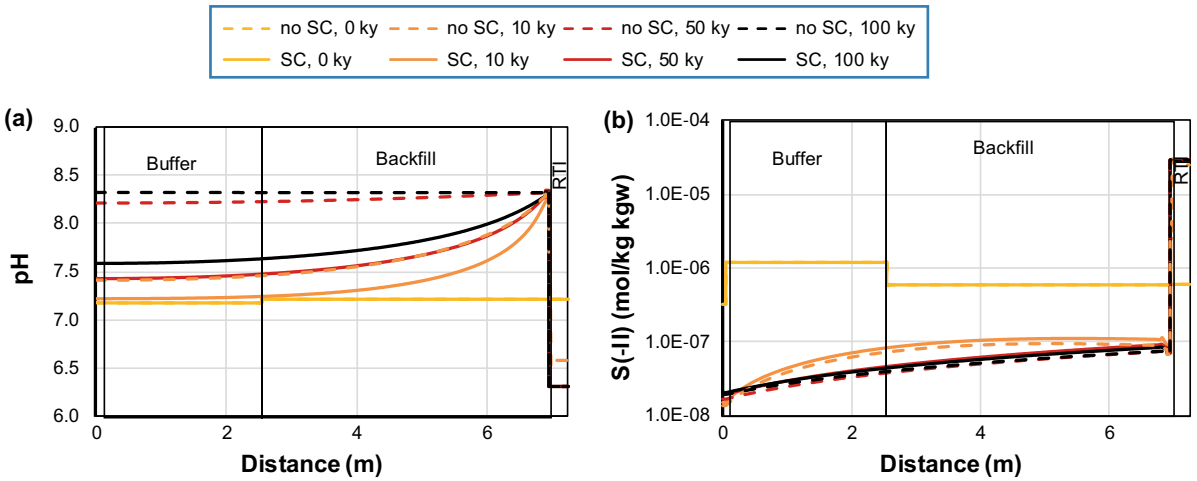

Figure 7-13. *Longitudinal profiles of (a) pH and (b) sulfide concentration for different times in the Interface Metals case with (SC) and without surface complextation reactions (no SC).*

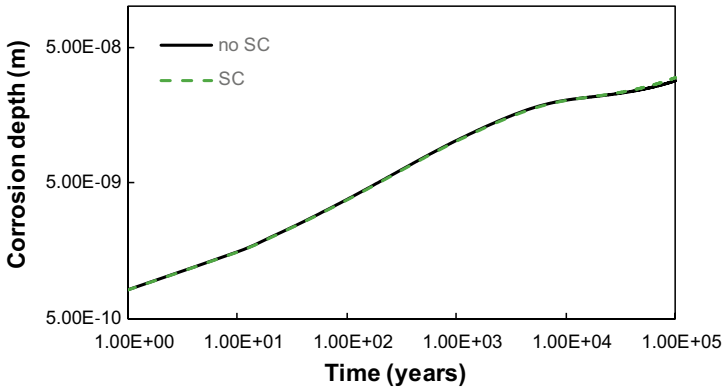

Figure 7-14. *Canister corrosion depth (in m) over 100 kyr in the Interface Metals model with (SC) and without surface complextation reactions (no SC).*

7.2.3 Hybrid model

The Interface Metals variant case was also simulated with the hybrid model. In this section, the hybrid model is compared to the Interface Metals traditional model without surface complexation.

Sulfide production by the CH_2O path (see Figure 7-15a and Table 7-3) is slightly reduced in the hybrid model due to a limited DOM transport, as reported for the Base Case (Section 6.4.2). Sulfide production in the RTI via the H_2 path (Figure 7-15b and Table 7-3) is also slightly lower in the hybrid model, due to the retardation effect by bulk porosity for hydrogen diffusion towards the RTI. As explained in Section 7.2.1, the hydrogen produced in the BSI due to steel corrosion first accumulates in the buffer and backfill. This hydrogen then diffuses towards the RTI where it is consumed (see Figure 7-7 and Figure 7-16).

The overall sulfide production is thus lower with the hybrid model. Still, canister corrosion in the long term is larger than the result obtained with the traditional model (Figure 7-15d,e). This is due to an increase in total sulfide concentrations (Figure 7-17b) and a reduction in mackinawite formation in the hybrid model (Figure 7-15c and Table 7-3). On the one hand, a lower pH in the buffer and backfill of the HM (Figure 7-17b) results in higher sulfide concentrations in equilibrium with mackinawite in the bulk porewater (Figure 7-17a). On the other hand, the hybrid model results in higher sulfide concentrations in the interlayer water due to the contribution of the cation $Fe(HS)^+$. The overall result is a larger sulfide flux reaching the canister in the long term (Figure 7-15e) and thus higher canister corrosion depths in the hybrid model (Figure 7-15d, Table 7-3): after 100 kyr of simulation, the corrosion depth is four times larger in the hybrid model.

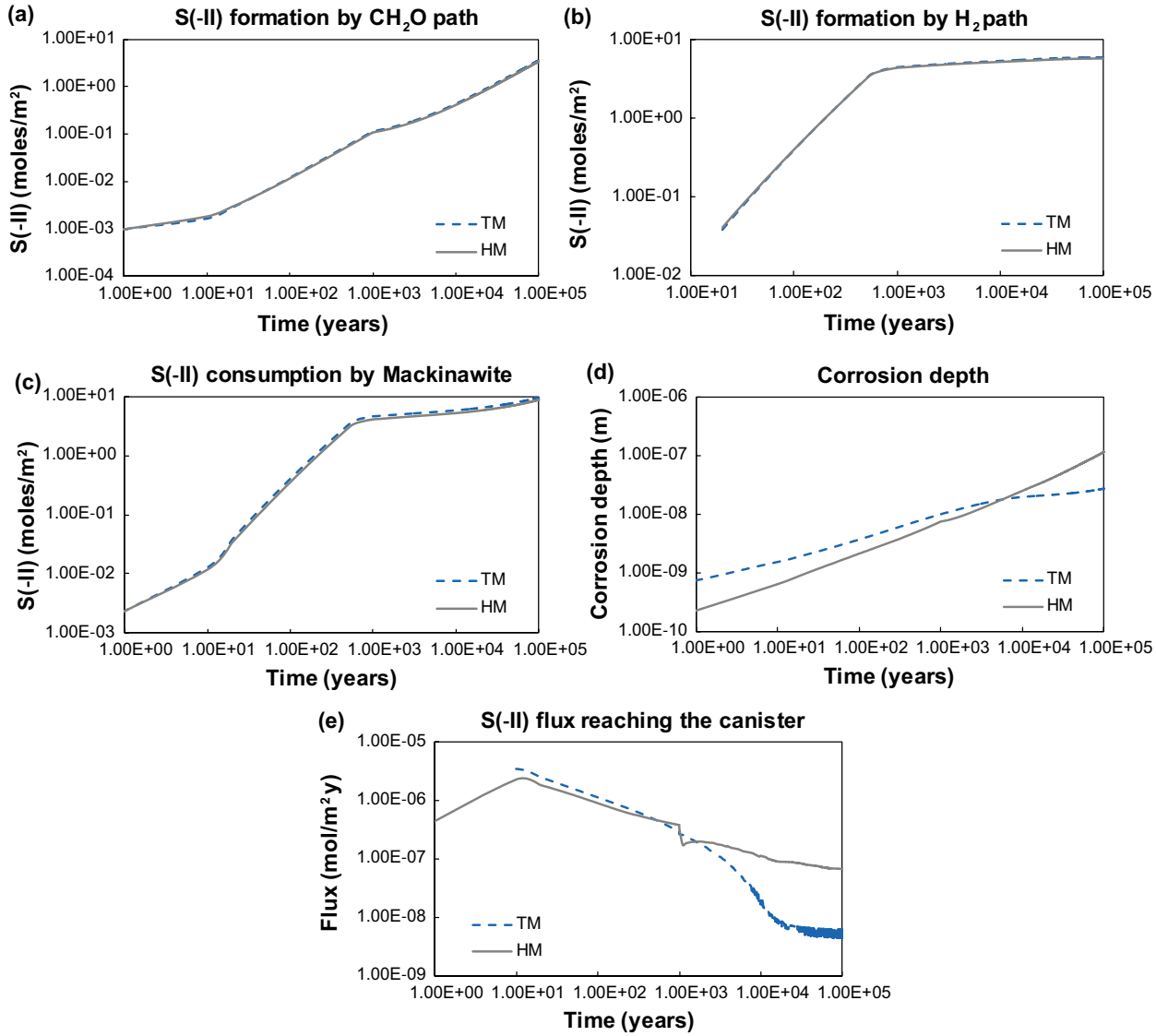

Figure 7-15. *Comparison of Interface Metals variant case results. Traditional vs. hybrid model corrosion depth and S(-II) budget plots: cumulative sulfide generation (in moles/m^2) by (a) CH_2O path and (b) H_2 path, (c) cumulative sulfide consumption by mackinawite precipitation (in moles/m^2), (d) corrosion depth (m), and (e) sulfide flux reaching the canister (moles/m^2 year).*

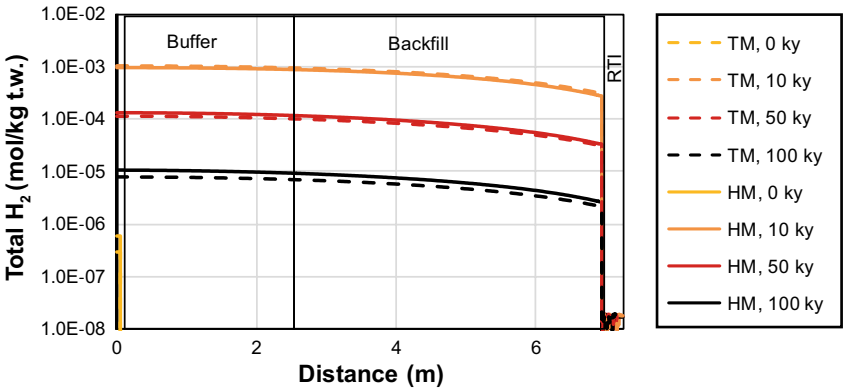

Figure 7-16. *Longitudinal profiles of total hydrogen concentration, in moles per kg of total water, for different times in the traditional and hybrid Interface Metals models.*

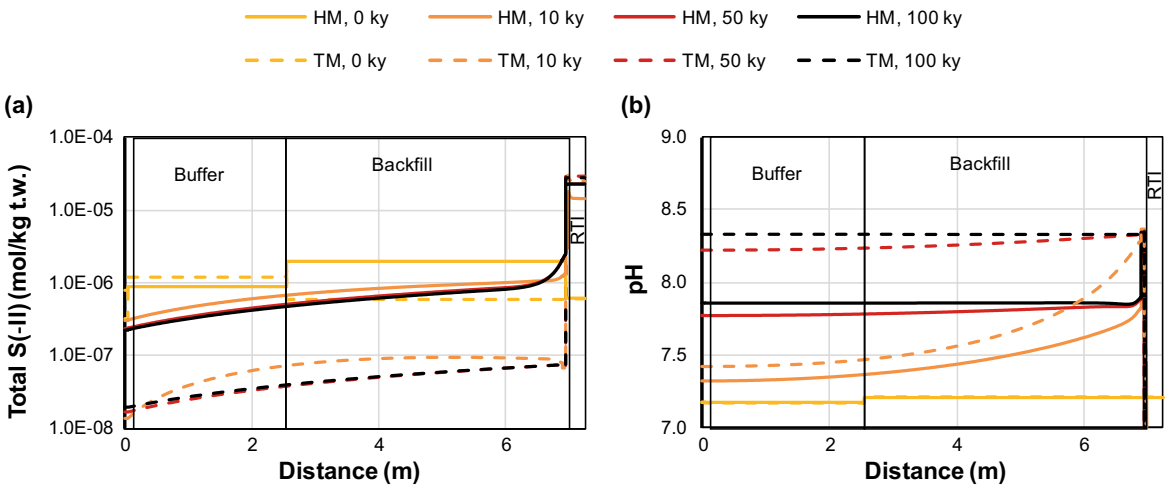

Figure 7-17. *Longitudinal profiles of (a) total sulfide concentration (mol/litre of total water) and (b) pH for different times in the traditional and hybrid Interface Metals models.*

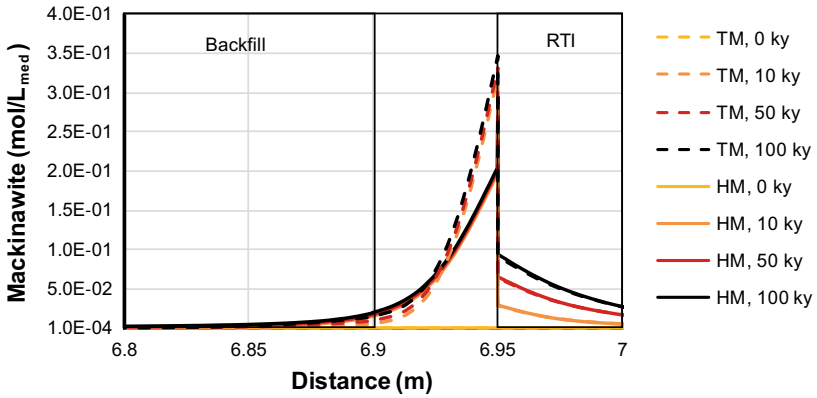

Figure 7-18. *Longitudinal profiles of mackinawite concentration (mol/litre medium) for different times in the traditional and hybrid Interface Metals models.*

Table 7-3. Sulfide budget in the Base Case and Interface Metals simulations with traditional model without (TM) and with (TM (SC)) surface complexation, and the hybrid model (HM) at 100 kyr: production, consumption, and accumulation. Amount of sulfide in moles, considering a cross-section of 1 m^2. Percentages are given with respect to total sulfide produced.

Case	Model	Produced sulfide (moles/m^2)			Consumed sulfide (moles/m^2)				Corrosion Depth (μm)
		CH_2O path	H_2 path	Total	Mackinawite	Porewater	Corrosion	Total	
Base Case	**TM**	3.55	8.21E−03	3.56	3.50 (98.6 %)	1.02E−02 (0.287 %)	4.76E−02 (1.34 %)	3.56	0.675
	TM (SC)	3.55	5.62E−03	3.56	3.52 (99.0 %)	5.49E−03 (0.15 %)	3.18E−02 (0.89 %)	3.56	0.451
	HM	3.32	1.43E−02	3.33	3.20 (96.2 %)	2.23E−02 (0.67 %)	8.30E−02 (2.49 %)	3.31	1.18
Interface Metals	**TM**	3.63	5.89	9.52	9.56 (100 %)	−2.21E−03 (−2.32E−02 %)	1.98E−03 (2.08E−02 %)	9.56	2.81E−02
	TM (SC)	3.63	5.89	9.52	9.56 (100 %)	−2.19E−03 (−2.3E−02 %)	2.13E−03 (2.32E−02 %)	9.56	3.02E−02
	HM	3.40	5.82	9.21	8.69 (94.3 %)	2.76E−03 (3.0E−02 %)	8.46E−03 (9.18E−02 %)	8.69	0.12

7.3 Organic Matter

The Organic Matter sensitivity case consists of varying the content of solid organic carbon (SOM) available for sulfate reduction in the buffer and backfill. In the Base Case, solid organic matter (SOM) is largely in excess after 100 kyr and increasing its initial amount would not have any effect on the system. Thus, the opposite case was tested, reducing the initial amount of solid organic matter by a factor of 10. The dissolved organic matter (DOM) in equilibrium with the SOM is the same as the Base Case. Note that this sensitivity case is only simulated with the traditional model given that the use of a hybrid model is not expected to have a large effect on DOM (a neutral species) transport.

Figure 7-19 displays the evolution of SOM in the present sensitivity case and in the Base Case. Reducing the initial amount of solid organic matter in the backfill and buffer causes a faster depletion of SOM at the interface between backfill and RTI. This means that the dissolved organic matter needs to diffuse from the SOM dissolution front to the interface with the RTI, thus slightly limiting the sulfate reduction rate at the latter (see Figure 7-20a and Table 7-4).

Due to the lower sulfide production, there is proportionally less mackinawite precipitation (Figure 7-20c), sulfide flux reaching the canister (Figure 7-20e), canister corrosion (Figure 7-20d) and hydrogen formation (Figure 7-20b), see also Table 7-4. However, the effect is very small: canister corrosion, for example, is reduced by only 4 % (Table 7-4).

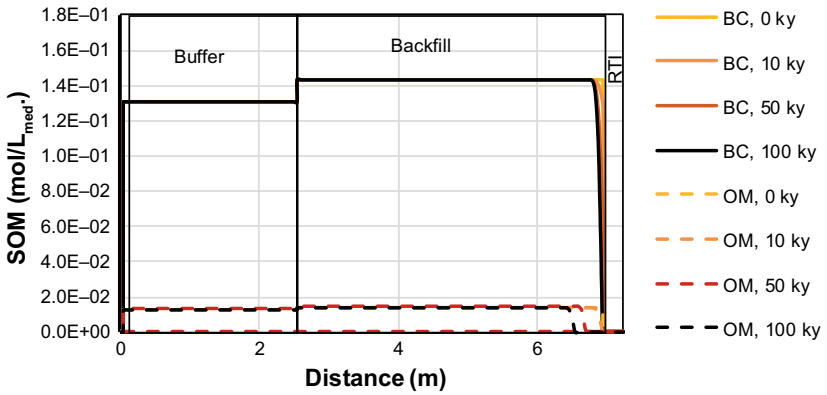

Figure 7-19. *Longitudinal profile of solid organic matter (mol/L medium) for different times in the Organic Matter sensitivity case (OM), as compared to the Base Case (BC).*

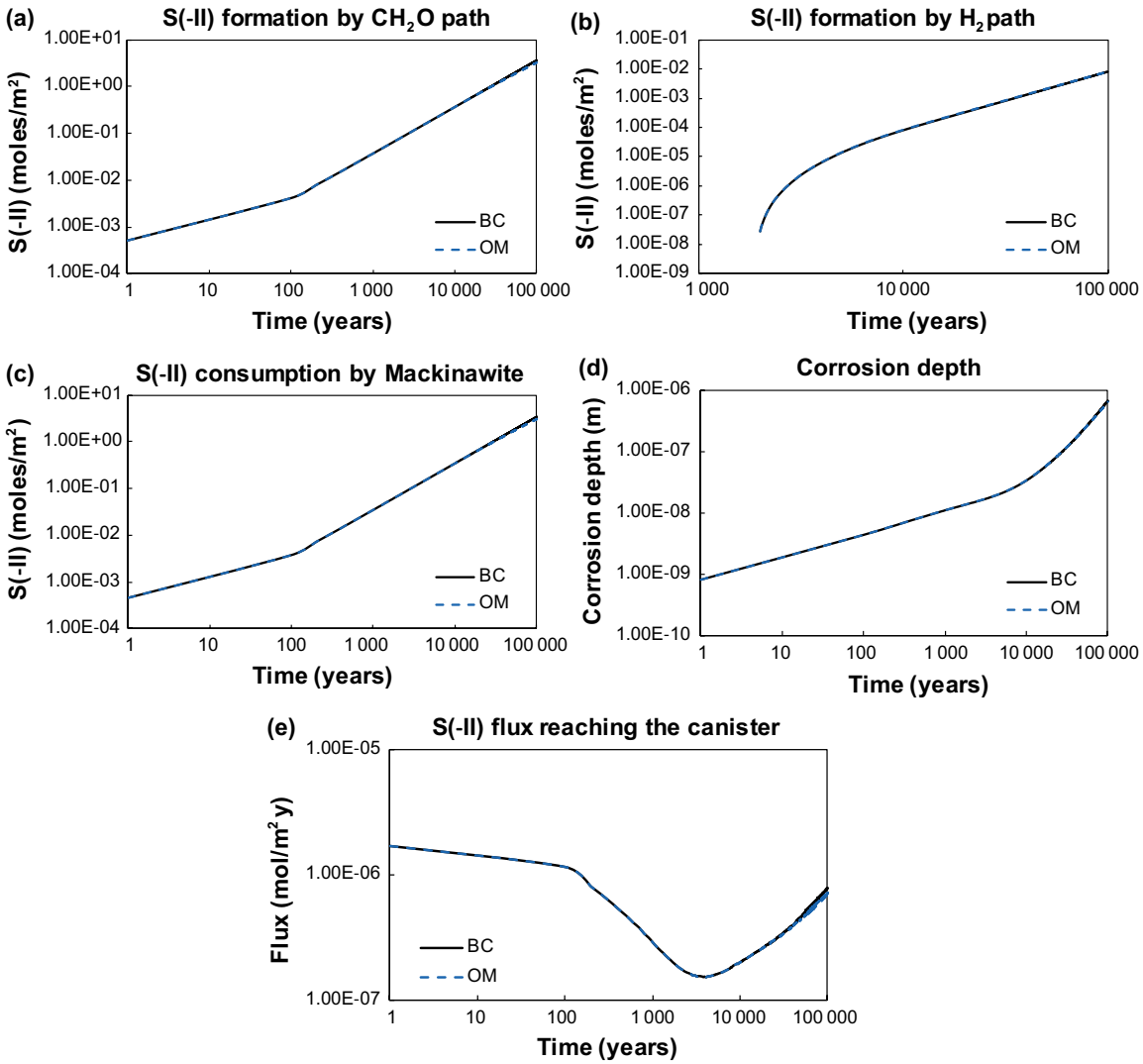

Figure 7-20. *Comparison of results of Organic Matter sensitivity case vs. Base Case (corrosion depth, S(-II) budget plots): cumulative sulfide generation (in moles/m^2) by (a) CH_2O path and (b) H_2 path, (c) cumulative sulfide consumption (in moles/m^2) by mackinawite precipitation, (d) corrosion depth (m), and (e) sulfide flux reaching the canister (moles/m^2 year) .*

Table 7-4. Produced and consumed sulfide at 100 kyr in the Organic Matter case and the Base case: production, consumption, and accumulation. Amount of sulfide in moles, considering a cross-section of 1 m^2.

Case		Produced sulfide (moles/m^2)			Consumed sulfide (moles/m^2)				Corrosion Depth (μm)
		CH_2O path	H_2 path	Total	Mackinawite	Porewater	Corrosion	Total	
Base Case	TM	3.55	8.21E−03	3.56	3.50 (98.6 %)	1.02E−02 (0.287 %)	4.76E−02 (1.34 %)	3.56	0.675
	HM	3.32	1.43E−02	3.33	3.20 (96.2 %)	2.23E−02 (0.67 %)	8.30E−02 (2.49 %)	3.31	1.18
Organic Matter	TM	3.18	7.86E−03	3.18	3.13 (98.3 %)	8.92E−03 (0.28 %)	4.50E−02 (1.41 %)	3.18	0.638

7.4 Fe(II) Minerals

The Fe(II) Minerals variant cases consist of varying the amount of iron minerals (i.e. siderite) that may react with sulfide in the buffer and backfill to form mackinawite and thus act as a sink for sulfide. Two different cases are presented below:

- Siderite Increase (SI) case: the amount of siderite was increased from 0 to 0.5 wt. % in the buffer and from 1.1 to 2.2 wt. % in the backfill. This case was simulated with the traditional model as well as the hybrid model.
- No Siderite (NS) case: siderite is initially removed from both the buffer and backfill, as well as Fe from the cation exchanger. The only available Fe is the initial porewater concentration. This case was tested with the traditional model only.

7.4.1 Traditional model

In the Siderite Increase case, siderite is still present in the entire backfill, as in the Base Case, even after 100 kyr (including at the backfill – RTI interface, see Figure 7-21a). Also, pH in the buffer and backfill presents a very similar evolution (Figure 7-21b), such that sulfide entering the buffer is below the solubility limit. For that reason, there is no mackinawite precipitation in this domain in the Sulfide Increase case (Figure 7-21c), despite the presence of siderite. Thus, the effect of increasing the amount of siderite compared to the Base Case does not influence sulfide production and transport, or its consumption (see Figure 7-22 and Table 7-5).

The removal of siderite from the system, however, does have a significant effect on sulfide concentrations in the long term (Figure 7-22). In the No Siderite case, the only source of iron is the initial porewater concentration. Thus, there is much less iron available in the buffer and backfill to form mackinawite, as compared to the Base Case (Figure 7-22c). This is especially the case after 10 kyr, where Fe availability clearly starts to be the limiting factor for mackinawite formation (Figure 7-23b and Figure 7-22c). This results in higher concentrations of sulfide and a larger sulfide flux reaching the canister in the No Siderite case (see Figure 7-23a and Figure 7-22e). Canister corrosion (Figure 7-22d) and production of sulfide by the H_2 path (Figure 7-22b) increase by almost two orders of magnitude at 100 kyr in the No Siderite case.

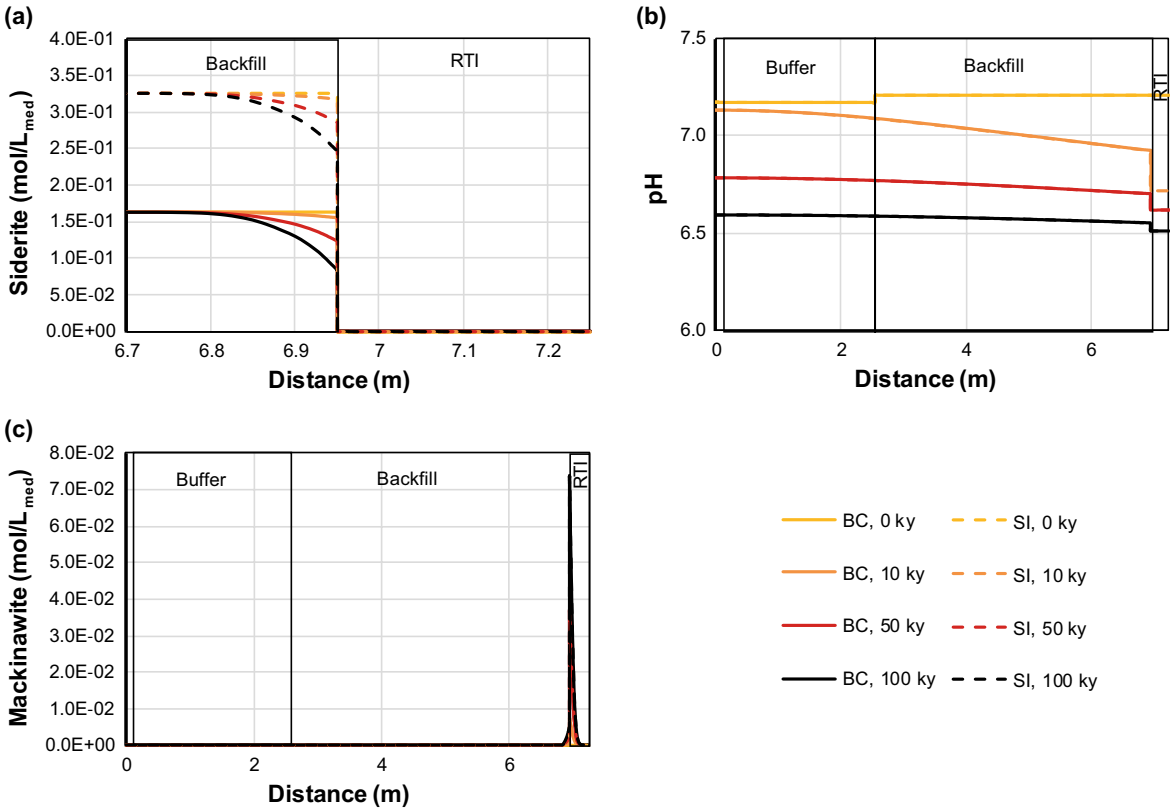

Figure 7-21. *Longitudinal profiles of (a) siderite, in mol/L medium, near the interface between backfill and RTI, (b) pH and (c) mackinawite, in mol/L medium, for different times in the Siderite Increase case as compared to the Base Case.*

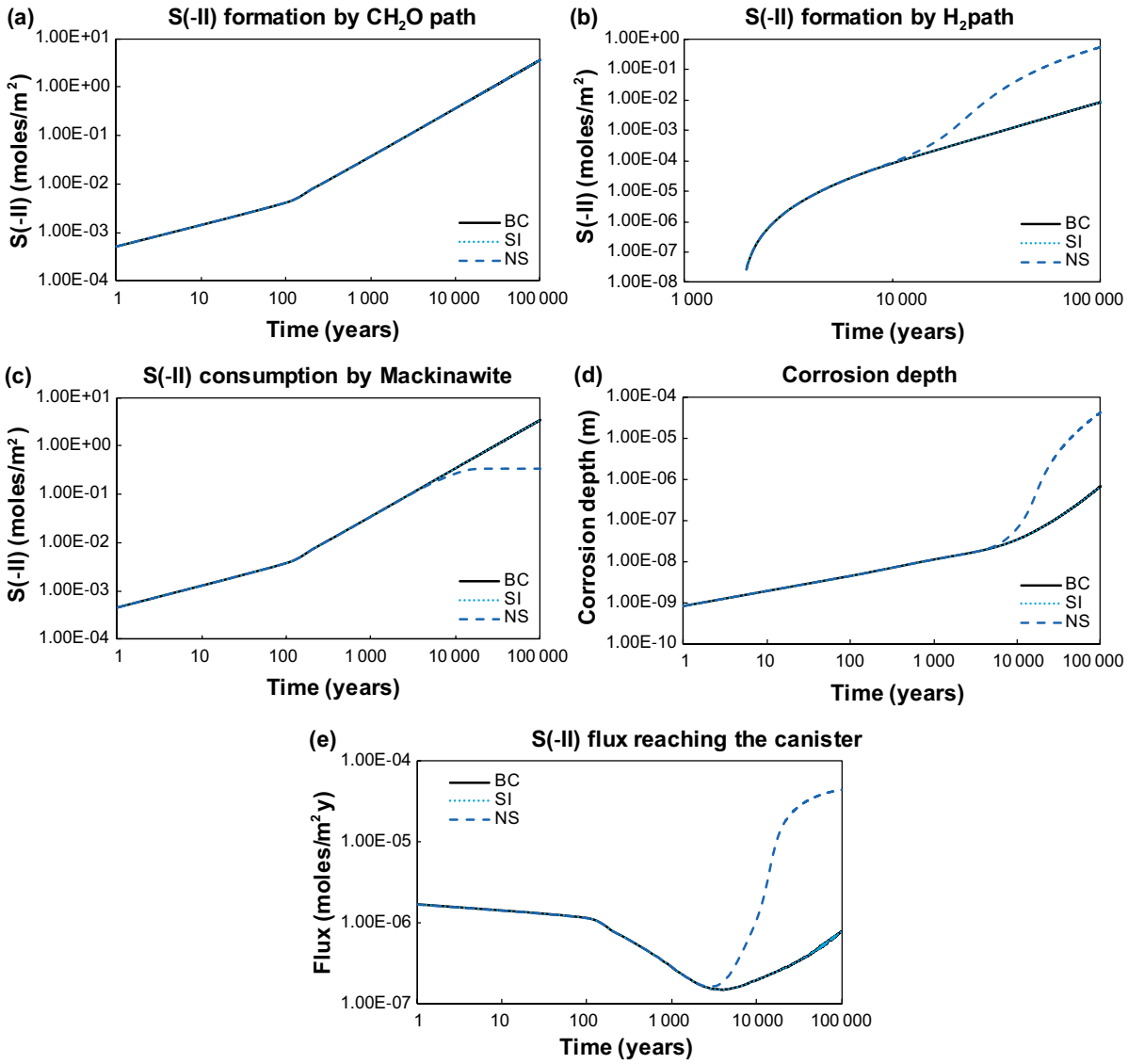

Figure 7-22. *Comparison of results of Fe(II) mineral sensitivity cases vs. Base Case (corrosion depth, S(-II) budget plots): cumulative sulfide generation (in moles/m^2) by (a) CH_2O path and (b) H_2 path, (c) cumulative sulfide consumption by mackinawite precipitation (in moles/m^2), (d) corrosion depth (m), and (e) sulfide flux reaching the canister (moles/m^2 year). The Siderite Increase results are not clearly visibile because they overlap completely with the Base Case results.*

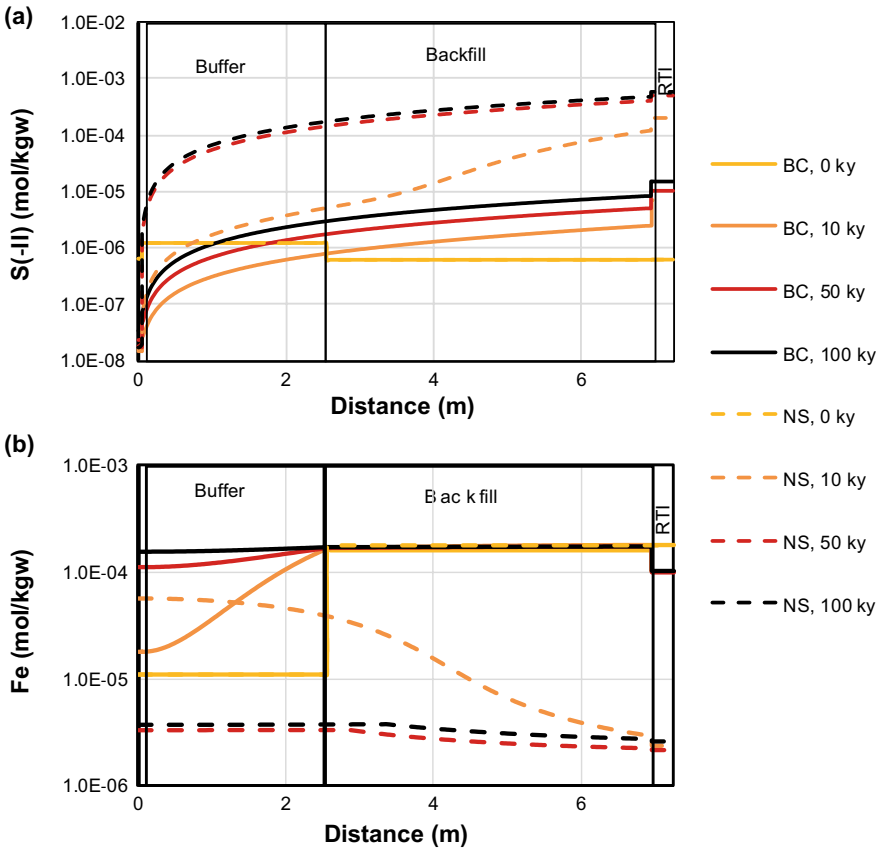

Figure 7-23. *Longitudinal profiles of (a) total aqueous sulfide and (b) iron concentrations in mol/kg$_{water}$ for different times in the case without siderite as compared to the Base Case.*

7.4.2 Hybrid model

As mentioned above, the Siderite Increase case was simulated with both the traditional and the hybrid model. The results of these two models are compared in this section.

Table 7-5 shows the sulfide budget for the hybrid and traditional Siderite Increase case, as well as for the hybrid and traditional Base Case. If one compares the results of the two hybrid models, it is clear that increasing the initial amount of siderite in the buffer and backfill does not have a significant effect on the general evolution of the system. The same conclusion was reached for the traditional models in the previous section.

Furthermore, the differences between the hybrid and traditional models in the Siderite Increase case are very similar to the differences in the Base Case (compare Figure 6-18, Figure 6-19 and Figure 6-20 with Figure 7-24).

Sulfide production by the CH_2O path is slightly lower in the hybrid model (Figure 7-24a) due to a limited transport of DOM. However, the higher flux of sulfide in the hybrid model in the long term (Figure 7-24e) causes relatively less mackinawite precipitation, more canister corrosion and more sulfide production by the H_2 path (Figure 7-24c, d and b respectively).

Table 7-5. Sulfide budget in the different Base Case and Fe(II) Minerals models at 100 000 years: production, consumption, and accumulation. Amount of sulfide in moles, considering a cross-section of 1 m^2. Percentages are given with respect to total sulfide produced.

Case		Produced sulfide (moles/m^2)			Consumed sulfide (moles/m^2)				Corrosion depth (µm)
		CH_2O path	H_2 path	Total	Mackinawite	Porewater	Corrosion	Total	
Base Case	TM	3.55	8.21E−03	3.56	3.50 (98.6 %)	1.02E−02 (0.287 %)	4.76E−02 (1.34 %)	3.56	0.675
	HM	3.32	1.43E−02	3.33	3.20 (96.2 %)	2.23E−02 (0.67 %)	8.30E−02 (2.49 %)	3.31	1.18
Siderite Increase	TM	3.55	8.20E−03	3.56	3.50 (98.4 %)	1.02E−02 (0.286 %)	4.76E−02 (1.34 %)	3.56	0.675
	HM	3.32	1.42E−02	3.33	3.20 (96.2 %)	2.23E−02 (0.67 %)	8.29E−02 (2.49 %)	3.31	1.18
No Siderite	(TM)	3.55	5.29E−01	4.08	3.45E−01 (8.44 %)	6.86E−01 (16.8 %)	3.03 (74.3 %)	4.06	43

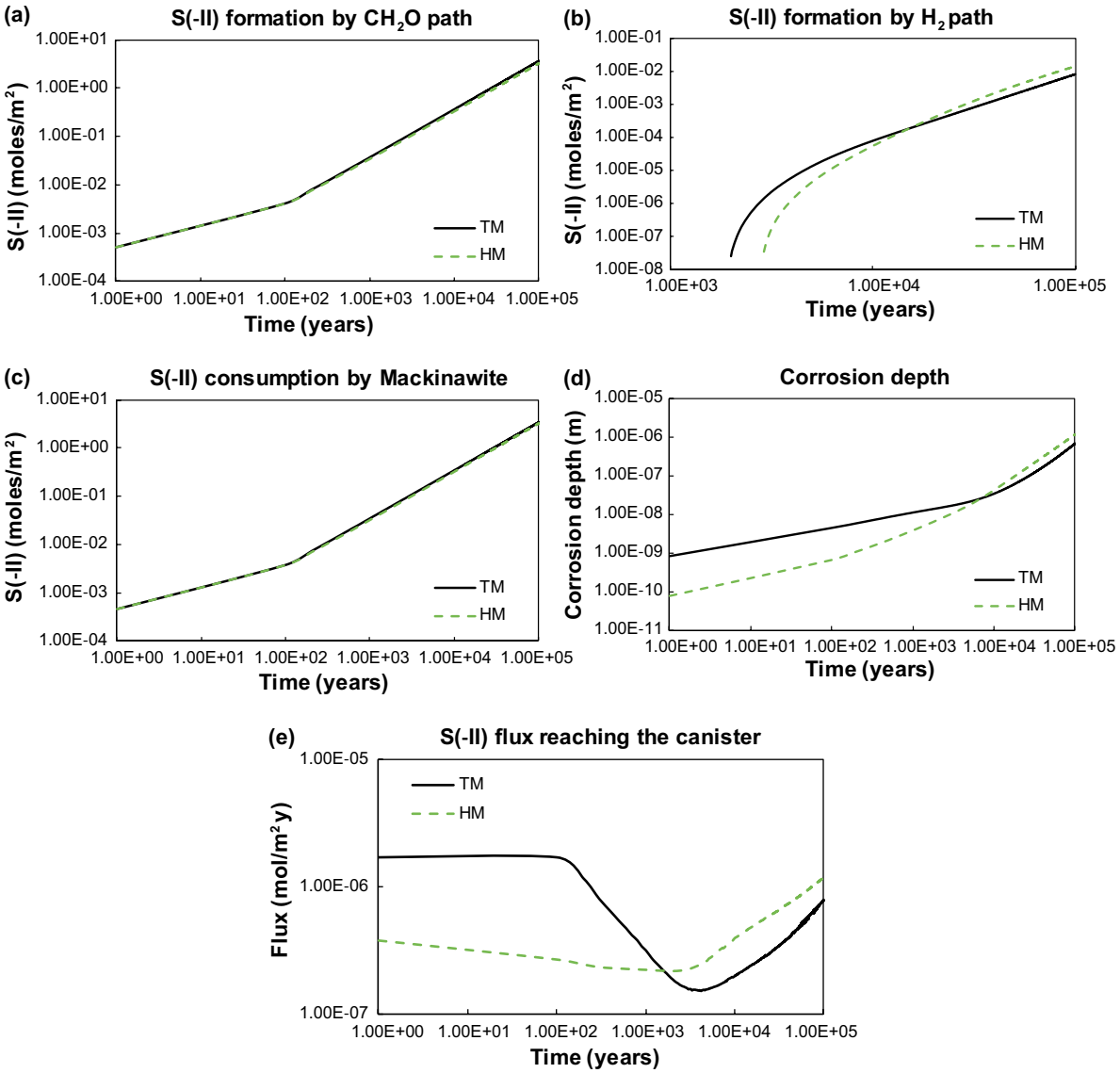

Figure 7-24. *Comparison of Siderite Increase results of TM vs. HM (corrosion depth, S(-II) budget plots): cumulative sulfide generation (in moles/m^2) by (a) CH_2O path and (b) H_2 path, (c) cumulative sulfide consumption by mackinawite precipitation (in moles/m^2), (d) corrosion depth (m), and (e) sulfide flux reaching the canister (moles/m^2 year).*

8 Summary

The main goal of the Integrated Sulfide Project between Posiva and SKB is the assessment of copper corrosion in the canister of a KBS-3V repository due to the presence of sulfide. To this end, conceptual and numerical models of sulfide in the near-field are needed to quantify the different processes concerning sulfide production, transport and consumption.

In this work, a model – called the *hybrid model* – for treating the combination of diffusive transport and aqueous chemistry in compacted, water saturated bentonite has been defined, numerically implemented, and evaluated. The main idea behind the hybrid model is to assume all (diffusive) transport to take place within an interconnected network of interlayer pores, while all chemical reactions are treated entirely within a disconnected, stagnant bulk water phase. In this way, the interlayer specific features of (ion) transport – which have been demonstrated experimentally to fully dominate the transport characteristics of compacted bentonite – are captured. At the same time, conventional geochemical simulators such as Phreeqc can be used to handle chemical reactions within the bentonite. Moreover, a requirement of the hybrid model is that the bulk and interlayer domains must be in local Donnan equilibrium at all times. Treating this type of equilibrium is consequently central, and the details for a calculation framework have been presented in Section 2.3.

The key parameter calculated within this framework is the so-called Donnan factor (f_D), which quantifies the electrostatic potential difference between the bulk and interlayer domains. Once this potential difference is known, ions are simply partitioned between the domains in accordance with the Boltzmann distribution. A complicating aspect of performing this partitioning (as well as performing the calculation of f_D) is the requirement of knowing the activity coefficients for all involved chemical species both in the bulk and in the interlayer domain. Therefore, procedures to relate interlayer activity coefficients to experimental quantities – in particular to cation selectivity coefficients – were presented in Section 2.3.4, and existing experimental data were evaluated in Section 6.4.1.

An implementation of the hybrid model in the reactive transport modelling framework iCP (Nardi et al. 2014) was presented and verified using reasonably simple test cases. Several illuminating results were obtained (see Section 5) by comparing the results of these test cases with the traditional approach to reactive transport in compacted bentonite, which treats interlayer pores as simple ion exchangers without transport capacity. In particular, these verification tests demonstrated that qualitatively different results are obtained when the interlayer domain is allowed to dominate the diffusional transport capacity, as compared to treating interlayers merely as cation sorption sites. Moreover, the hybrid model presented here demonstrates that the Donnan equilibrium model developed by Birgersson and Karnland (2009) is compatible with available geochemical models of compacted bentonite (e.g. Bradbury and Baeyens 2003, Wersin 2003, Arcos et al. 2003). The hybrid model resembles traditional geochemical models in that both consider that mineral and aqueous reactions take place within a bulk porosity and that the interlayer water is chemically inactive.

The Base Case defined within the Integrated Sulfide project, modelling the near-field evolution of a KBS-3V repository, was simulated first with a traditional approach (i.e. by treating interlayer pores as cation exchange sorption sites with no transport capacity) in Section 6.3. In Section 6.4, on the other hand, the hybrid model was applied to the Base Case and the results were compared to those obtained with the traditional approach. These simulations are based on a 1D geometry and include the canister, buffer, tunnel backfill, rock-tunnel interface (RTI), and host rock domains, with special focus on sulfide reactions and transport. Note that this 1D setup is not fully representative for the repository system and largely under-estimates canister corrosion. This is related with the fact that the RDI in the deposition hole, which generates a significant amount of sulfide and is closer to the canister than the RTI, is not included in the model.

In addition, a set of variant cases have been simulated to study the impact on the corrosion of copper in the canister of several processes:

- A backfill density that is low enough to sustain SRB activity in its entire volume (Section 7.1)
- Presence of steel at the rock-tunnel interface: effect of corrosion of steel in rock bolts and stretch metal producing hydrogen and magnetite (Section 7.2)
- Effect of changing organic matter content in buffer and backfill (Section 7.3)
- Effect of changing the amount of Fe(II) minerals that can react with sulfide in the buffer and backfill (Section 7.4)

A summary of main results in the different models and variant cases are given in Table 8-1.

Simulations using the hybrid model are computationally more intensive than the traditional model due to the complexity of the conceptual model (Donnan equilibrium calculations, transport of each aqueous species, need of special treatment of interfaces between bentonite and other porous media, etc.).

When it comes to sulfide production by sulfate reduction, two reaction paths have been considered: one in which the electron donor is organic matter (simplistically represented as CH_2O), and another one in which the electron donor is hydrogen. The results of the different simulations showed that the first reaction path accounts for the vast majority (99 %) of sulfide production in absence of corroding steel. If there is increased hydrogen production due to the presence of corroding steel, however, sulfide production through the hydrogen path is comparable to the sulfide produced by the CH_2O path.

Both sulfide production rates taking place in the RTI are much faster than the diffusion of reactants into this domain. Therefore, sulfide production is mainly limited by diffusion of dissolved organic matter from the backfill towards the RTI. The diffusion of sulfate, the other reactant needed for sulfide production by the CH_2O path, does not limit sulfide production because it presents higher concentrations in the backfill and is needed in smaller quantities due to the stoichiometry of the reaction. If the sulfide production reactions were to take place in the backfill as well, on the other hand, one can expect an increase in sulfide production of almost two orders of magnitude in 100 kyr (see Section 7.1).

Once sulfide is formed in the RTI, its transport towards the copper canister is limited mainly by mackinawite precipitation. This mineral acts as a sulfide sink and controls sulfide concentrations through its solubility. In most of the cases tested in this work, more than 90 % of the sulfide precipitated as mackinawite and only 1-2 % reached the canister causing copper corrosion. Mackinawite precipitation depends on the availability of iron in the bentonite barriers as primary mineral (siderite) and in the bentonite interlayer. For a variant case with absence of iron sources in the system, limited mackinawite precipitation occurs. In this scenario, a significant amount of sulfide (74 %) reached the canister, see Section 7.4. The solubility of mackinawite in terms of sulfide concentration at equilibrium depends on the pH of the pore solution. Cases with a relatively low pH due to SRB activity in the backfill result in higher sulfide concentrations and up to 5 % of sulfide reaching the canister. On the other hand, cases in which pH increases (Interface Metals case) result in less than 0.1 % of the sulfide reaching the canister.

In general, the use of a hybrid model to simulate reactive transport in the system under study had a small effect on the results as compared to the traditional modelling approach. The general trend was that considering transport through interlayer pores, instead of through bulk porosity, slightly reduced mackinawite precipitation and increased sulfide fluxes reaching the canister, and thus canister corrosion. Depending on the simulation case, canister corrosion can decrease by 12 % or increase by a factor of 4 when using a hybrid model as compared to a traditional reactive transport model, see Table 8-1. However, it should be mentioned that the cases simulated in the present work may not be the best test cases to analyse the differences between a traditional reactive transport model and the hybrid model. In the current setup, the diffusion of sulfide from the RTI towards the canister is controlled, at least to some extent, by the RTI transport properties, which acts as a diffusion barrier. In this context, diffusion across the bentonite barriers is partially limited by the diffusive transport properties of the RTI/RDI. Moreover, production and consumption of sulfide by sulfate reduction and corrosion/mackinawite precipitation, respectively, take place outside the bentonite barriers (except some mackinawite formation in the backfill). This is thought to be one of the reasons why different models

for diffusion-reaction processes in compacted bentonite, such as the hybrid model or more traditional models, yield rather similar results. In other words, the Base Case is not optimized for analysing differences between a traditional reactive transport model and the hybrid model.

A final note concerns the numerical implementation of the models. No attempt to study in detail the impact of the spatial and temporal discretization on the results has been made in this work, which has mainly focused on the development of a new conceptual model for reactive transport in compacted bentonite. Even though the results could be affected to some extent by different discretizations, especially at the interfaces, it is thought that the governing processes and main conclusions of the study would remain largely unaffected.

Table 8-1. Sulfide budget obtained in the different models at 100 000 years: production, consumption, and accumulation. Percentages are given with respect to total sulfide produced.

Case		Produced sulfide (moles/m^2)			Consumed sulfide (moles/m^2)				Corrosion depth (μm)
		CH_2O path	H_2 path	Total	Mackinawite precipitation	Accumulated in water	Corrosion rate	Total	
Base Case		3.54	7.61E−03	3.55	3.50 (98.7 %)	9.48E−03 (0.268 %)	4.40E−02 (1.24 %)	3.55	0.624
Base Case with Surface Complexation		3.55	5.62E−03	3.56	3.52 (99.%)	5.49E−03 (0.15 %)	3.18E−02 (0.89 %)	3.56	0.451
Base Case (Simpl.)	**TM**	3.55	8.21E−03	3.56	3.50 (98.6 %)	1.02E−02 (0.287 %)	4.76E−02 (1.34 %)	3.56	0.675
	HM	3.32	1.43E−02	3.33	3.20 (96.2 %)	2.23E−02 (0.67 %)	8.30E−02 (2.49 %)	3.31	1.18
Backfill Density (fast)	**TM**	341	4.36	345	326 (94.3 %)	1.64 (0.48 %)	17.6 (5.11 %)	345	250
	HM	333	3.75	337	319 (94.7 %)	1.89 (0.56 %)	15.4 (4.57 %)	336	218
Backfill Density (slow)	**TM**	320	2.38	322	311 (96.4 %)	1.59 (0.49 %)	9.78 (3.03 %)	322	139
	HM	319	2.17	321	310 (96.5 %)	1.87 (0.58 %)	9.05 (2.82 %)	320	128
Interface Metals	**TM**	3.63	5.89	9.52	9.56 (100 %)	−2.21E−03 (−2.32E−02 %)	1.98E−03 (2.08E−02 %)	9.56	2.81E−02
	TM (SC)	3.63	5.89	9.52	9.56 (100 %)	−2.19E−03 (−2.30E−02 %)	2.13E−03 (2.32E−02 %)	9.56	3.02E−02
	HM	3.40	5.82	9.21	8.69 (94.3 %)	−2.76E−03 (−3.00E−02 %)	8.46E−03 (9.18E−02 %)	8.69	0.12
Organic Matter		3.18	7.86E−03	3.18	3.13 (98.3 %)	8.92E−03 (0.28 %)	4.50E−02 (1.41 %)	3.18	0.638
Siderite Increase	**TM**	3.55	8.20E−03	3.56	3.50 (98.4 %)	1.02E−02 (0.286 %)	4.76E−02 (1.34 %)	3.56	0.675
	HM	3.32	1.42E−02	3.33	3.20 (96.2 %)	2.23E−02 (0.67 %)	8.29E−02 (2.49 %)	3.31	1.18
No Siderite		3.55	5.29E−01	4.08	3.45E−01 (8.44 %)	6.86E−01 (16.8 %)	3.03 (74.3 %)	4.06	43

References

SKB's (Svensk Kärnbränslehantering AB) publications can be found at www.skb.com/publications

Alt-Epping P, Tournassat C, Rasouli P, Steefel C I, Mayer K U, Jenni A, Mäder U, Sengor S S, Fernández R, 2015. Benchmark reactive transport simulations of a column experiment in compacted bentonite with multispecies diffusion and explicit treatment of electrostatic effects. Computational Geosciences 19, 535–550.

Appelo C A J, 2013. A review of porosity and diffusion in bentonite. Posiva Working Report 2013–29, Posiva Oy, Finland.

Appelo C A J, Van Loon L R, Wersin P, 2010. Multicomponent diffusion of a suite of tracers (HTO, Cl, Br, I, Na, Sr, Cs) in a single sample of Opalinus Clay. Geochimica et Cosmochimica Acta 74, 1201–1219.

Arcos D, Bruno J, Benbow S, Takase H, 2000. Behaviour of bentonite accessory minerals during the thermal stage. SKB TR-00-06, Svensk Kärnbränslehantering AB.

Arcos D, Bruno J, Karnland O, 2003. Geochemical model of the granite–bentonite–groundwater interaction at Äspö HRL (LOT experiment). Applied Clay Science 23, 219–228.

Birgersson M, 2019. Task Force on EBS C-session: Calculation of benchmarks 1–5. SKB TR-19-16, Svensk Kärnbränslehantering AB.

Birgersson M, Karnland O, 2009. Ion equilibrium between montmorillonite interlayer space and an external solution – Consequences for diffusional transport. Geochimica et Cosmochimica Acta 73, 1908–1923.

Birgersson M, Karnland O, 2014. Summary of Clay Technology's work within FORGE. In Sellin P (ed). Experiments and modelling on the behaviour of EBS. FORGE Report D.3.38, 218–232.

Bourg I C, Tournassat C, 2015. Self-diffusion of water and ions in clay barriers. In Tournassat C, Steefel C I, Bourg I C, Bergaya F (eds). Natural and engineered clay barriers. Amsterdam: Elsevier. (Developments in Clay Science), 189–226.

Bradbury M H, Baeyens B, 1997. A mechanistic description of Ni and Zn sorption on Na-montmorillonite Part II: modelling. Journal of Contaminant Hydrology 27, 223–248.

Bradbury M H, Baeyens B, 2002. Porewater chemistry in compacted re-saturated MX-80 bentonite: physicochemical characterisation and geochemical modelling. PSI Bericht 02e10, Paul Scherrer Institut, NTB 01-08, Nagra, Switzerland.

Bradbury M H, Baeyens B, 2003. Porewater chemistry in compacted re-saturated MX-80 bentonite. Journal of Contaminant Hydrology 61, 329–338.

Byegård J, Selnert E, Tullborg, E-L, 2008. Bedrock transport properties. Data evaluation and retardation model. Site descriptive modelling SDM-Site Forsmark. SKB R-08-98, Svensk Kärnbränslehantering AB.

Carlson L, 2004. Bentonite mineralogy. Part 1: Methods of investigation - a literature review. Part 2: Mineralogical research of selected bentonites. Posiva Working Report 2004-02, Posiva Oy, Finland.

Charlet L, Tournassat C, 2005. Fe(II)–Na(I)–Ca(II) cation exchange on montmorillonite in chloride medium: evidence for preferential clay adsorption of chloride – metal ion pairs in seawater. Aquatic Geochemistry 11, 115–137.

Charlton S R, Parkhurst D L, 2011. Modules based on the geochemical model PHREEQC for use in scripting and programming languages. Computers & Geosciences 37, 1653–1663.

COMSOL, 2015. COMSOL Multiphysics® v.5.2., COMSOL AB, Stockholm.

Curti E, Wersin P, 2002. Assessment of porewater chemistry in the bentonite backfill for the Swiss SF/HLW repository.Nagra Technical Report 02-09, Nagra, Switzerland.

Dohrmann R, Olsson S, Kaufhold S, Sellin P, 2013. Mineralogical investigations of the first package of the alternative buffer material test – II. Exchangeable cation population rearrangement. Clay Minerals 48, 215–233.

Fernández A M, Baeyens B, Bradbury M, Rivas P, 2004. Analysis of the porewater chemical composition of a Spanish compacted bentonite used in an engineered barrier. Physics and Chemistry of the Earth, Parts A/B/C 29, 105–118.

Giffaut E, Grivé M, Blanc P, Vieillard P, Colàs E, Gailhanou E, Gaboreau S, Marty N, Madé B, Duro L, 2014. Andra thermodynamic database for performance assessment: ThermoChimie. Applied Geochemistry 49, 225–236.

Gimmi T, Kosakowski G, 2011. How mobile are sorbed cations in clays and clay rocks? Environmental Science & Technology 45, 1443–1449.

Glaus M A, Baeyens B, Bradbury M H, Jakob A, Van Loon L R, Yaroshchuk A, 2007. Diffusion of ^{22}Na and ^{85}Sr in montmorillonite: evidence of interlayer diffusion being the dominant pathway at high compaction. Environmental Science & Technology 41, 478–485.

Glaus M A, Frick S, Rossé R, Van Loon L R, 2010. Comparative study of tracer diffusion of HTO, $^{22}Na^{+}$ and $^{36}Cl^{-}$ in compacted kaolinite, illite and montmorillonite. Geochimica et Cosmochimica Acta 74, 1999–2010.

Glaus M A, Birgersson M, Karnland O, Van Loon L R, 2013. Seeming steady-state uphill diffusion of $^{22}Na^{+}$ in compacted montmorillonite. Environmental Science & Technology 47, 11522–11527.

Glaus M A, Aertsens M, Appelo C A J, Kupcik T, Maes N, Van Laer L, Van Loon L R, 2015. Cation diffusion in the electrical double layer enhances the mass transfer rates for Sr^{2+}, Co^{2+} and Zn^{2+} in compacted illite. Geochimica et Cosmochimica Acta 165, 376–388.

Hansen J, Korkiala-Tanttu L, Keski-Kuha E, Keto P, 2010. Deposition tunnel backfill design for a KBS-3V repository. Posiva Working Report 2009-129, Posiva Oy, Finland.

Hartley L, Hoek J, Swan D, Appleyard P, Baxter S, Roberts D, Simpson T, 2013. Hydrogeological modelling for assessment of radionuclide release scenarios for the repository system 2012. Posiva Working Report 2012-42, Posiva Oy, Finland.

Hellä P, Pitkänen P, Löfman J, Partamies S, Vuorinen U, Wersin P, 2014. Safety case for the disposal of spent nuclear fuel at Olkiluoto. Definition of reference and bounding groundwaters, buffer and backfill porewaters. Posiva 2014-04, Posiva Oy, Finland.

Holmboe M, Wold S, Jonsson M, 2012. Porosity investigation of compacted bentonite using XRD profile modeling. Journal of Contaminant Hydrology 128, 19–32.

Hsiao Y-W, Hedström M, 2017. Swelling pressure in systems with Na-montmorillonite and neutral surfaces: a molecular dynamics study. The Journal of Physical Chemistry C 121, 26414–26423.

Idiart A, Pękala M, 2016. Models for diffusion in compacted bentonite. SKB TR-15-06, Svensk Kärnbränslehantering AB.

Itälä A, Muurinen A, 2012. Na/Ca selectivity coefficients of montmorillonite in perchlorate solution at different temperatures. In Symposium NW – Scientific basis for nuclear waste management XXXV: symposium held in Buenos Aires, Argentina, 2–7 October 2011. Warrendale, PA: Materials Research Society. (Materials Research Society Symposium Proceedings 1475)

Jin Q, Roden E E, Giska J R, 2013. Geomicrobial kinetics: extrapolating laboratory studies to natural environments. Geomicrobiology Journal 30, 173–185.

Karnland O, 2010. Chemical and mineralogical characterization of the bentonite buffer for the acceptance control procedure in a KBS-3 repository. SKB TR-10-60, Svensk Kärnbränslehantering AB.

Karnland O, Olsson S, Nilsson U, 2006. Mineralogy and sealing properties of various bentonites and smectite-rich clay material. SKB TR-06-30, Svensk Kärnbränslehantering AB.

Karnland O, Birgersson M, Hedström M, 2011. Selectivity coefficient for Ca/Na ion exchange in highly compacted bentonite. Physics and Chemistry of the Earth, Parts A/B/C 36, 1554–1558.

Keller L M, Holzer L, Gasser P, Erni R, Rossell M D, 2014. Intergranular pore space evolution in MX80 bentonite during a long-term experiment. Applied Clay Science 104, 150–159.

King F, Kolář M, 2018. Copper Sulfide Model (CSM) – model improvements, sensitivity analyses, and results from the Integrated Sulfide Project inter-model comparison exercise. SKB TR-18-08, Svensk Kärnbränslehantering AB.

Kumpulainen S, Kiviranta L, 2010. Mineralogical and chemical characterization of various bentonite and smectite-rich clay materials. Part A: Comparison and development of mineralogical characterization methods Part B: Mineralogical and chemical characterization of clay materials. Posiva Working Report 2010–52, Posiva Oy, Finland.

Kumpulainen S, Kiviranta L, 2011. Mineralogical, chemical and physical study of potential buffer and backfill materials from ABM Test Package 1. Posiva Working Report 2011-41, Posiva Oy, Finland.

Maia F, Puigdomenech I, Molinero J, 2016. Modelling rates of bacterial sulfide production using lactate and hydrogen as energy sources. SKB TR-16-05, Svensk Kärnbränslehantering AB.

Muurinen A, 2006. Ion concentration caused by an external solution into the porewater of compacted bentonite. Posiva Working Report 2006–96, Posiva Oy, Finland.

Muurinen A, Lehikoinen J, 1999. Porewater chemistry in compacted bentonite. Posiva 99-20, Posiva Oy, Finland.

Muurinen A, Karnland O, Lehikoinen J, 2004. Ion concentration caused by an external solution into the porewater of compacted bentonite. Physics and Chemistry of the Earth, Parts A/B/C 29, 119–127.

Muurinen A, Karnland O, Lehikoinen J, 2007. Effect of homogenization on the microstructure and exclusion of chloride in compacted bentonite. Physics and Chemistry of the Earth, Parts A/B/C 32, 485–490.

Müller-Vonmoos M, Kahr G, 1983. Mineralogische Untersuchungen von Wyoming Bentonite MX-80 und Montigel. NAGRA Technischer Bericht 83–12, Nagra, Switzerland. (In German.)

Nardi A, Idiart A, Trinchero P, de Vries L M, Molinero J, 2014. Interface COMSOL-PHREEQC (iCP), an efficient numerical framework for the solution of coupled multiphysics and geochemistry. Computers & Geosciences 69, 10–21.

Nethe-Jaenchen R, Thauer R K, 1984. Growth yields and saturation constant of *Desulfovibrio vulgaris* in chemostat culture. Archives of Microbiology 137, 236–240.

Parkhurst D L, Appelo C A J, 2013. Description of input and examples for PHREEQC version 3 – A computer program for speciation, batch-reaction, one-dimensional transport, and inverse geochemical calculations. Techniques and Methods 6–A43, U.S. Geological Survey, Denver, Colorado.

Pękala M, Alt-Epping P, Wersin P, 2019. 3D and 1D dual-porosity reactive transport simulations – model improvements, sensitivity analyses, and results from the Integrated Sulfide Project inter-model comparison exercise. Posiva Working Report 2018-31, Posiva Oy, Finland

Posiva, 2013. Safety case for the disposal of spent nuclear fuel at Olkiluoto – Models and data for the repository system 2012. Posiva 2013-01, Posiva Oy, Finland.

Samper J, Naves A, Montenegro L, Mon A, 2016. Reactive transport modelling of the long-term interactions of corrosion products and compacted bentonite in a HLW repository in granite: uncertainties and relevance for performance assessment. Applied Geochemistry 67, 42–51.

Salas J, Sena C, Arcos D, 2014. Hydrogeochemical evolution of the bentonite buffer in a KBS-3 repository for radioactive waste. Reactive transport modelling of the LOT A2 experiment. Applied Clay Science 101, 521–532.

Sposito G, 1981. The thermodynamics of soil solution. Oxford University Press.

Sposito G, Holtzclaw K M, Charlet L, Jouany C, Page A L, 1983. Sodium–calcium and sodium–magnesium exchange on Wyoming bentonite in perchlorate and chloride background ionic media1. Science Society of America Journal 47, 51–56.

Svensson D, Dueck A, Nilsson U, Olsson S, Sandén T, Lydmark S, Jägerwall S, Pedersen K, Hansen S, 2011. Alternative buffer material. Status of the ongoing laboratory investigation of reference materials and test package 1. SKB TR-11-06, Svensk Kärnbränslehantering AB.

Tachi Y, Yotsuji K, 2014. Diffusion and sorption of Cs^+, Na^+, I^- and HTO in compacted sodium montmorillonite as a function of porewater salinity: integrated sorption and diffusion model. Geochimica et Cosmochimica Acta 132, 75–93.

Wersin P, 2003. Geochemical modelling of bentonite porewater in high-level waste repositories. Journal of Contaminant Hydrology 61, 405–422.

Wersin P, Birgersson M, 2014. Reactive transport modelling of iron–bentonite interaction within the KBS-3H disposal concept: the Olkiluoto site as a case study. London: Geological Society. (Special publication 400)

Wersin P, Alt-Epping P, Pitkänen P, Román-Ross G, Trinchero P, Molinero J, Smith P, Snellman M, Filby A, Kiczka M, 2014. Sulfide fluxes and concentrations in the spent nuclear fuel repository at Olkiluoto. Posiva 2014-01, Posiva Oy, Finland.

Appendix A

Analysis of Equation 2-21

Assume the cation(s) with the highest charge to have valency *m* and the anion(s) with the highest charge to have valency - *k*. Multiplying Equation 2-21 by f_D^m and ordering the terms in decreasing powers of f_D gives an equation of the form

$$p(f_D) = 0 \tag{A-1}$$

where

$$p(x) = \sum_{n=0}^{k+m} a_n \cdot x^n \tag{A-2}$$

is a polynomial of order $k + m$. The coefficients a_n are of the form

$$a_n = (m-n) \cdot \sum_j \Gamma_j \cdot c_j^{bulk} \quad n \neq m \tag{A-3}$$

$$a_m = -c_{IL} \tag{A-4}$$

where index *j* runs over all species with the same valency *(m-n)*. As Γ_i and c_i^{bulk} are positive quantities, the sign of the a_n - coefficients are determined by the valency factor *(m-n)*. Thus, by construction

$$a_n \leq 0, n \geq m \tag{A-5}$$

$$a_n \geq 0, n < m \tag{A-6}$$

The sequence of a_n - coefficients consequently only change sign at one place, and according to Descartes' sign rule for polynomials, *p(x)* can only have a single positive real root, i.e. f_D. Furthermore, from the definition of f_D, the value of this root must be in the range $0 < x \leq 1$. Since $p(0) = a_0 > 0$, the derivative at $x = f_D$ is negative (*p(x)* changes sign from positive to negative at $x = f_D$). Generally,

$$p'(x) = \sum_{n=1}^{k+m} n \cdot a_n \cdot x^{n-1} \tag{A-7}$$

Thus,

$$p'(0) = a_1 \tag{A-8}$$

and for $m > 1$, the derivative at $x = 0$ is generally positive. Consequently, *p(x)* has a local maximum in the range $0 \leq x < f_D$ in this case (for the case $m = 1$, $p'(x)$ is negative for all $x \geq 0$ and *p(x)* has no local extremes in this range). The second derivative of *p(x)* is

$$p''(x) = \sum_{n=2}^{k+m} n \cdot (n-1) \cdot a_n \cdot x^{n-2} \tag{A-9}$$

Thus, when $m \leq 2$, $p''(x)$ is negative in the whole range $x \leq 0$.

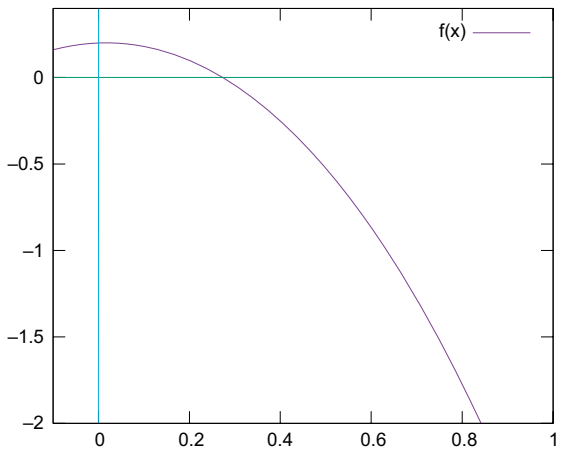

Figure A-1. *Example of a polynomial p(x).*

Appendix B

Summary of Base Case parameters and processes

Domain	Groundwater/Porewater	Minerals (equilibrium)		Kinetic reactions	Cation exchange	Transport Properties	Dimensions
		Primary	Secondary				
Intact rock	B-SO_4 (Table 6-3 in Hellä et al. 2014) SO_4^{2-} & sulfide concs. = 0 Ca or Na: charge balance $[Fe(II)]_{TOT}$= 5.7x10^{-6} M HC, OM: 0 Anoxic conditions Cl^-: 0.1131 M (4010 mg/L) No SRB activity. No sorption processes	-	calcite, mackinawite	-	-	Porosity = 0.00515 D_{eff} = 2.0×10^{-13} m^2/s	5 m from the interfaces Vol = 2050 m^3
RTI (rock – tunnel interface)	B−SO_4 (Table 6-3 in Hellä et al. 2014) SO_4^{2-} & sulfide concs. = 0 DOC: Initially set to 0 Charge balance on Na No sorption processes. SRB activity: Yes	-	calcite, mackinawite	Biotic SO_4 reduction with: C-org: k = 1.5×10−4 s^{-1} H_2(aq): k = 6.4×10^{-5} s^{-1} [biomass]: 3.54×10^{-4} mol/m^3 K_{orgC} = 5.0×10^{-6} M; K_{H2} = 4.0×10^{-6} M; K_{SO4} = 1.0×10^{-5} M;	-	Porosity = 0.01 D_{eff} = 5.0×10^{-13} m^2/s	0.3 m, except below tunnel floor, where it is 0.4 m Tunnel contact = 110.1 m^2 Vol = 35.4 m^3
RDI (rock – deposition hole interface)	B−SO_4 (Table 6-3 in Hellä et al. 2014) SO_4^{2-} & sulfide concs. = 0 DOC: Initially set to 0 Charge balance on Na No sorption processes SRB activity: Yes	-	calcite, mackinawite	Biotic SO_4 reduction with: C−org: k = 1.5×10−4 s^{-1} H_2(aq): k = 6.4×10^{-5} s^{-1} [biomass]: 1.06×10^{-3} mol/m^3 K_{orgC} = 5.0×10^{-6} M; K_{H2} = 4.0×10^{-6} M; K_{SO4} = 1.0×10^{-5} M;	-	Porosity = 0.02 D_{eff} = 1.5×10^{-12} m^2/s	0.1 m Contact with deposition hole = 45.3 m^2 Vol = 2.45 m^3
Backfill	Brackish water (Table F-2 in Posiva 2013) DOC= 2 mg/L of C SOM(s)=0.1wt% of C (143.2 mol/m^3) SRB activity: No	Gypsum 189.8 mol/m^3 Calcite 467 mol/m^3 Siderite 163.3 mol/m^3 (Table 7-5 in Hellä et al. 2014)	mackinawite	-	CEC = 2120 meq/L = 0.47 eq/ kg (Table F-2 in Posiva 2013)	Porosity = 0.43 D_{eff} = 2.15×10^{-11} m^2/s	4 m height, 3.5 m wide, 7.5 m long (distance btwn deptn. holes). Vol = 105 m^2 Cross section = 14 m^2
Buffer	Brackish water (Table E-2 in Posiva 2013) DOC= 2 mg/L of C SOM = 0.1wt% of C (130.7 mol/m^3) SRB activity: No	Gypsum 36.5 mol/m^3 Calcite 327 mol/m^3 (Table 7-5 in Hellä et al. 2014)*	siderite, mackinawite	-	CEC = 2873 meq/L = 0.79 eq/ kg (Table E-2 in Posiva 2013)	Porosity = 0.43 D_{eff} = 2.15×10^{-11} m^2/s	7.8 m height, outer diam. 1.75m, inner diam. 1.05m. Vol = 14.6m^3
Canister	-	-	-	-	-	-	4.8 m height, 1.05 m diam, Area = 17.6 m^2
TDB	Thermodynamic database (Giffaut et al. 2014): Thermochimie version 9b: all equilibrium constants; sulfate/sulfide decoupled; hydrogen from corrosion decoupled						

DOC = dissolved organic matter; SOM = solid organic matter
B-SO4 = Brackish-sulfate groundwater
CEC = Cation Exchange Capacity
SRB = Sulfate Reducing Bacteria
*no siderite is considered in the buffer initially, to keep the porewater Fe concentration as in Table E-2
HC = hydrocarbons; OM = organic matter

Appendix C

Coordinates of the finite element mesh nodes

Canister	6.93257	6.95005
0 - 0.05 m: Every 0.01 m	6.93666	6.95008
Buffer	6.94000	6.95012
0.06164	6.94260	6.95017
0.07731	6.94453	6.95024
0.09838	6.94596	6.95034
0.12674	6.94702	6.95046
0.16489	6.94780	6.95064
0.21318	6.94838	6.95087
0.26261	6.94881	6.95119
0.31223	6.94913	6.95162
0.31223 - 2.55 m: Every $4.97 \cdot 10^{-2}$ m	6.94936	6.95220
Backfill	6.94954	6.95298
2.55 − 6.69984 m: Every $5.00 \cdot 10^{-2}$ m	6.94966	6.95404
6.74662	6.94976	6.95547
6.78493	6.94983	6.95740
6.81619	6.94988	6.96000
6.84169	6.94992	6.96349
6.86251	6.94995	6.96818
6.87949	6.94997	6.97449
6.89335	6.94999	6.98251
6.90466	6.95000	6.99188
6.91388	**RTI**	6.99188 − 7.25 m: Every $9.93 \cdot 10^{-3}$ m
6.92141	6.95001	**Rock**
6.92756	6.95003	7.25 − 12.25 m: Every 0.01 m

Appendix D

List of aqueous species

Full Base Case			Simplified Base Case
$Ca(H_3SiO_4)^+$	$FeCO_3OH$	$S_2O_4^{2-}$	$Ca(HCO_3)^+$
$Ca(HCO_3)^+$	$FeCO_3OH^-$	SO_3^{2-}	$Ca(SO_4)$
$Ca(OH)^+$	$FeHCO_3^+$	SO_4^{2-}	Ca^{2+}
$Ca(SO_4)$	$FeHSO_4^{2+}$	$Si_2O_2(OH)_5^-$	$CaCl^+$
Ca^{2+}	$H(SO_4)^-$	$Si_2O_3(OH)_4^{2-}$	$CaCl_2$
$CaCl^+$	H^+	$Si_3O_5(OH)_5^{3-}$	$CaCO_3$
$CaCl_2$	H_2	$Si_3O_6(OH)_3^{3-}$	Cl^-
$CaCO_3$	$H_2(SiO_4)^{2-}$	$Si_4O_6(OH)_6^{2-}$	CO_2
Cl^-	H_2O	$Si_4O_7(OH)_6^{4-}$	CO_3^{2-}
CO	H_2S	$Si_4O_8(OH)_4^{4-}$	$Fe(CO_3)$
CO_2	$H_3(SiO_4)^-$	$Si_6O_{15}^{6-}$	$Fe(CO_3)_2^{2-}$
CO_3^{2-}	$H_4(SiO_4)$		$Fe(HS)^+$
$Fe(CO_3)$	HCl		$Fe(SO_4)^+$
$Fe(CO_3)_2^{2-}$	HCO_3^-		Fe^{2+}
$Fe(CO_3)_3^{3-}$	Hdg		$FeCl^+$
$Fe(H_3SiO_4)^{2+}$	HS^-		$FeCl_3^-$
$Fe(HS)^+$	K(OH)		$FeHCO_3^+$
$Fe(HS)_2$	$K(SO_4)^-$		$H(SO_4)^-$
$Fe(HSO_4)^+$	K^+		H^+
$Fe(OH)^+$	KCl		H_2
$Fe(OH)^{2+}$	$Mg(CO_3)$		H_2S
$Fe(OH)_2$	$Mg(H_3SiO_4)^+$		$H_3(SiO_4)^-$
$Fe(OH)_2^+$	$Mg(HCO_3)^+$		$H_4(SiO_4)$
$Fe(OH)_3$	$Mg(OH)^+$		HCO_3^-
$Fe(OH)_3^-$	$Mg(SO_4)$		Hdg
$Fe(OH)_4^-$	Mg^{+2}		HS^-
$Fe(OH)_4^{2-}$	$Mg_4(OH)_4^{4+}$		$Na(CO_3)^-$
$Fe(SO_4)$	$MgCl^+$		$Na(HCO_3)$
$Fe(SO_4)^+$	$Na(CO_3)^-$		$Na(SO_4)^-$
$Fe(SO_4)_2^-$	$Na(HCO_3)$		Na^+
Fe^{2+}	Na(OH)		NaCl
Fe^{3+}	$Na(SO_4)^-$		OH^-
$Fe_2(OH)_2^{4+}$	Na^+		$S_2O_3^{2-}$
$Fe_3(OH)_4^{5+}$	NaCl		SO_4^{2-}
$FeCl^+$	OH^-		
$FeCl^{2+}$	S^{2-}		
$FeCl_2$	S_2^{2-}		
$FeCl_2^+$	S_3^{2-}		
$FeCl_3$	S_4^{2-}		
$FeCl_3^-$	S_5^{2-}		
$FeCl_4^-$	$S_2O_3^{2-}$		

Arkitektkopia AB, Bromma, 2020

SKB is responsible for managing spent nuclear fuel and radioactive waste produced by the Swedish nuclear power plants such that man and the environment are protected in the near and distant future.

skb.se